



**EUCENTRE**

European Centre for Training and Research in Earthquake Engineering

**GEO TECHNICAL ASPECTS OF MAY 20, 2012  
M5.9 EMILIA EARTHQUAKE, ITALY**

**Version 1.0**

**July 13, 2012**

**By**

**Carlo G. Lai (University of Pavia, EUCENTRE, Pavia, Italy)**

**Francesca Bozzoni (EUCENTRE, Pavia, Italy)**

**Maria-Daphne Mangriotis (EUCENTRE, Pavia, Italy)**

**Mario Martinelli (EUCENTRE, Pavia, Italy)**

**OTHER CONTRIBUTORS**

**Laura Scandella (EUCENTRE, Pavia, Italy)**

**Filippo Dacarro (EUCENTRE, Pavia, Italy)**

## **Acknowledgments**

The authors would like to acknowledge the support of the Department of Civil Protection of Italian Government and that of the Administration of Emilia-Romagna Region.

The authors would also like to express their gratitude to the local authorities, in particular the Municipality of Sant'Agostino, the Firefighters of the Italian Fire Watch Corps and the Local Agency of Civil Protection of Emilia-Romagna Region for their support and encouragement during the reconnaissance.

The authors are indebted to Prof. Misko Cubrinovski (University of Canterbury, at Christchurch, New Zealand) for the precious recommendations provided on the liquefaction field reconnaissance.

A word of gratitude to the EUCENTRE staff, particularly to Dr. Emilia Fiorini for providing some of the pictures and to Riccardo Melzi and Luca Rotonda for their assistance in carrying out the geophysical investigation.

The field geo-reconnaissance survey has been conducted using the mobile structural and geophysical laboratory unit of EUCENTRE TREES Lab. The authors are grateful to Prof. Alberto Pavese of the University of Pavia and Director of EUCENTRE TREES Lab for his support and encouragement.

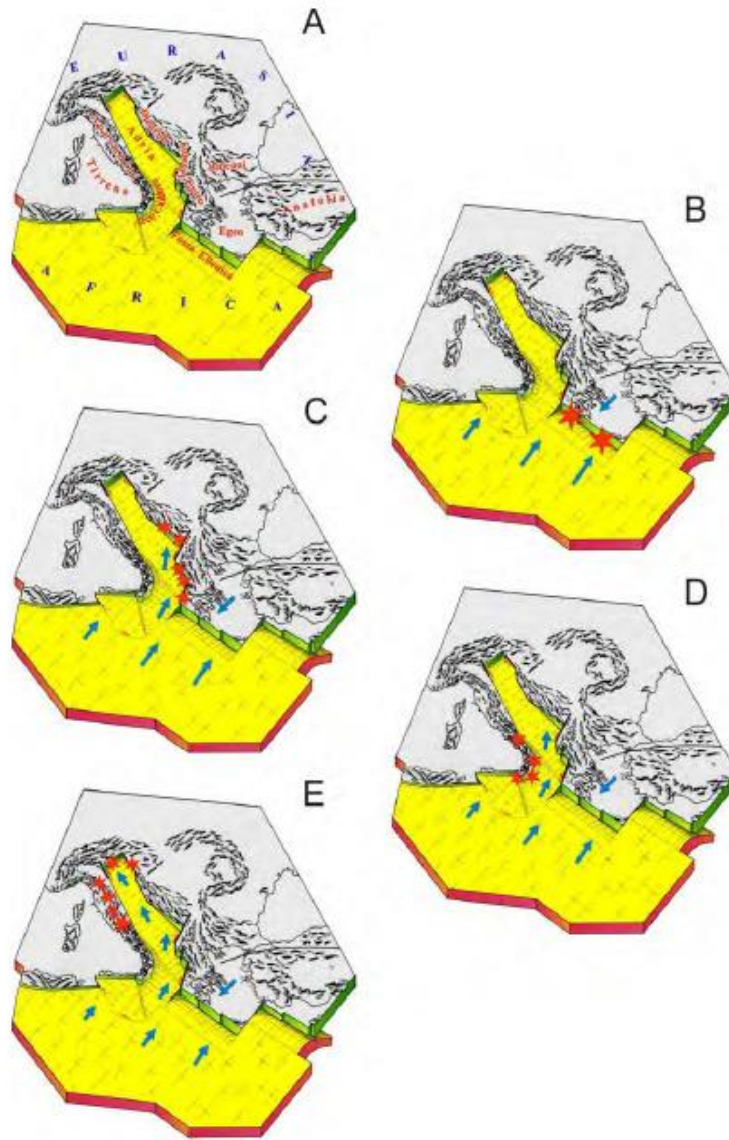
# Table of Contents

Table of Contents.....	3
1. SEISMOLOGICAL ASPECTS .....	4
1.1. Global tectonics .....	4
1.2. The seismic sequence .....	9
1.3. Historical seismicity .....	13
1.4. The May 20 <sup>th</sup> , 2012 event .....	14
1.5. Shake maps.....	15
1.6. Recordings and response spectra .....	19
1.7. Preliminary ground response analysis at Mirandola .....	26
2. LIQUEFACTION EFFECTS .....	30
2.1. Hydro-geological framework .....	30
2.2. Historical cases of liquefaction .....	32
2.3. Effects of liquefaction at San Carlo .....	35
2.4. Available geotechnical information.....	41
2.5. Preliminary assessment of liquefaction susceptibility.....	44
3. GEOPHYSICAL TESTING .....	47
3.1. Objectives of geophysical testing .....	47
3.2. Seismic data acquisition.....	49
3.3. Data Analysis and Results.....	49
3.4. Remarks .....	60
References .....	61
Appendix .....	63

# 1. SEISMOLOGICAL ASPECTS

## 1.1. Global tectonics

The Italian seismicity is mainly due to the movement of the African plate in the North direction and the consequent (continent to continent) collision with the Euro-Asiatic plate. Figure 1 shows a tectonic sketch of the Central Mediterranean basin and the associated plate movement. In the North-East, the Adriatic (micro) plate is a geologic structure playing a key role in the observed seismicity of that part of the Italian Peninsula. This is the remains of a large African promontory that in ancient times occupied most of the actual Central-Western Mediterranean basin (Mantovani et al., 2011). In its Northern part, the Adriatic plate collides with the Euro-Asiatic margin along the oriental Alps, giving rise to systems of inverse faults and to moderate to high seismicity. Some of the most significant earthquakes in this zone (e.g. Friuli earthquake, 1976-77) are due to the subduction of the Adriatic plate beneath the Oriental Alps. A sketch of the tectonic setting and kinematics compatible with the observed deformations of the Central part of the Mediterranean basin is shown in Figure 2. The available geodetic data retrieved from a dense GPS permanent network allows to define a detailed picture of the deformation of Central-Northern Italy. Figure 3 shows the horizontal velocity field (with respect to Euro-Asiatic plate) obtained from measurements of 177 GPS stations for an observation period greater than 1 year.



**Figure 1** Simplified tectonic sketch of the Central Mediterranean area. (a) The African plate (yellow) and the interaction zones with the Anatholic-Aegean-Balcanic system. (b) After intense earthquakes in the Hellenic trench (red stars), the African-Ionic front and the Adriatic plate accelerate (blue arrows), increasing the tectonic load on the interaction zones between the Adriatic plate and the Hellenic-Adriatic chain of mountains, where strong earthquakes are frequent. (c) The acceleration in the Ionic area, after strong earthquakes (red stars), increases the stresses and the probability of strong earthquakes increases even in the interaction zone with the Calabrian arch. (d) The seismic events let the plate to accelerate northward (with velocities controlled by the post-seismic readjustment). (e) The adjustment provokes an increase in tectonic loading on the interaction zones between the northern-Adriatic front and the surrounding parts. (Mantovani et al., 2011)

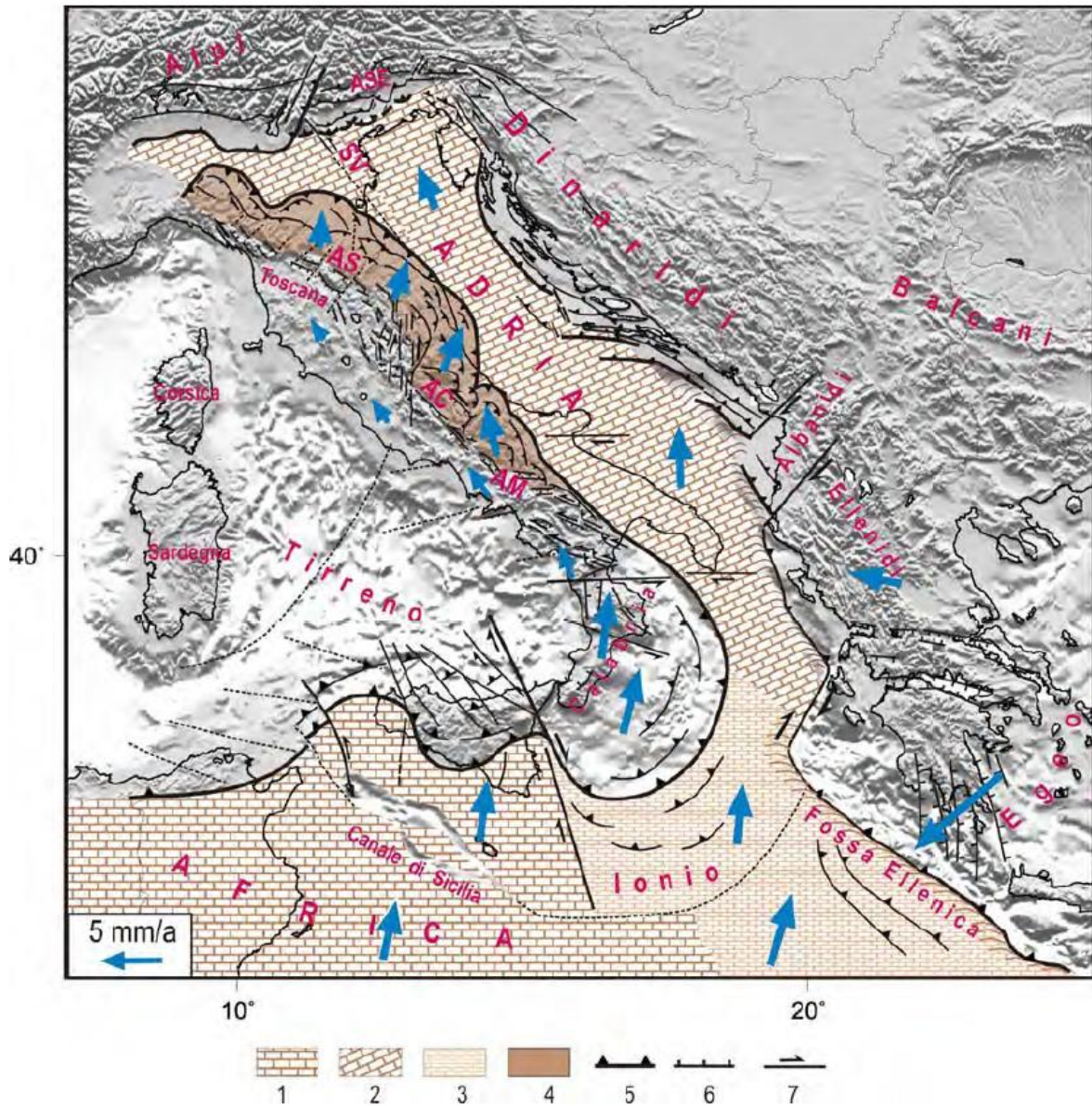


**Figure 2** Tectonic setting and kinematics of the blocks in the central part of the Mediterranean basin compatible with the post-Pleistocene deformation field (Mantovani et al, 2011). 1-2 African and Adriatic plates, 3) Ionic plate, 4) external part of the Apennine chain carried by the Adriatic plate, 5, 6, 7) main tectonic compressive features. The blue arrows show the long term kinematic situation (medium post-Pleistocene) with respect to the Eurasian. AM=Southern Apennines, AC= Central Apennines, AS=northern Apennines, ASE=Southern-east Alps, SV=Schio-Vicenza fault system.

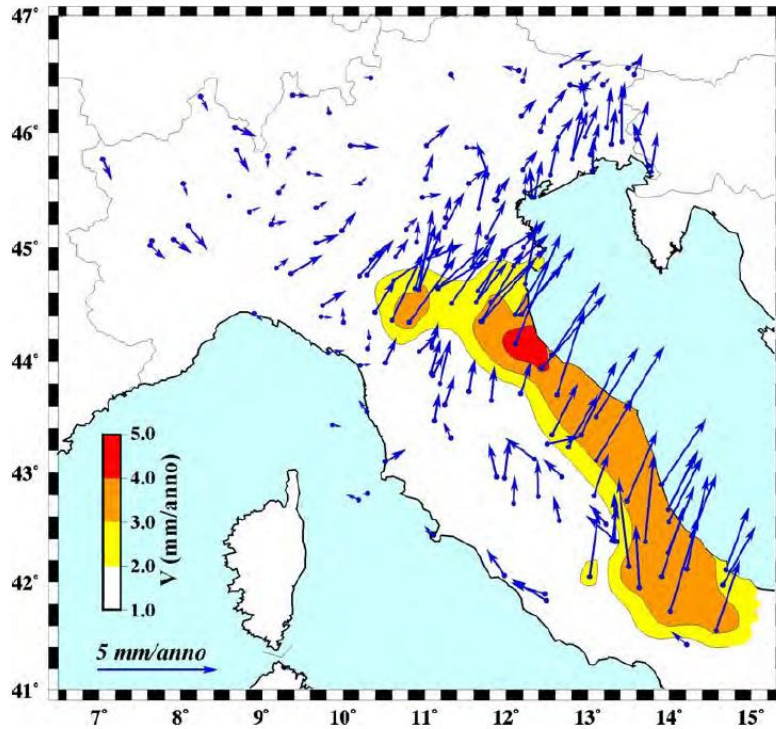


**Figure 3** Horizontal velocities in 177 permanent GPS stations after 1 year observation. The velocities are defined as proposed by Devoti et al. (2008): position 55.85° N, -95.72° E; rotation velocity  $\omega = 0.266^\circ/\text{Ma}$ . The position of the contours is plotted by interpolating the data available with the finite element procedure. (Mantovani et al., 2011)

The area struck by the Emilia May 2012 sequence is located South of the Po Plain, the foreland basin of two mountain belts: the Alps and the Northern Apennines. Under thick clastic sedimentary fills, along the Northern and Southern margins of the Po Plain, are buried several thrust sheets and tectonic structures (Figure 4). Due to fast sedimentation rates and comparatively low tectonic rates, the thrusts are generally buried and the surface evidence of their activity is faint (Toscani et al., 2009).

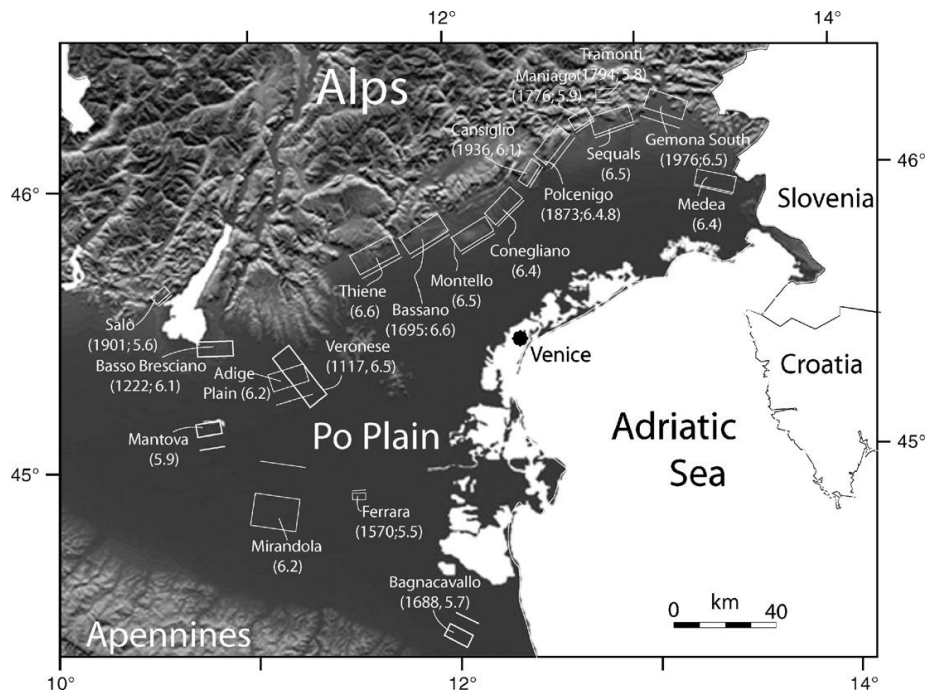


**Figure 4** Tectonic map showing the location and extension of potentially active faults in the Po Plain area. In parenthesis, the year of the last known large earthquake associated to the fault (if known), and the maximum expected magnitude (Carminati et al., 2007).

Figure 5 shows a tectonic map of the Po Plain, with the main faults and seismogenic sources and two structural sections between Bologna and Ferrara analyzed by Toscani et al. (2009). The authors correlate the seismicity both with the outer buried front and with the inner Pedeappenninic Trust front. Figure 5b shows the seismogenic sources associated with the largest historical earthquakes ever recorded.

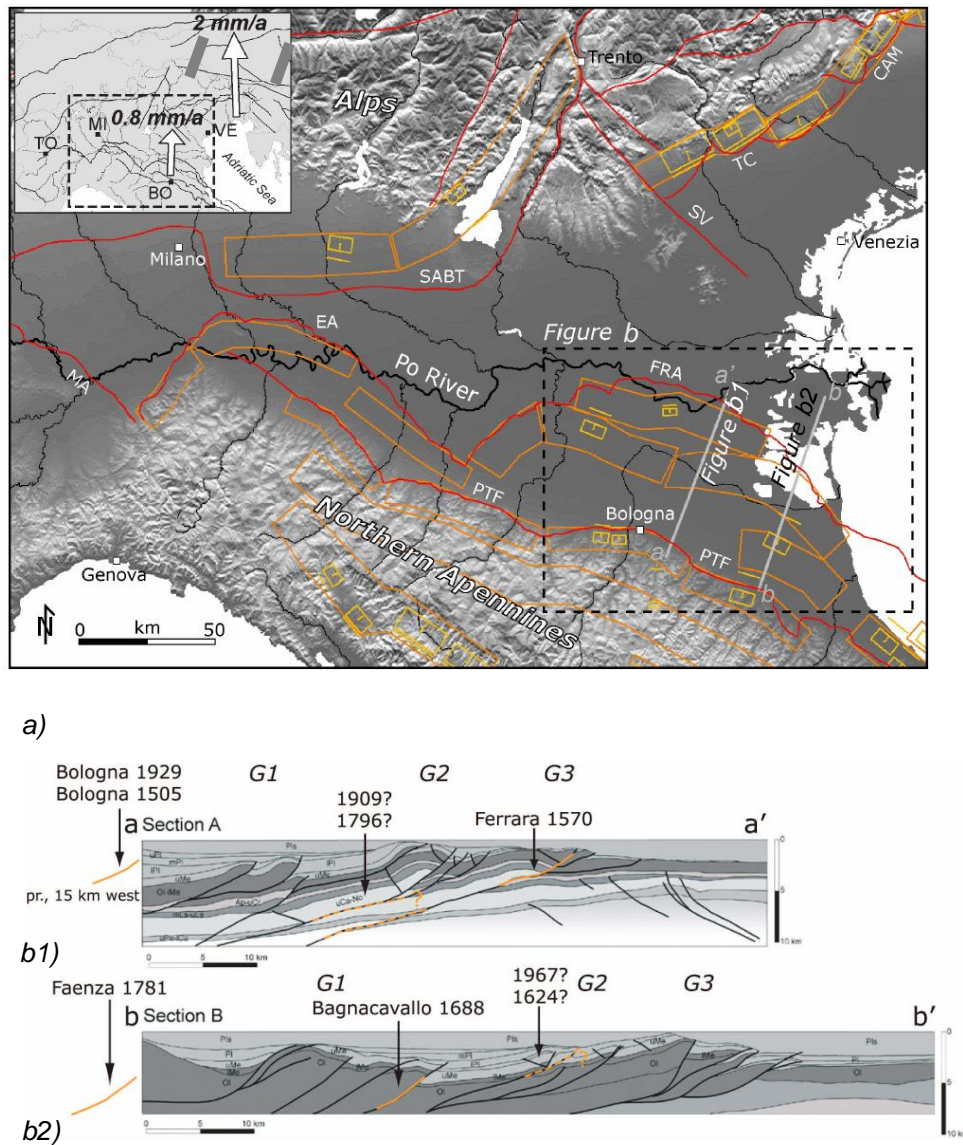


**Figure 5 (a)** Simplified tectonic map of the Po Plain and the surrounding regions showing the Northern Apennines and Southern Alps main thrusts and faults as red lines. Yellow and orange polygons are the individual seismogenic sources and seismic areas respectively from DISS database (DISS working group, 2007) (Toscani et al., 2009). The cross sections a-a' (b1) and b-b' (b2) show the seismogenic sources associated with the past largest earthquakes of the area of interest (DISS Working group, 2007) interpreted in the light of the results obtained in the study of Toscani et al. (2009).

Under the Po Plain lie sediments of the Ferrarese dorsal, which has generated the Emilia seismic sequence. This is constituted by the northern structures of the Apennines, which, during the last hundreds of thousands of years, moved forward North-East. This movement generated a mechanism such that the front of the chain generates compression and structural shortening, while the back part is divergent and generates tension. In the Ferrara proximity there are three consecutive systems at a distance of 10-15 km: the oldest and backlog is at the foots of the Apennines, near Bologna, while the most advanced and recent is on the North-East part of the Ferrarese dorsal.

## 1.2. The seismic sequence

Figure 6 shows the location on the Po Plain of the seismic sequence of May-June 2012. Figure 7 illustrates the number of earthquakes, which occurred in this area from May 19 through June 5 as function of magnitude  $M_L$ . The sequence is still in progress. Furthermore, Figure 8 shows the spatial distribution of the epicenters: orange dots represent the events from May 19<sup>th</sup> to June 28<sup>th</sup>; the red dots represent the earthquakes occurred from June 28<sup>th</sup> to July 5<sup>th</sup>. The seven stars represent the events with magnitude ( $M_L$ ) greater than 5. Two of them are events with  $M_L$  greater than 5.5: the main shock (5.9  $M_W$ ) occurred on May 20, 2012 causing 7 fatalities, significant damage to historic structures, churches, industrial buildings and leaving 7000 people homeless. On May 29<sup>th</sup> 2012 a  $M_W$  5.65 shock hit the region causing further damage and fatalities. At present (July 13, 2012) the death toll stands at 27, hundreds were injured and approximately 16.000 were left homeless from the two combined events.



Figure 6 Location on the Po Plain (Northern Italy) of the seismic sequence of May-June 2012.

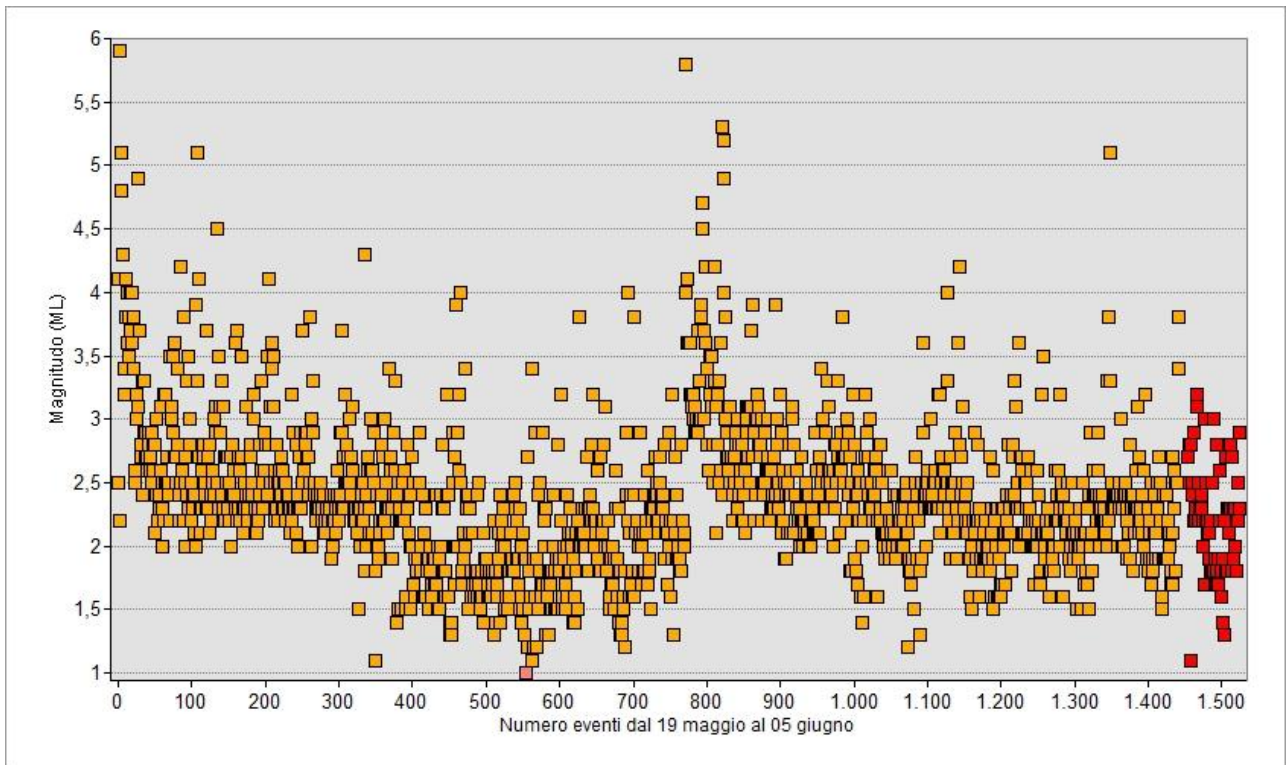


Figure 7 Number of earthquakes as a function of magnitude  $M_L$ . Red dots represent the events occurred within 24 hours from June 4 through June 5 (INGV, <http://www.ingv.it/>).

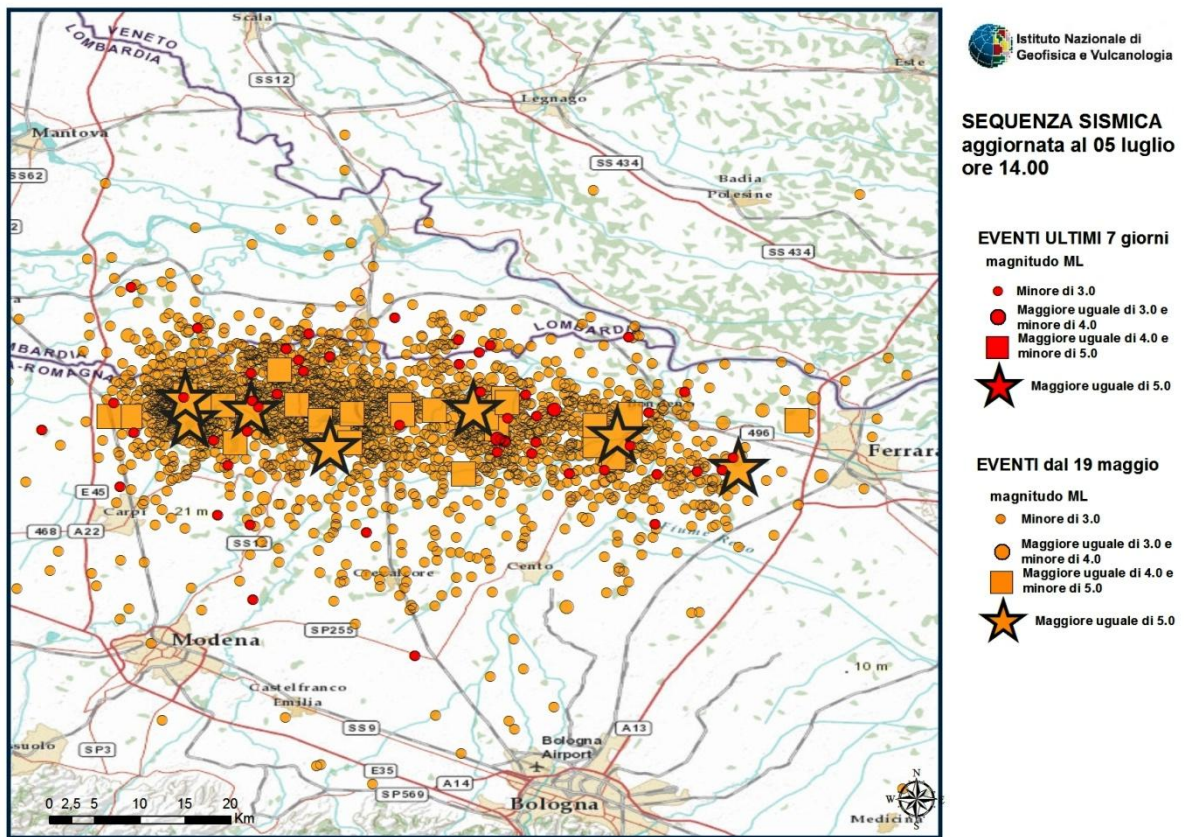


Figure 8 Spatial distribution of the epicenters of the seismic sequence (INGV, <http://www.ingv.it/>).

A preliminary source model (Figure 9) was proposed by Atzori et al. (2012) representing the geometry of two structures that generated the events of May 20th and May 29th. The figure shows the slip distribution inferred mostly from seismological and tectonic data and to a certain extent also SAR interferogram data. The green stars are events with magnitude between 5.8 and 5.9 (main shocks) while green dots are events with magnitude between 5.1 and 5.3. Black dots represent the foreshocks and aftershocks. Figure 10 shows a map of static ground displacement, which occurred between May 27 and June 4 in the area of Mirandola (Atzori et al, 2012), as obtained from SAR interferogram.

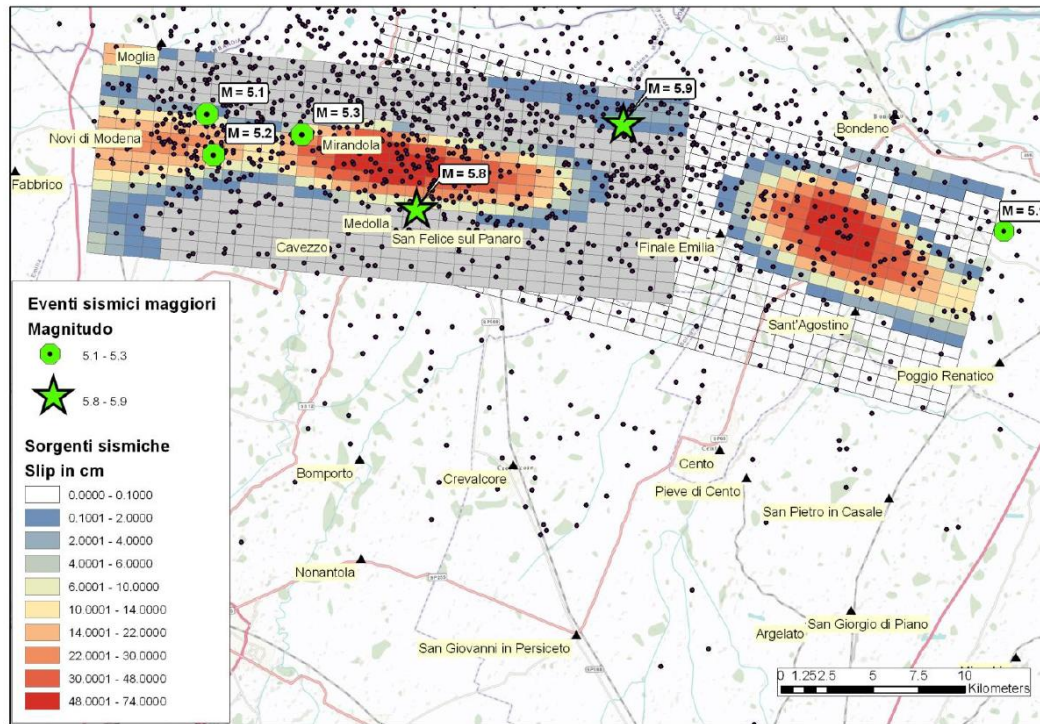


Figure 9 Preliminary model of the seismic sources of May 29 event of the Emilia earthquake (Atzori et al, 2012).

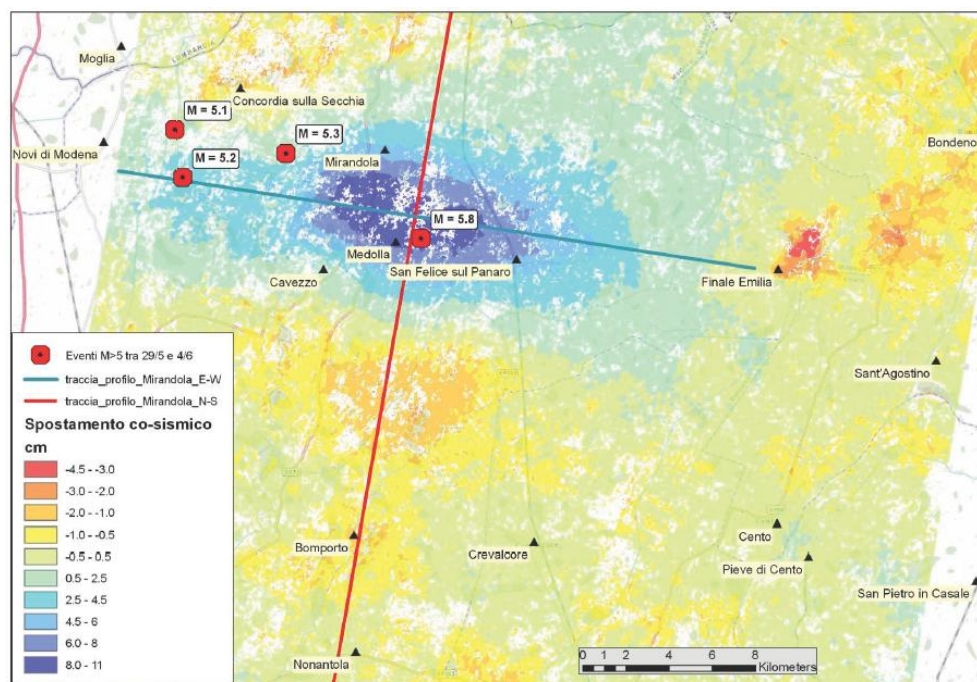


Figure 10 Map of total ground displacement, which occurred between May 27 and June 4 in the area of Mirandola. The green and red traces represent EW and NS cross-sections shown in Figure 11 (Atzori et al, 2012).

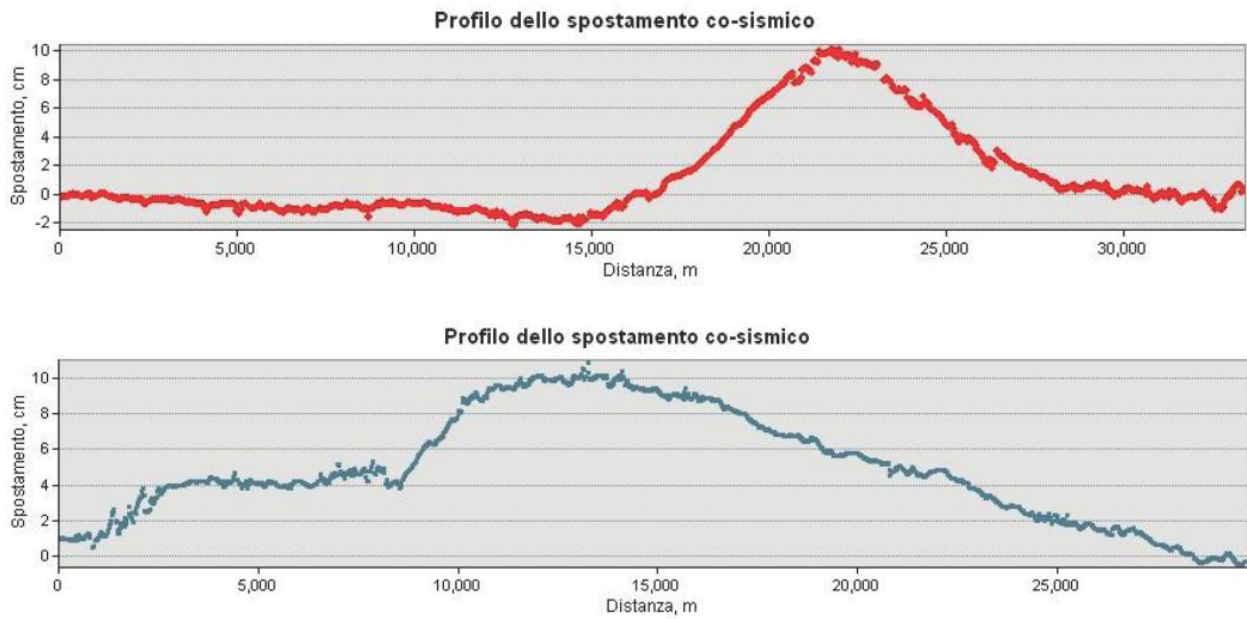
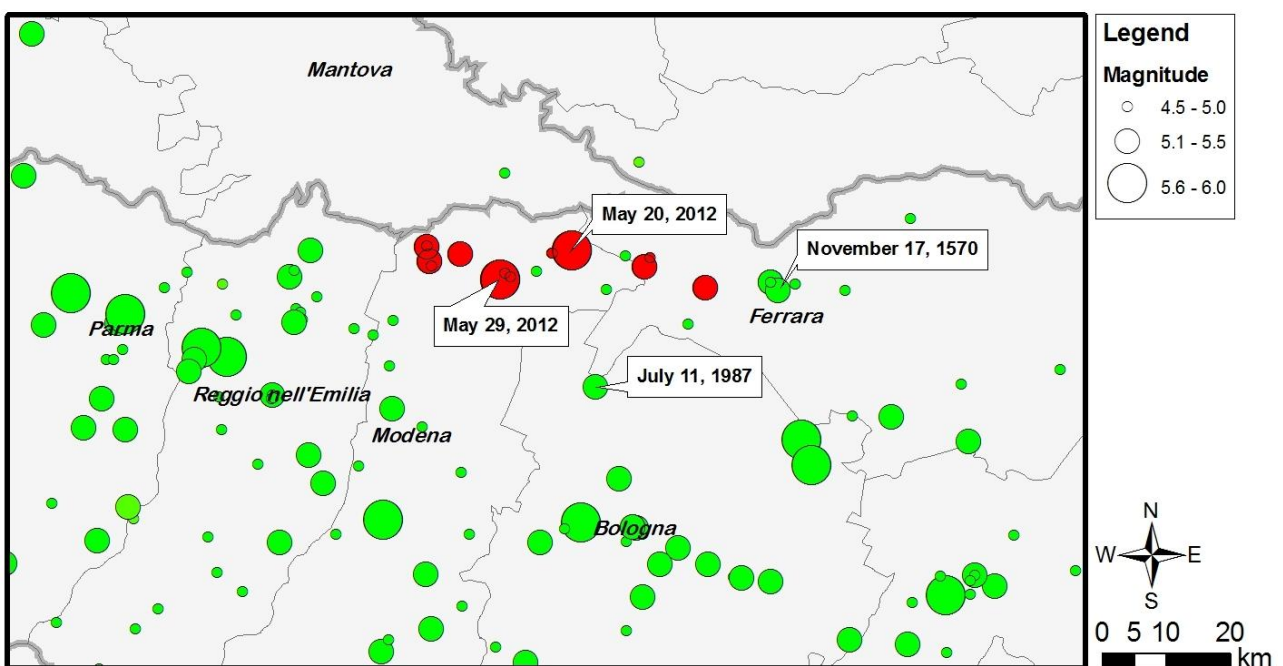


Figure 11 *Top*: Profile of total ground displacement along the NS cross-section shown in Figure 10 (South is on the left of the profile). *Bottom*: Profile of total ground displacement along the EW cross-section shown in Figure 10 (West is on the left of the profile). (Atzori et al, 2012)

### 1.3. Historical seismicity

Figure 12 shows a map with the epicentres of the most important earthquakes, which have occurred in the Northern part of the Emilia-Romagna Region in the latest 500 years (green points). The data were retrieved from the Italian earthquake catalogue CPTI1 of INGV (Istituto Nazionale di Geofisica e Vulcanologia, <http://emidius.mi.ingv.it/CPTI11/>). The Ferrara territory was hit by a M5.5 earthquake (magnitude estimated from macroseismic data) on November 17, 1570. On July 11, 1987 a M5.4 event struck the Po Plain area close to Bologna and Ferrara. Other earthquakes occurred in the Southern part of the Emilia-Romagna Region, close to the Apennine Mountains. The magnitude of these events reached a magnitude up to 6. Figure 12 shows also the events with magnitude greater than 4.5 (red points) of the seismic sequence of May-June 2012 (data retrieved from <http://iside.rm.ingv.it/>).



**Figure 12** Distribution of the major historical earthquakes (green points) retrieved from the CPTI1 catalogue (<http://emidius.mi.ingv.it/CPTI11/>) and of the events with  $M > 4.5$  (red points) of the seismic sequence of May-June 2012 (<http://iside.rm.ingv.it/>).

## 1.4. The May 20<sup>th</sup>, 2012 event

At 02:03:52 UTC (04:03 local time) of May 20<sup>th</sup>, 2012 a strong shaking was felt in the Emilia-Romagna Region, in Northern Italy. The magnitude estimates for this event are reported in Table 1. The epicenter was characterized by coordinates 44.89° (latitude) and 11.23° (longitude). The depth of the hypocenter has been estimated as 6.3 km (INGV). The focal mechanism is that associated with a thrust rupture. Figure 13 shows the mechanisms of the events, which occurred from May 20 through May 23. They had a magnitude ranging from 3.4 to 5.9. The movement involved East-West oriented faults with North-South compression.

**Table 1** Seismological characteristics of the May 20<sup>th</sup>, 2012 event in Emilia Romagna region, Northern Italy (INGV).

Magnitude ( $M_w$ )	5.9	<a href="#">INGV</a>
Date and time	20/05/2012 – 02:03:52 (UTC)	<a href="#">INGV</a>
Epicentral coordinates	Lat: 44.89°N – Long: 11.23°E	<a href="#">INGV</a>
Depth (km)	6.3	<a href="#">INGV</a>
Focal mechanism of main shock	Reverse fault	<a href="#">INGV</a>

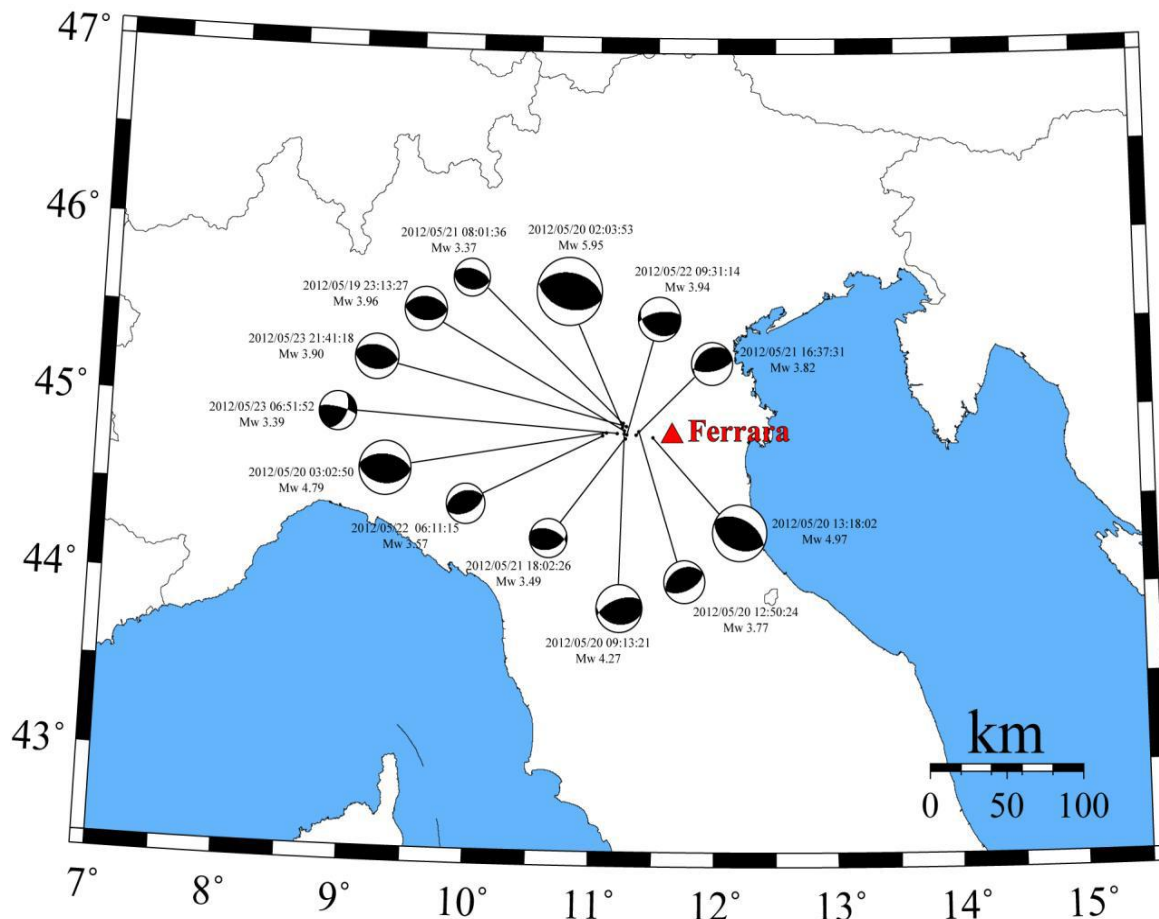


**Figure 13** Focal mechanism of events with magnitude ranging between 3.4 and 5.9, which occurred from May 20 to May 23. These focal mechanisms show a compressive movement on approximately East-West oriented faults and North-South compression. (INGV, <http://www.ingv.it/>)

## 1.5. Shake maps

Figure 14 shows the location of the recording stations of the Italian Strong Motion Network (RAN) and the Strong Motion Network of Northern Italy (RAIS). Figure 15 shows the peak ground accelerations (PGA) recorded at the stations located in the area close to the epicenter. The maximum PGA is recorded at station of Mirandola (MRN) and is associated to the vertical component. The other peak values of the recordings are associated to one of the two horizontal components. Figure 16 shows a shake map computed by interpolating the recorded PGA at the RAN stations. To a first approximation the stations are located at sites characterized by similar soil category (Soil Type C according to the ground classification of Italian Building Code, NTC, 2008). More information about the soil categories of the stations belonging to the Italian strong-motion network can be retrieved at the portal <http://itaca.mi.ingv.it/ItacaNet/>.

From Figure 16 it is worth noticing that the pattern of the iso-contours of PGA is non-symmetric with respect to the epicenter. This is due to the small number of stations used to perform the interpolation (the station closest to the epicenter is MRN). The fault mechanism may have also played a role in this asymmetry. This map provides a first estimate of the ground motion caused by the May 20 quake.

The recordings provided by the RAN and RAIS networks have been compared with the estimates of recent two ground motion predicting equations (GMPE) one of which was developed using Italian strong-motion data. Figure 17 and Figure 18 show the horizontal PGA predicted by the GMPE developed respectively by Cauzzi and Faccioli (2008) and Bindi et al. (2011). The selected GMPEs define the ground classification of the recording sites according to the current European (CEN 2004) seismic codes, on which the soil categories of Italian Building Code (NTC, 2008) are based. The predictions have been made, preliminarily, for Soil Type C. The predicted PGA values are in agreement with the recordings from the RAN and RAIS networks. Figure 19 shows the vertical component of PGA predicted by Bindi et al. (2011). This GMPE grossly underestimates the vertical PGA recorded at Mirandola (MRN) station.

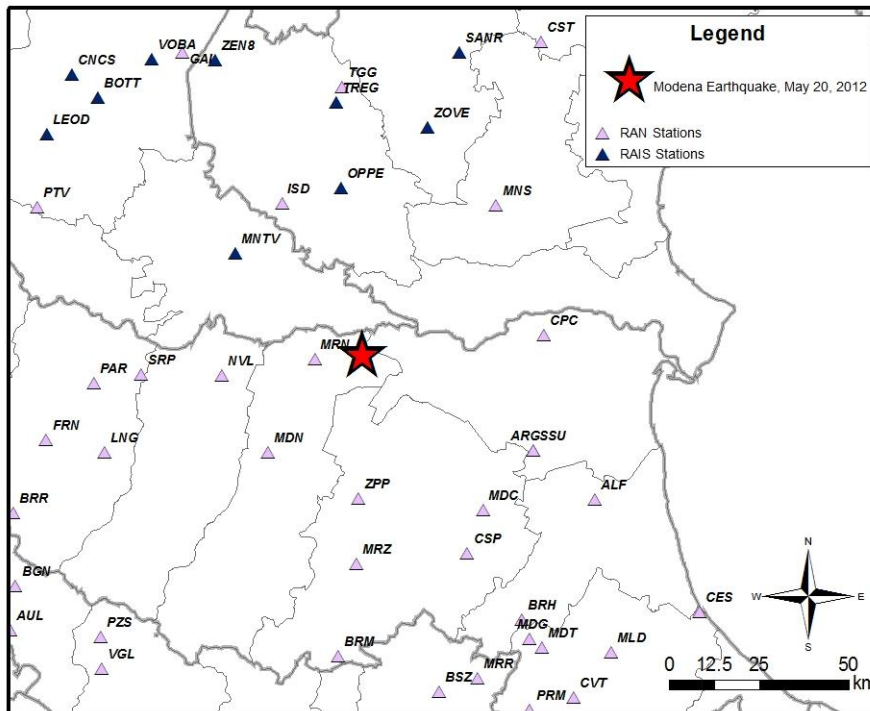


**Figure 14** Location of the May 20<sup>th</sup> epicenter and of the recording stations of the Italian Strong Motion Network (RAN) and the Strong Motion Network of Northern Italy (RAIS).

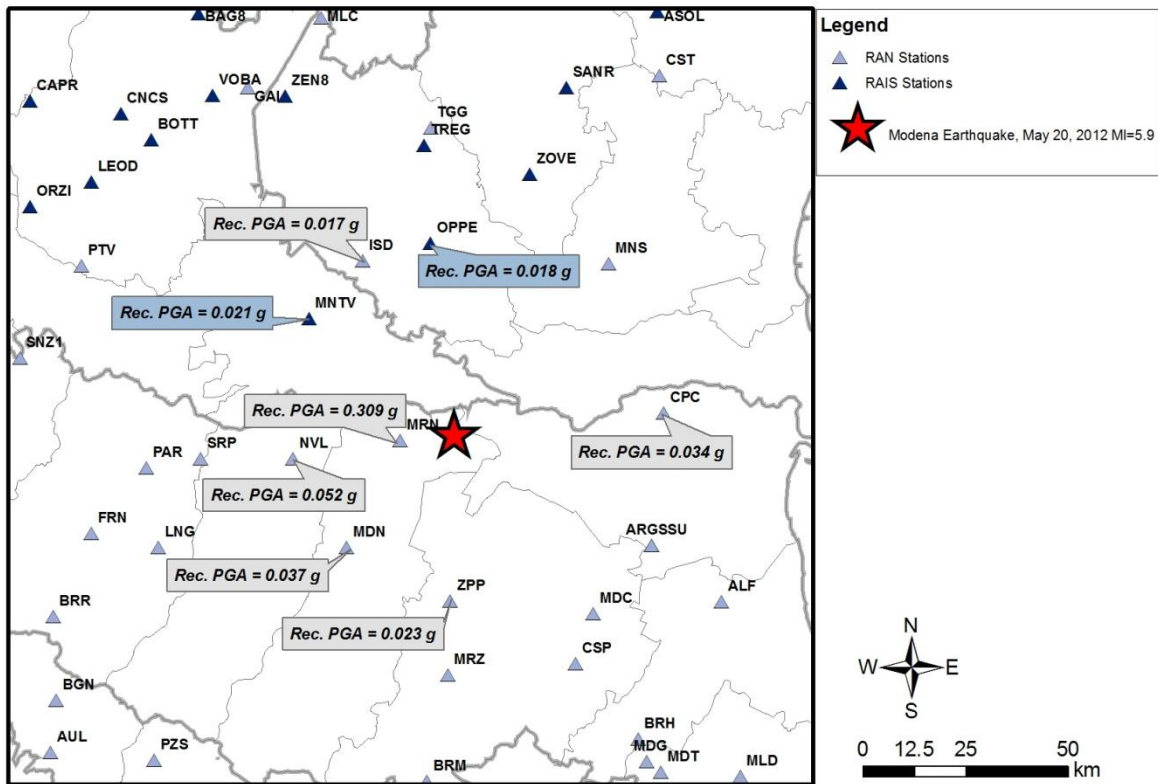


Figure 15 Maps of recorded PGA (g) at the stations of the Italian Strong Motion Network (RAN) and the Strong Motion Network of Northern Italy (RAIS).

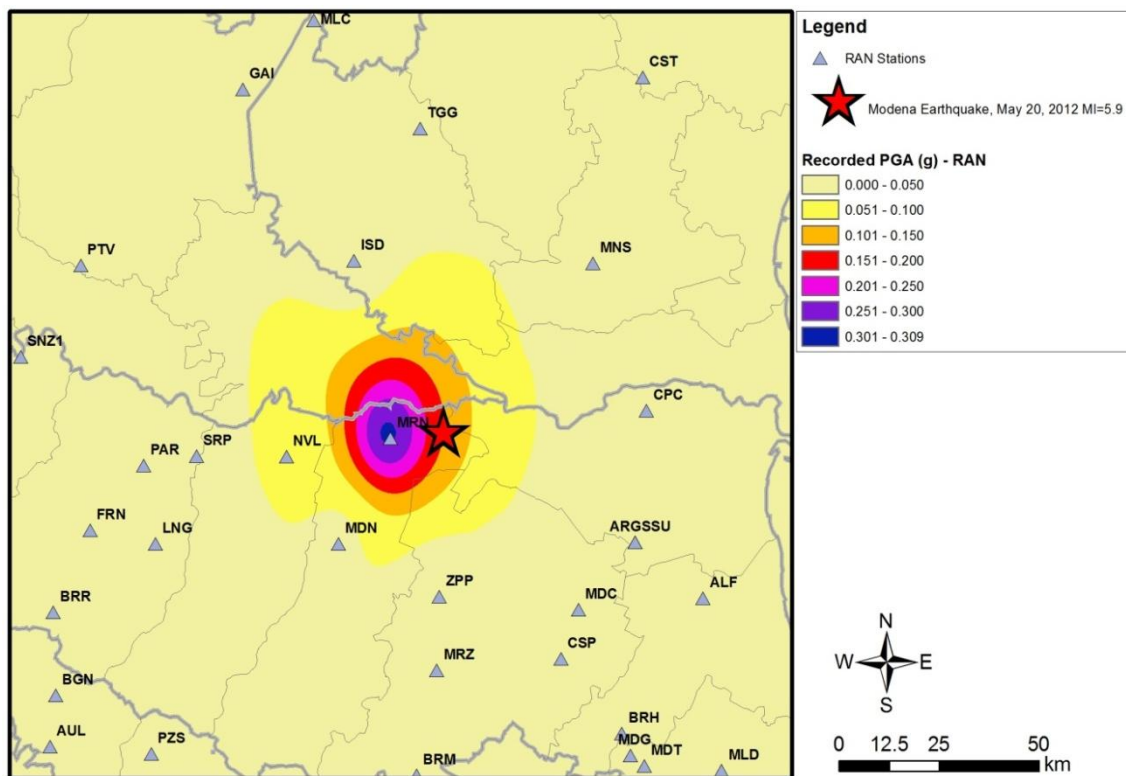


Figure 16 Shake map obtained from the interpolation of PGA recorded by the RAN seismic network. Ground conditions for the seismic stations are similar and approximately associated to Soil Type C according to ground classification of the Italian Building Code (NTC, 2008).

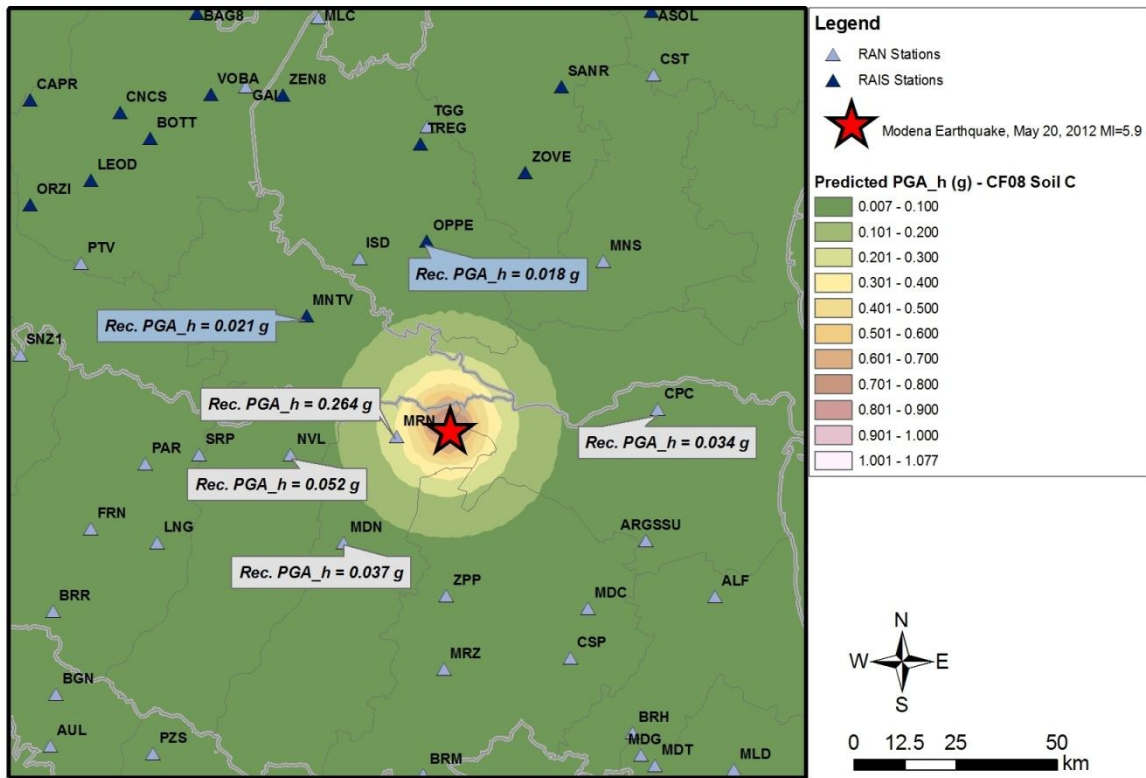


Figure 17 Median values of PGA (horizontal component) predicted by the GMPE of Cauzzi and Faccioli (2008) for Soil Type C, plotted on top of the recorded values of PGA at selected recording stations of the RAN and RAIS Italian strong motion networks.

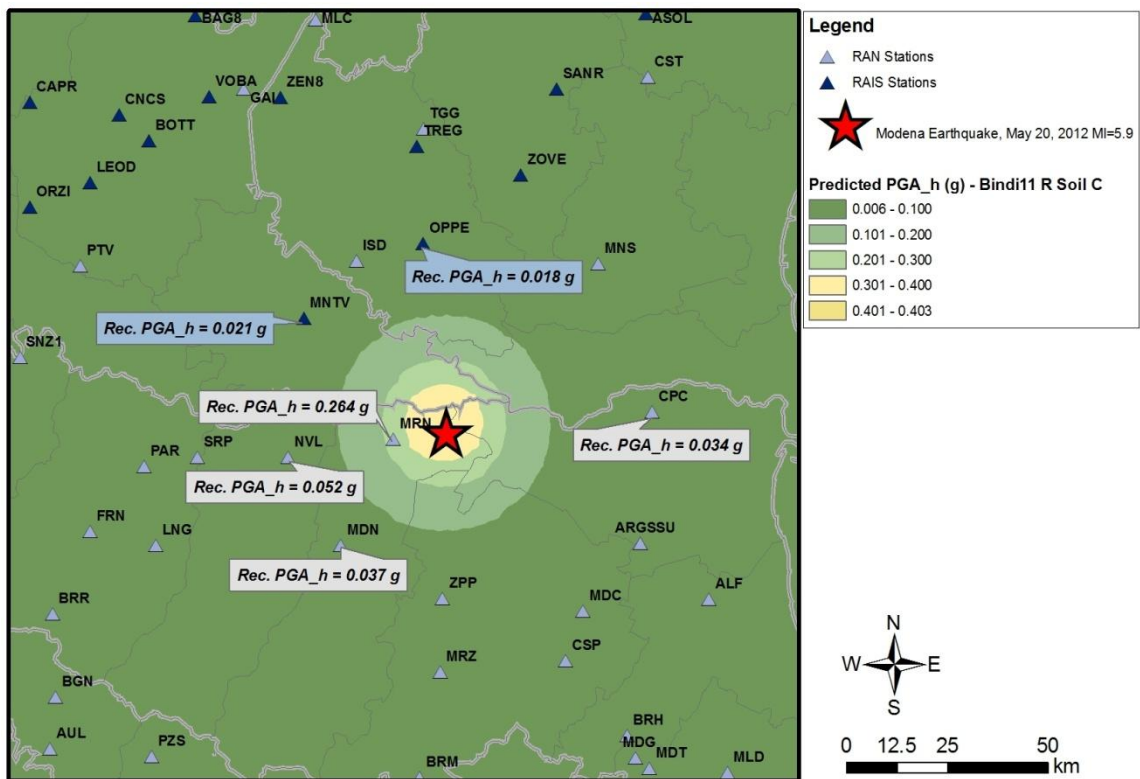


Figure 18 Median values of PGA (horizontal component) predicted by the GMPE of Bindi et al. (2011) for Soil Type C, plotted on top of the recorded values of PGA at selected recording stations of the RAN and RAIS Italian strong motion networks.

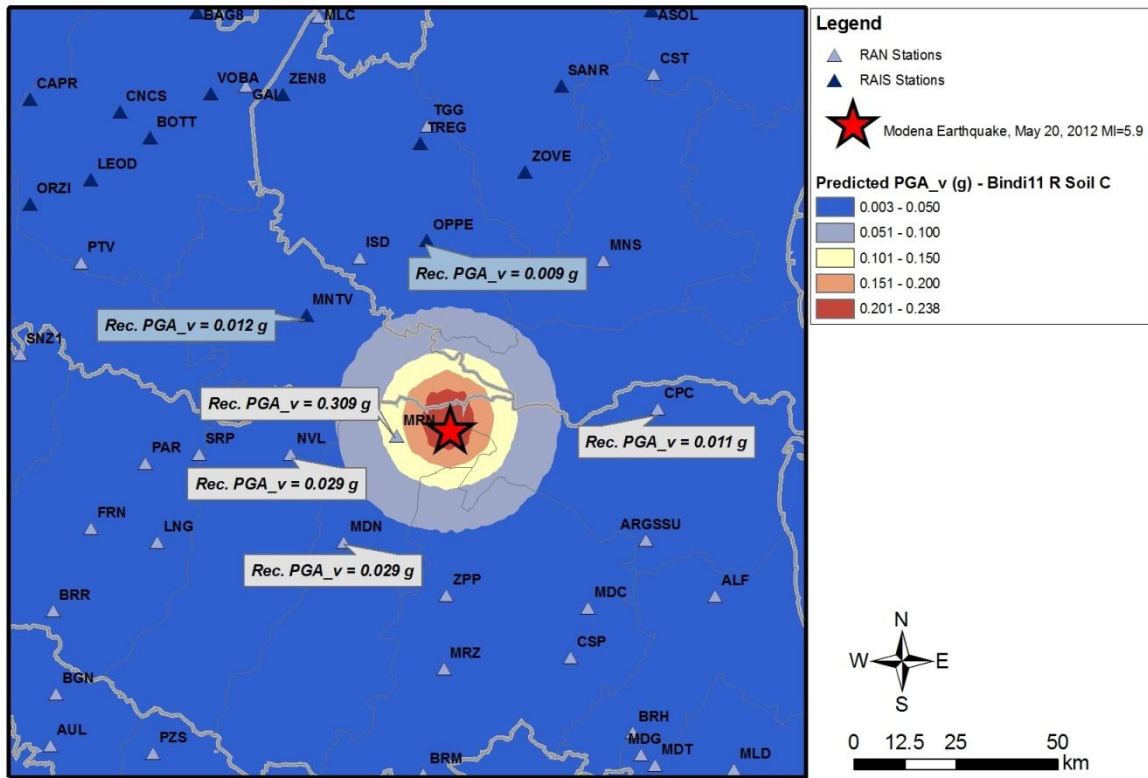
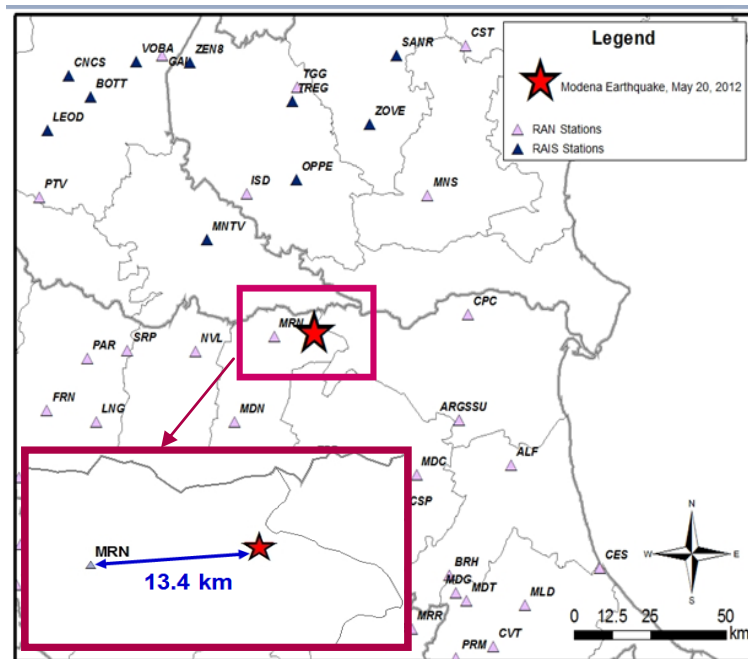


Figure 19 Median values of PGA (vertical component) predicted by the GMPE of Bindi et al. (2011) for Soil Type C, plotted on top of the recorded values of PGA at selected recording stations of the RAN and RAIS Italian strong motion networks.

## 1.6. Recordings and response spectra

The closest station to the epicenter of May 20, 2012 shock is Mirandola (MRN). The epicentral distance of this station is about 13.4 km (Figure 20). Figure 21 and Figure 22 show the acceleration, velocity and displacement time histories of the South-North (SN) and East-West (EW) components, respectively, with their corresponding response spectra. Figure 23 shows the analogous plots for the vertical (UP) component. Table 2 contains the “peak ground motion” parameters, which are Peak Ground Acceleration (PGA), Peak Ground Velocity (PGV) and Peak Ground Displacement (PGD), for each component recorded at MRN station. The recorded signals have been processed for standard baseline correction, band-pass filtered from 0.05 to 50 Hz, tapered and linearly de-trended in velocity. A comparison between acceleration, velocity and displacement response spectra is illustrated in Figure 24 for the three recorded components (SN, EW e UP). It is worth noticing that the maximum PGA recorded at this station is associated with the vertical component. In terms of the acceleration response spectrum, this component presents the highest peak at a lower frequency (0.06 sec.) if compared with the horizontal components (SN: 0.17 sec.; EW: 0.31 sec.). Furthermore, the peak values of spectral acceleration for the vertical component are concentrated in a narrow band of periods from 0.02 to 0.12 sec., while the peaks of spectral acceleration for the horizontal components occur at a band with higher periods up to 0.5 sec. (EW) and 1.3 sec. (SN). In terms of velocity and displacement response spectra, the horizontal spectral ordinates are more severe than the vertical component.

Processed data recorded at the other RAN stations are not reported. The interested reader can find them at the clearinghouse web portal: <http://www.terremotoemilia.it/>.



**Figure 20** Location of the epicenter and of the stations of the Italian Strong Motion Network (RAN) and the Strong Motion Network of Northern Italy (RAIS). The squared area is a close-up view of the Mirandola station (MRN) which is the closest to the epicenter.

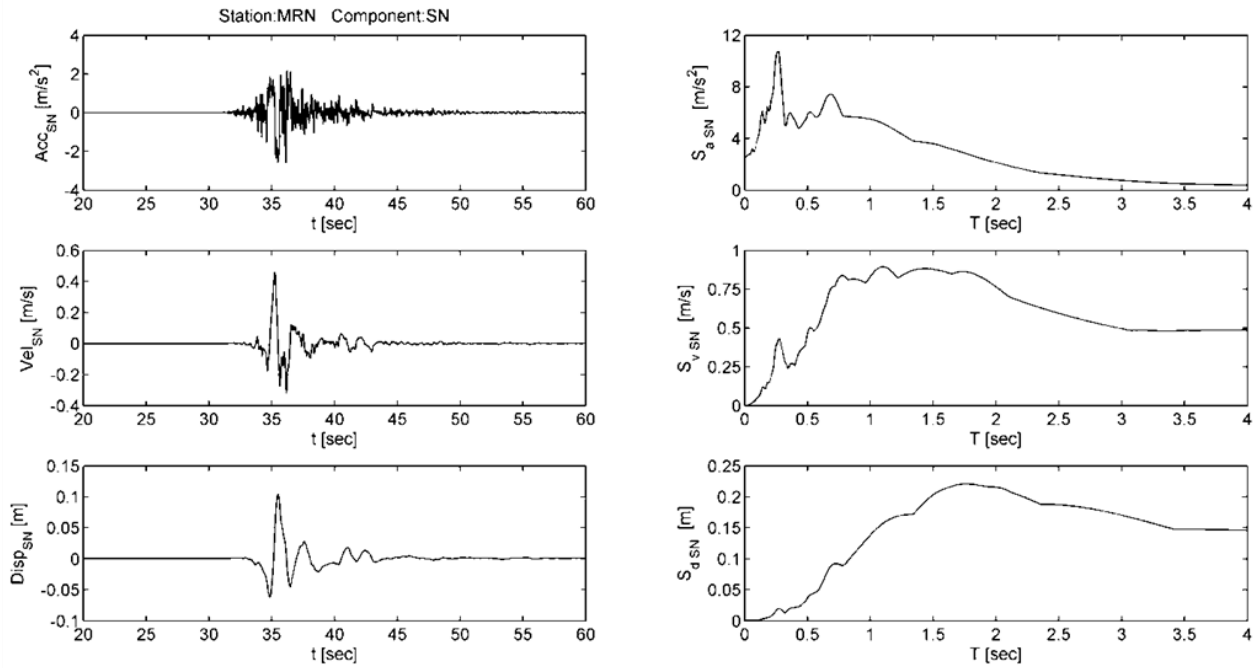


**Figure 21** Recordings at Mirandola station (MRN): acceleration, velocity, and displacement time histories associated to the South-North component (left) and corresponding relative acceleration ( $S_a$ ), velocity ( $S_v$ ) and displacement response spectra ( $S_d$ ) (right).

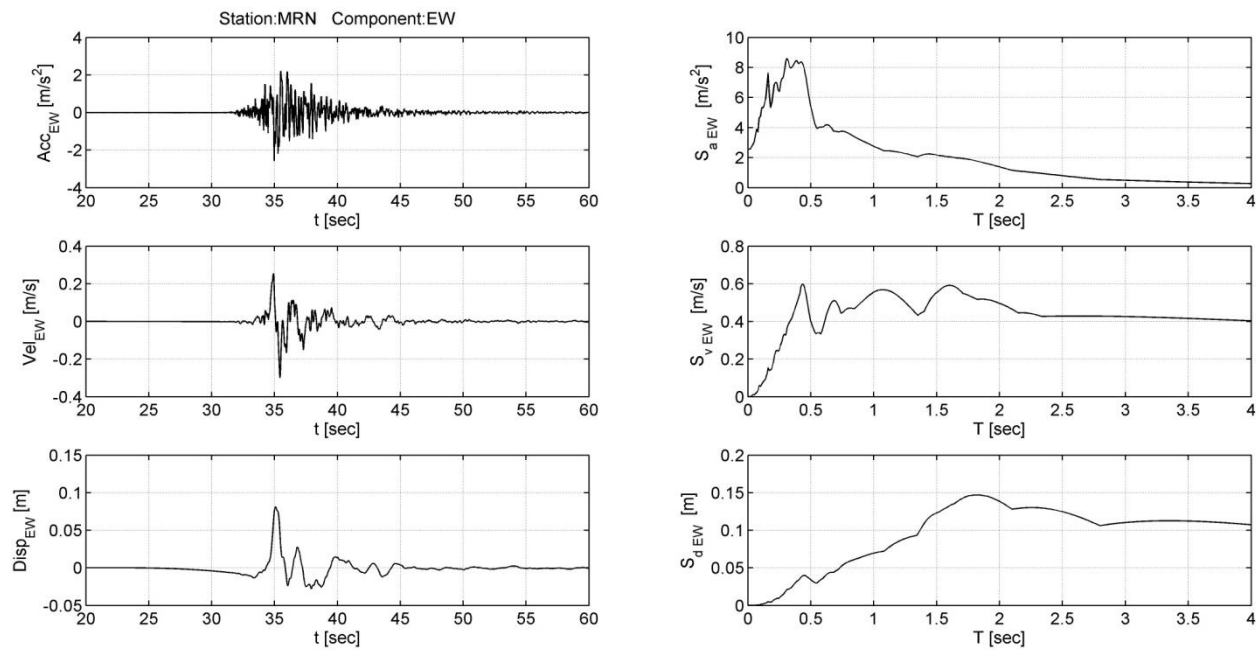


**Figure 22** Recordings at Mirandola station (MRN): acceleration, velocity, and displacement time histories associated to the East-West component (left), and corresponding relative acceleration ( $S_a$ ), velocity ( $S_v$ ) and displacement response spectra ( $S_d$ ) (right).

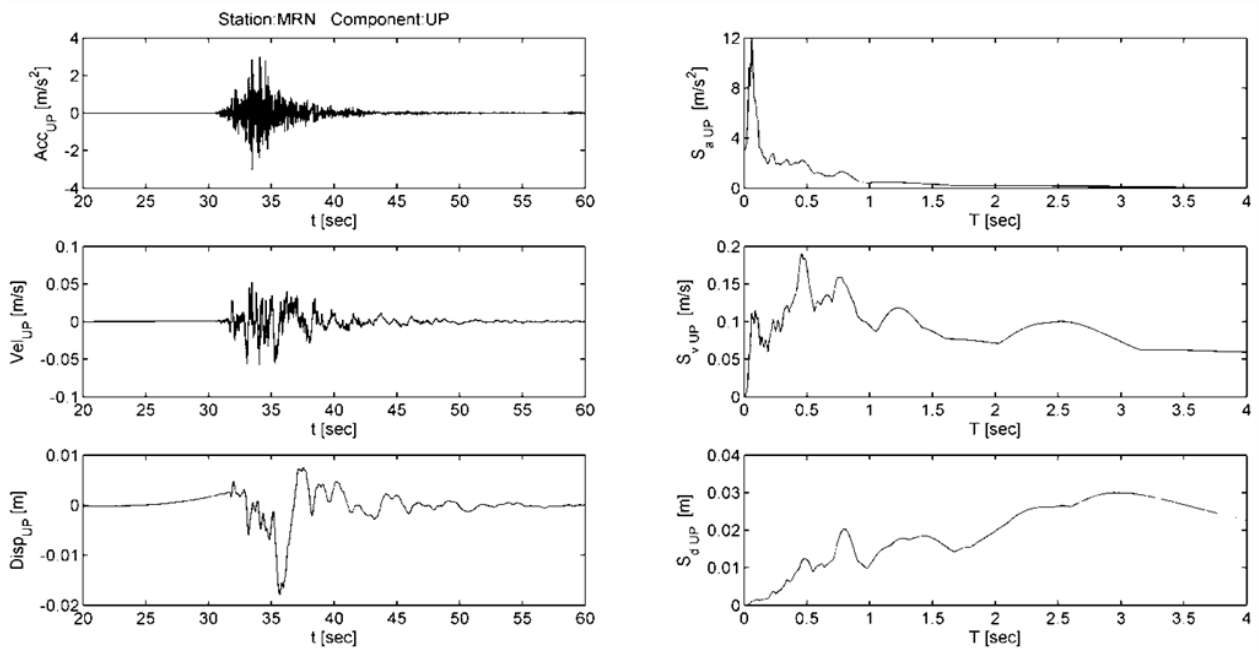


**Figure 23** Recordings at Mirandola station (MRN): acceleration, velocity, and displacement time histories associated to the vertical component (left), and corresponding relative acceleration ( $S_a$ ), velocity ( $S_v$ ) and displacement response spectra ( $S_d$ ) (right).

**Table 2** Peak ground motion parameters (PGA, PGV and PGD) for each component recorded at MRN station.

	PGA (g)	PGV (m/s)	PGD (m)
<b>SN</b>	0.264	0.463	0.105
<b>EW</b>	0.262	0.300	0.081
<b>UP</b>	0.310	0.059	0.018

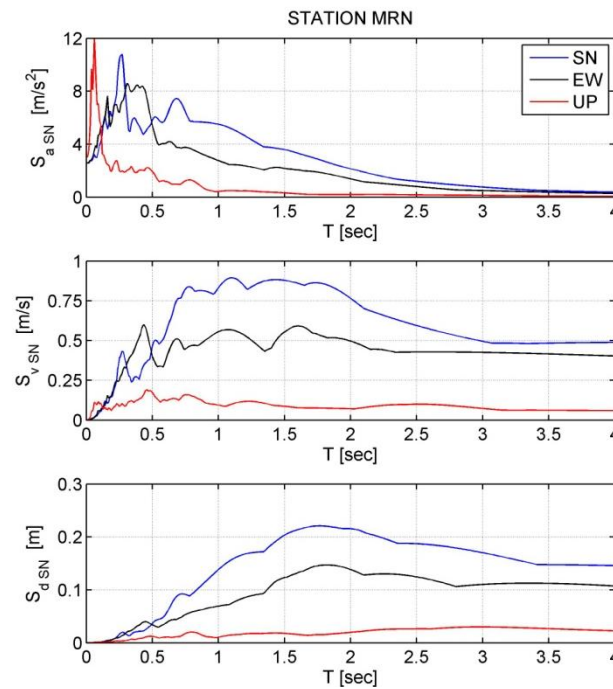


**Figure 24** Mirandola station (MRN): comparison between acceleration, velocity and displacement response spectra for the three recorded components of ground motion (SN, EW and UP).

To see the particle motions produced by the body waves and surface waves, the hodogram from station MRN has been plotted in the plane of Rayleigh wave propagation. Inspection of the MRN recordings show that P- and SV- wave arrivals are not well time-separated from the Rayleigh wave arrival given that the MRN station is very close to the epicenter. Figure 25 shows the radial and vertical displacement traces of the Rayleigh waves, obtained filtering the signals with band-pass between 0.1 Hz and 0.5 Hz.

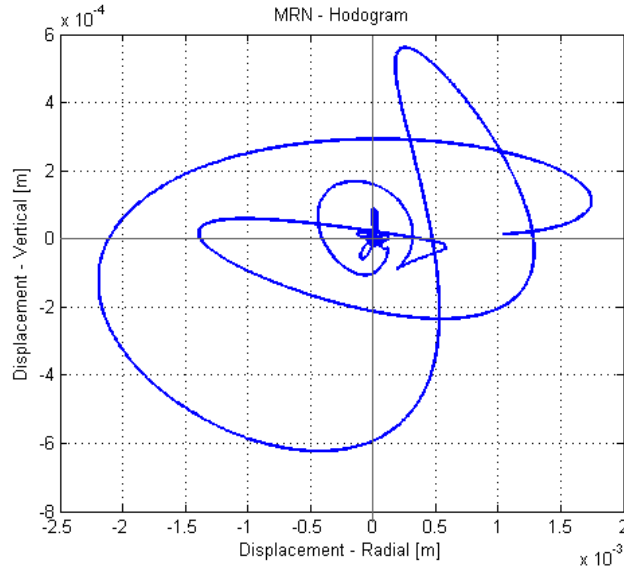


Figure 25 Hodogram from Mirandola station (MRN): the radial and vertical displacement traces.

The spectra obtained for MRN station have been compared with code (NTC, 2008) spectra, computed for both ground category C and D and for two different return periods ( $T_R$ ) equal to 475 and 975 years, in Figure 26 (horizontal component) and in Figure 27 (vertical component).

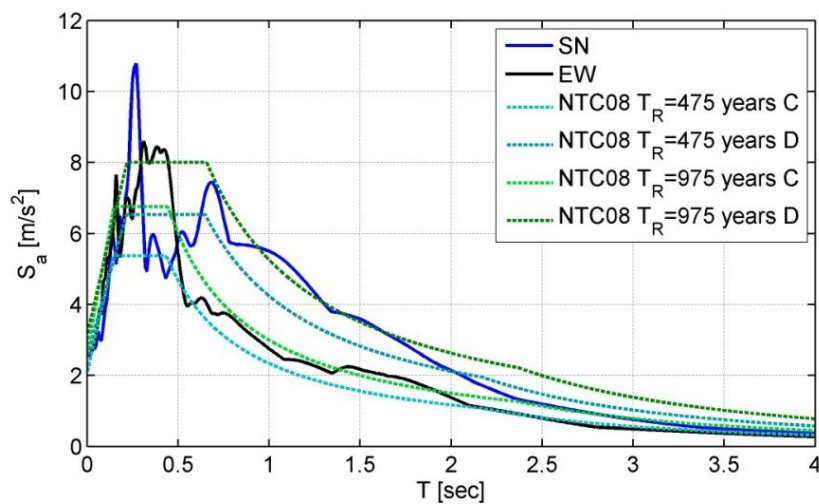


Figure 26 Mirandola station (MRN): comparison of the horizontal (SN, EW) acceleration response spectra with the horizontal code (NTC, 2008) spectra computed for soil classes C and D for 475 and 975 years.

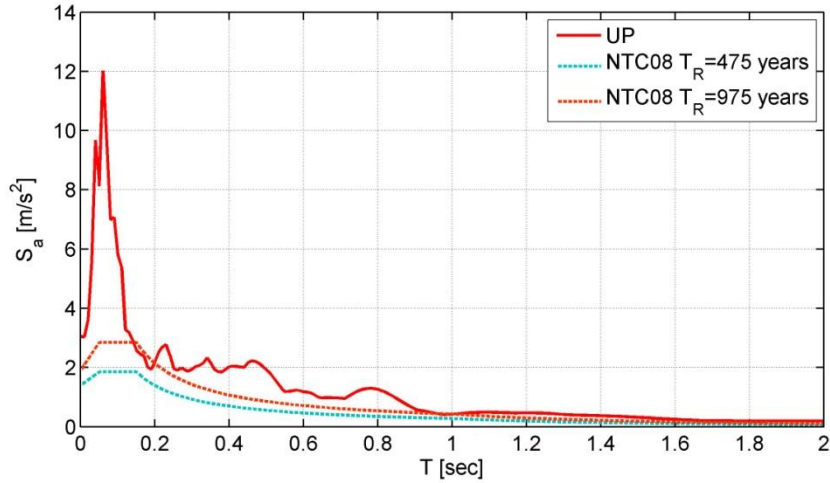


Figure 27 Mirandola station (MRN): comparison between the vertical (UP) acceleration response spectrum and the vertical code (NTC, 2008) spectra computed for 475 and 975 years.

The acceleration response spectra computed using the Mirandola station recordings have been compared with the predictions of the GMPE developed by Bindi et al. (2011) for the horizontal component and for ground category C (Figure 28). The predictions of the GMPE are satisfactory for periods less than 0.17 sec. whereas for larger periods the GMPE strongly underestimate the severity of the record.

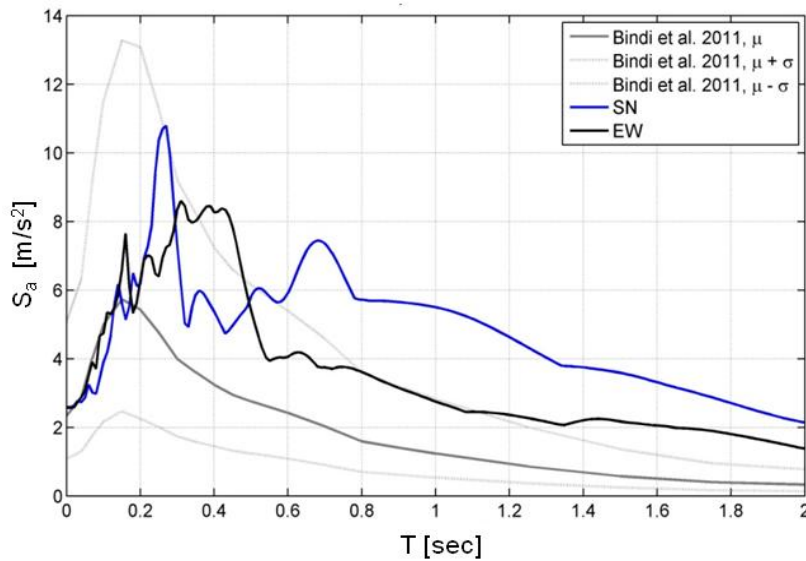
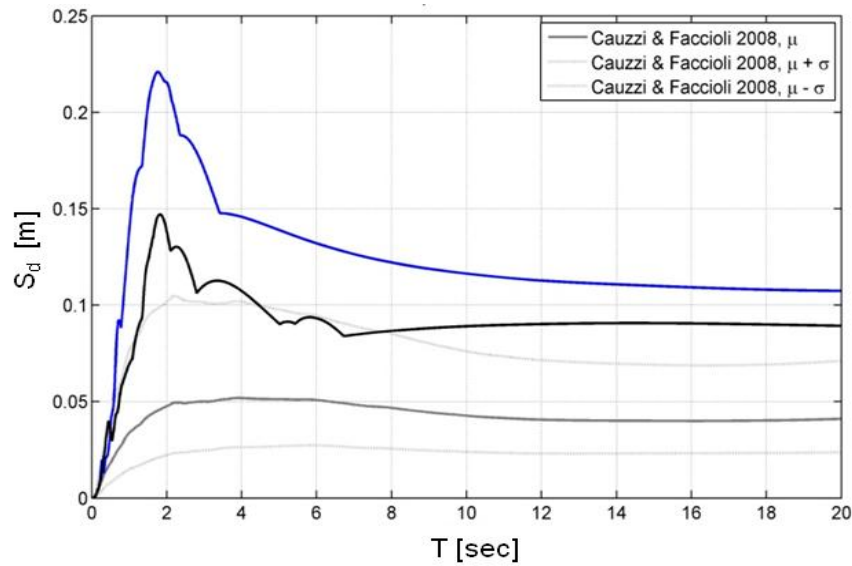


Figure 28 Mirandola station (MRN): comparison of the horizontal (SN, EW) acceleration response spectra with the Bindi et al. (2011) GMPE for ground category C.

Displacement response spectra computed using the Mirandola station recordings have been compared with the spectra predicted by the GMPE developed by Cauzzi and Faccioli (2008) for the horizontal component and for ground category C (Figure 29). In this case the GMPE severely underestimates the spectra calculated from the records for all the periods.



**Figure 29** Mirandola station (MRN): comparison of the horizontal (SN, EW) displacement response spectra with the Cauzzi and Faccioli (2008) GMPE for ground category C.

Figure 30 and Figure 31 illustrate the same type of comparison for the recordings of the Zola Pedrosa Piana station (ZPP). This seismic station has been chosen since it is the second one closer to the epicenter. ZPP station is approximately 40.7 km far from the epicenter. From Figure 30 it may be noticed that at this station the acceleration spectra predicted by the GMPE of Bindi et al. (2011) tend to overestimate the spectra from the recordings up to a period of about 0.7 sec. For larger periods the EW component is well predicted whereas the SN component is underestimated.

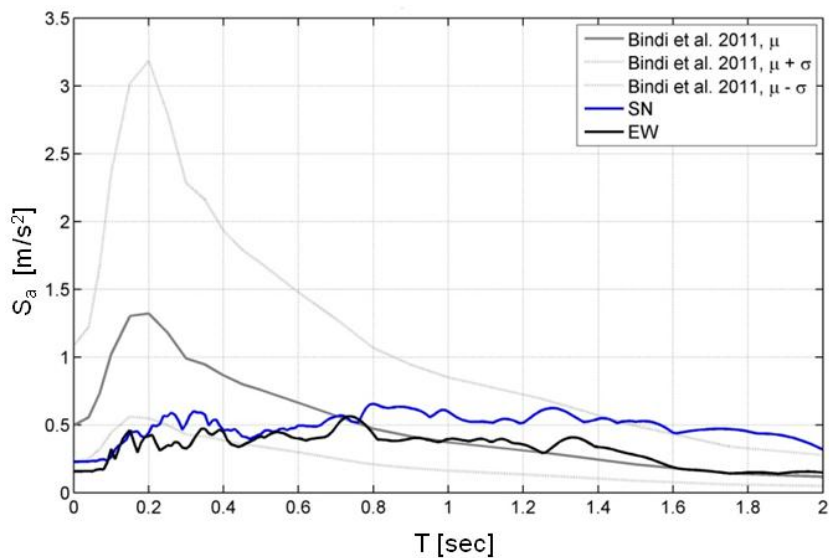


**Figure 30** Zola Pedrosa Piana station (ZPP): comparison of the horizontal (SN, EW) acceleration response spectra with the Bindi et al. (2011) GMPE for ground category C.

Displacement response spectra computed using the Zola Pedrosa Piana station recordings have been compared with the spectra predicted by the GMPE developed by Cauzzi and Faccioli (2008) for the horizontal component (Figure 31). As for the Mirandola station, the GMPE tends to severely underestimate the spectra calculated from the records at all the periods.

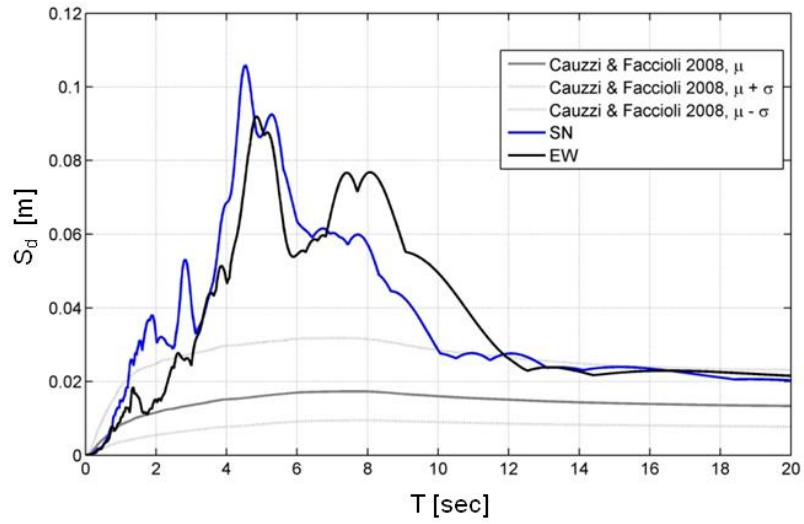


Figure 31 Zola Pedrosa Piana station (ZPP): comparison of the horizontal (SN, EW) displacement response spectra with the Cauzzi and Faccioli (2008) GMPE for ground category C.

## 1.7. Preliminary ground response analysis at Mirandola

The availability of field test results at a few sites inside the Municipality of Mirandola allowed a preliminary assessment of ground response where the closest station to the epicenter is located. Figure 32 shows the sites where *in situ* tests were performed in the area of Mirandola prior to the earthquake of May 2012. The corresponding data can be retrieved from the webGIS portal of the Emilia-Romagna Region (<https://territorio.regione.emilia-romagna.it/cartografia/cartografia-sgss>). Figure 33 shows an image of the town of Mirandola containing the site locations where MASW tests have been performed during a 2011 geophysical campaign (184090J001, 184090J002, 184090J003, 184090J004 and 184090J005). This data has been used to construct a geotechnical model of the subsoil at Mirandola which was successively adopted to perform ground response analyses. The figure also shows the location of Mirandola strong-motion seismic station (MRN).

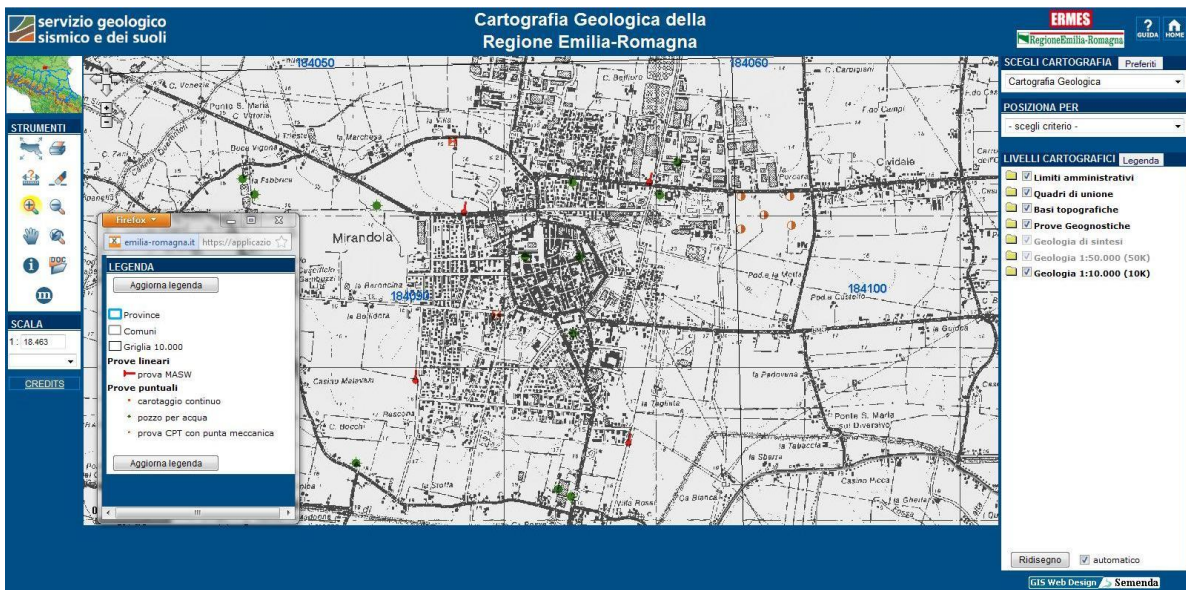


Figure 32 Map of the sites where *field* tests were performed in the territory of Mirandola prior to the earthquake of May 2012 (from <https://territorio.regione.emilia-romagna.it/cartografia/cartografia-sgss>).

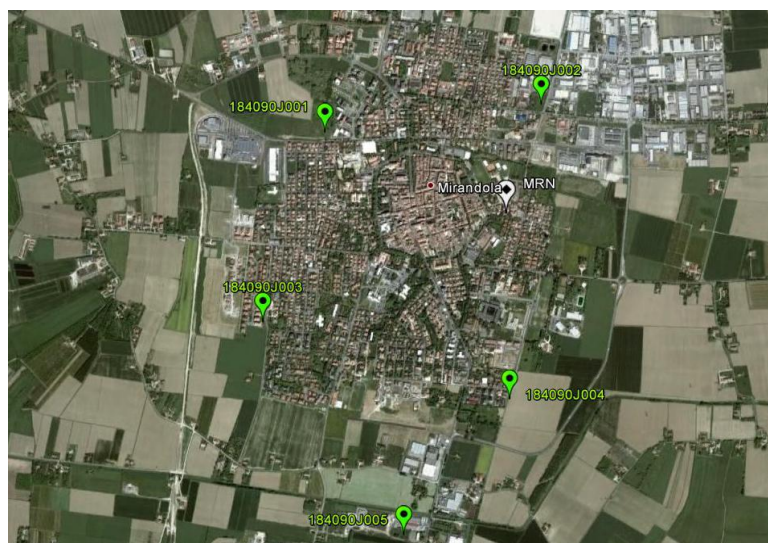
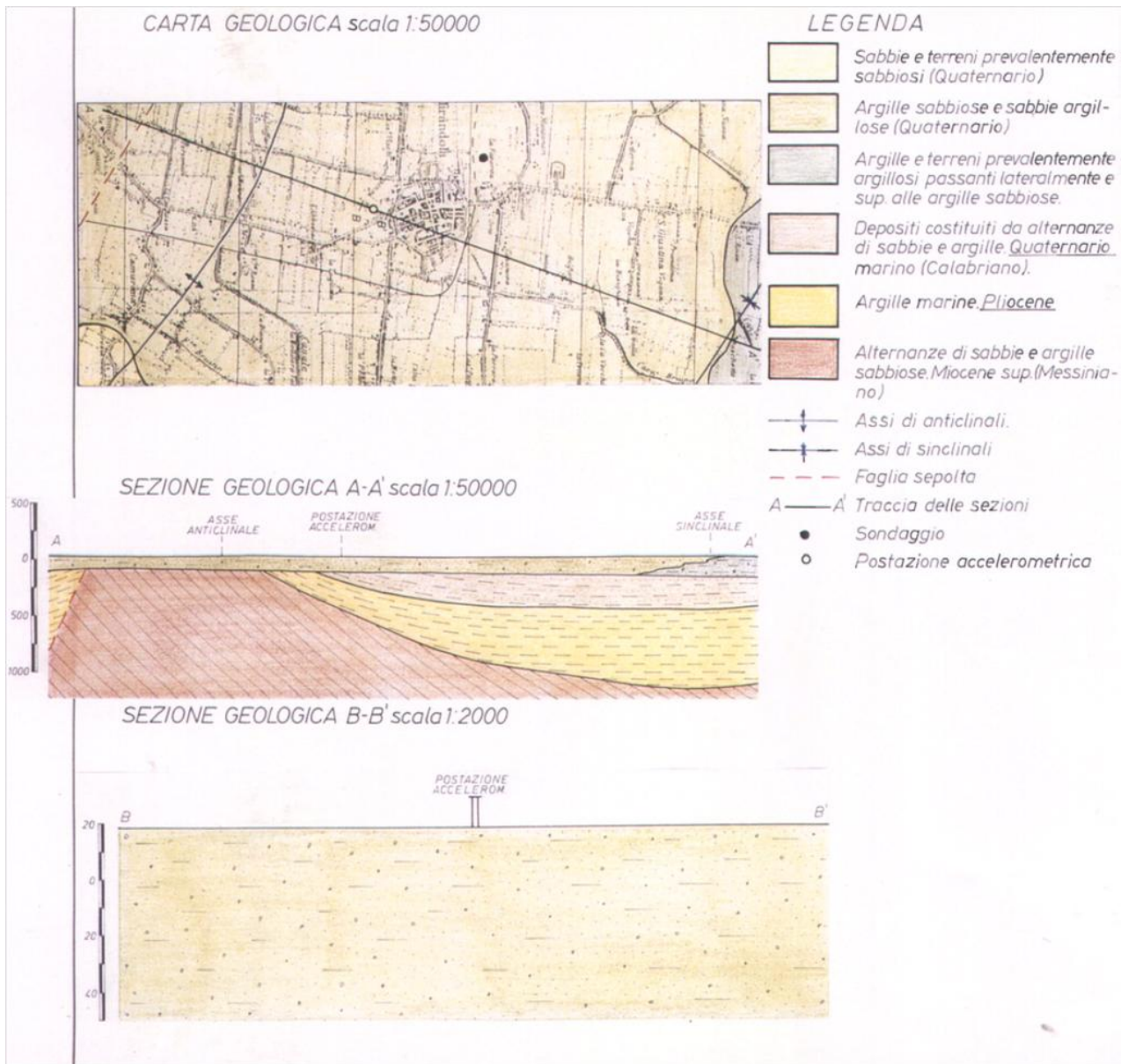


Figure 33 The urban center of Mirandola along with the locations where MASW geophysical tests were performed during a 2011 geophysical campaign (green markers). The data acquired during these tests were used to perform ground response analysis. The figure shows also the location of Mirandola strong-motion seismic station (MRN).

Geological information about the soil deposits of the site where MRN recording station is located was retrieved at the portal <http://itaca.mi.ingv.it/ItacaNet/>. Figure 34 shows the data available for MRN.



**Figure 34** Geological information available for the site where Mirandola recording station (MRN) is located (from <http://itaca.mi.ingv.it/ItacaNet/>).

1D linear equivalent, fully stochastic site response analysis has been performed at Mirandola using the methodology described in Rota et al. (2011) which takes into account the uncertainties associated with the geotechnical model parameters. The stochastic analysis has been carried out using Monte Carlo simulations associated with the Latin Hypercube sampling technique.

Randomly-generated geotechnical parameters varying within properly-defined probability distributions were assumed to calculate the seismic response of 100 deterministic realizations of the geotechnical model. The uncertainty adopted for the values of  $V_S$  is shown in Figure 35 where the red line denotes the mean of 100  $V_S$  profiles with layers of varying thickness. For the definition of the depth of the bedrock and of its stiffness, data available at the website of the Emilia-Romagna Region (<http://ambiente.regione.emilia-romagna.it>) were used.

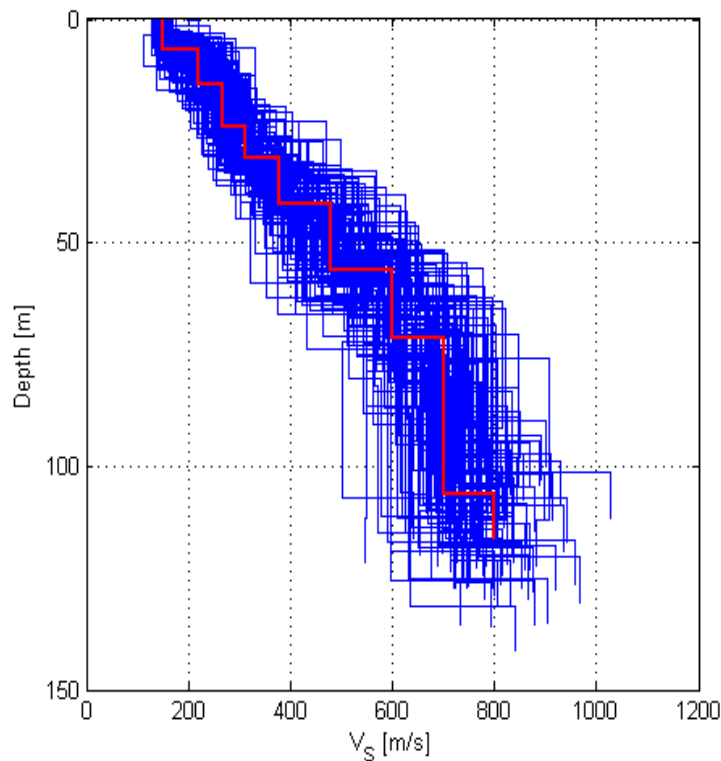


**Figure 35** 100 random  $V_s$  profiles generated using the Latin Hypercube sampling technique. The red line represents the mean profile.

The variability of seismic input was taken into account by considering an appropriate set of seismo- and spectrum-compatible natural records. Specifically, a set of 7 accelerograms recorded from real earthquakes were downloaded for the area under investigation from the website <http://www.eucentre.it/seismhome.html> (Rota et al., 2012). The signals were recorded on outcropping rock conditions and they are spectrum-compatible, in the mean, to the Italian code-based spectrum referred to the return period of 475 years. In fact, although it is still premature to make definitive conclusions, there is numerous seismological evidence that seems to suggest that the Emilia May 20, 2012 earthquake may correspond to this return period.

Figure 36 shows the mean acceleration response spectrum and plus/minus one standard deviation that has been calculated using linear-equivalent, fully-stochastic, 1D ground response analyses. This spectrum is compared to the response spectra calculated from the SN, EW recordings of the MRN station for the May 20, 2012 event. The figure also shows the spectrum for soil A computed according to the prescriptions of the Italian building code (NTC, 2008). The mean PGA computed from ground response analysis turned out to be equal to 0.269 g, which is in excellent agreement with the recorded PGA (see Table 2).

However the peaks of the MRN spectra are underestimated by the mean spectrum. A better agreement seems to be obtained by considering the mean spectrum plus one standard deviation only for the band with lower periods up to about 1 sec. For periods greater than 1 sec, the spectral accelerations of the MRN recordings, especially the SN component, exceed those of the computed spectra. Two possible explanations for this difference may be near-fault effects as the Mirandola station, which lies only 13 km away from the epicenter and in also the fact that the May 20, 2012 earthquake was a shallow event (with a focal depth of about 6.3 km). Further investigation is however needed to substantiate these preliminary statements.

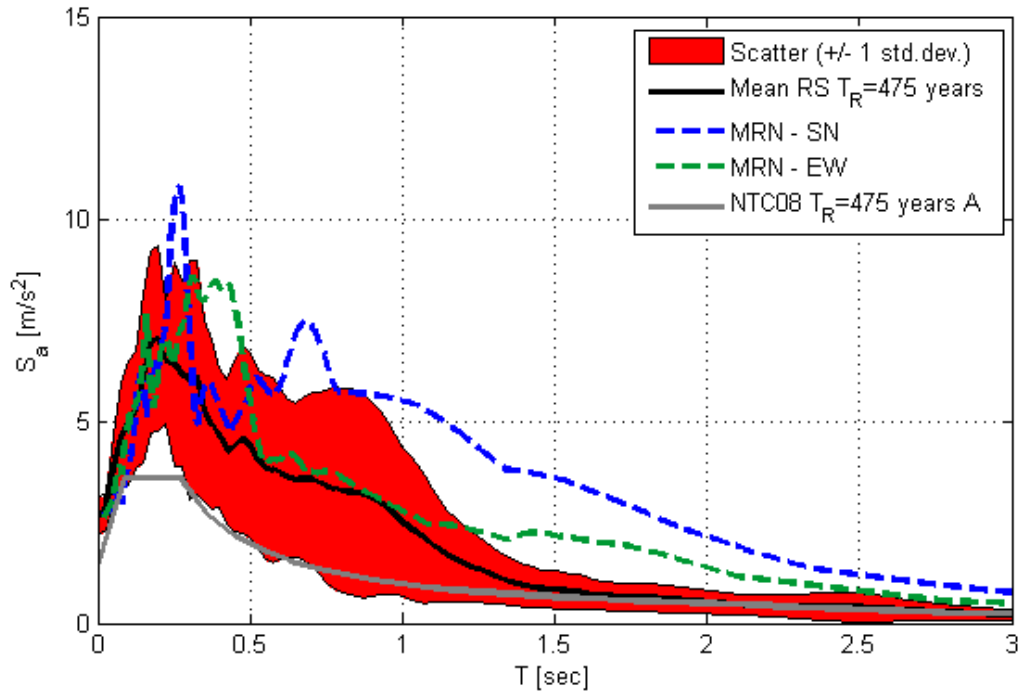
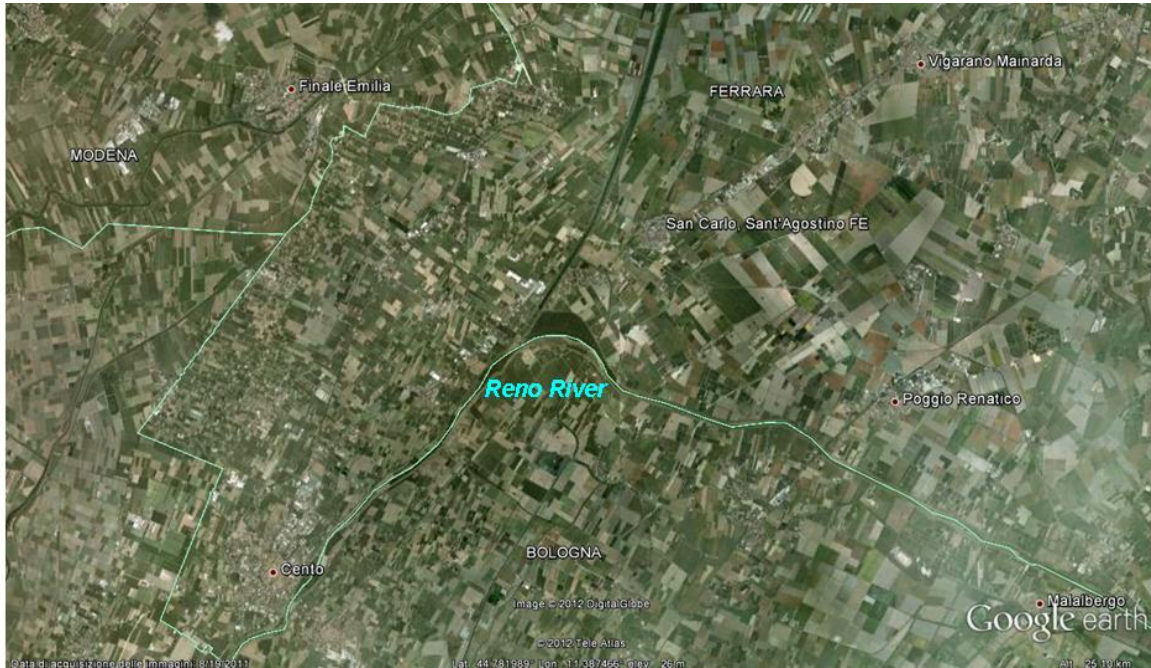


Figure 36 Mean acceleration response spectrum with the associated scatter computed using the  $V_s$ -profiles of Figure 35. The seismic input required to perform ground response analysis was constituted by 7 real records compatible to the Italian code-based spectrum referred to 475-year return period. The computed spectra are compared to the SN and EW spectra calculated from the recordings of the MRN station. Also shown is the spectrum for soil type A computed according to the prescriptions of the Italian building code (NTC, 2008).



The Southern part of the Ferrara Province is crossed by the Reno River, the most important river of the Emilia-Romagna Region after the Po River. Figure 38 shows the Reno River in the area where it marks the border between the provinces of Ferrara and Bologna. The Reno River is an ancient river whose course varied over the plain throughout the centuries. Its waters often stagnated in a wide valley area between Bologna and Ferrara. Some interesting notes on the history of the Reno River can be found in Barbieri (2003) from which Figure 39 has been taken.



**Figure 38** The Reno River passing over the Provinces of Ferrara and Bologna.

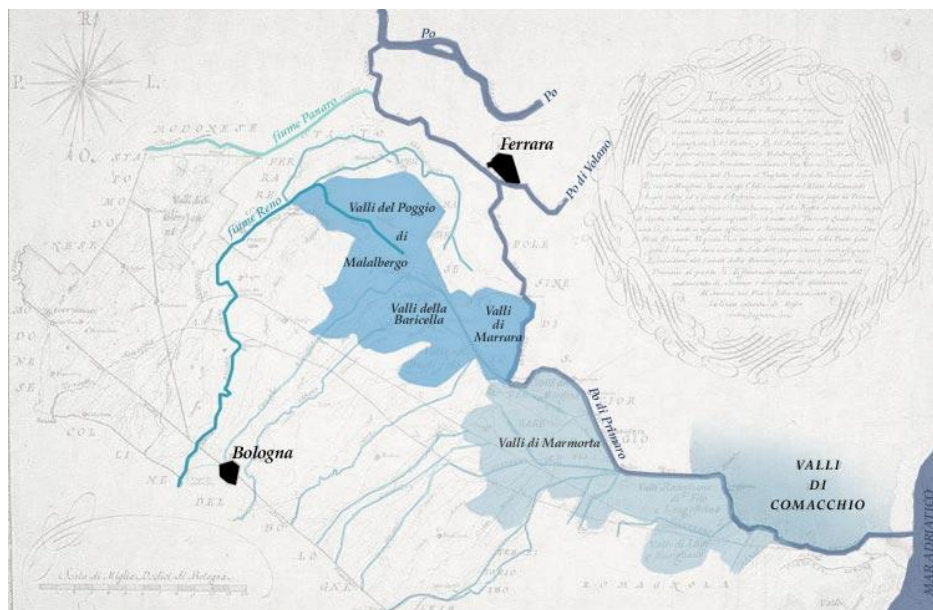


**Figure 39** The history of the Reno River: topography of Bologna plain in 1763 (Barbieri, 2003).

## 2.2. Historical cases of liquefaction

Although the most spectacular effects of soil liquefaction occur typically during strong earthquakes ( $M_w > 7.0$ ) at susceptible sites close to the epicenter (e.g. M7.3 Charleston, USA 1886; M9.2 Alaska, USA 1964; M7.6 Niigata, Japan 1964; M7.6 Izmit, Turkey 1999), there have been cases where moderately strong earthquakes (e.g. M6.8 Kobe, Japan 1995; M6.3 Christchurch, New Zealand 2011) have produced widespread liquefaction. The May 20, 2012 M5.9 and May 29, 2012 M5.65 shocks in Emilia Romagna, Italy are examples of moderate earthquakes yielding extensive liquefaction-related phenomena.

The database of historical liquefaction in Italy (Galli, 2000) demonstrates the existence of a relatively large number of weak to moderate earthquakes ( $M_s > 4.2$ ) producing liquefaction. The Italian territory is characterized by high seismicity along the Apennine chain and Eastern Alps. Broad liquefaction-prone-areas exist along the Adriatic, and Tyrrhenian coasts, the Po River alluvial plain. Severe historical earthquakes occurred in Calabria, Eastern Sicily and Campania. The long history of civilization of Italy and the availability of historical written sources also provides data with respect to the occurrence of liquefaction in ancient times. Galli (2000) compiled a catalogue of earthquakes where he recognized 59 liquefaction features resulting from earthquakes with  $M_s < 5.9$ . The compiled database contains indication of liquefaction related to earthquakes occurred in Italy from 1117 AD to 1990 (Figure 40). The MCS macroseismic intensity ranged from 5.5 to 11, whereas the magnitude ranged from 4.2 to 7.5 for  $M_s$  and from 4.83 to 7.46 for  $M_e$  (magnitude derived from intensity data).

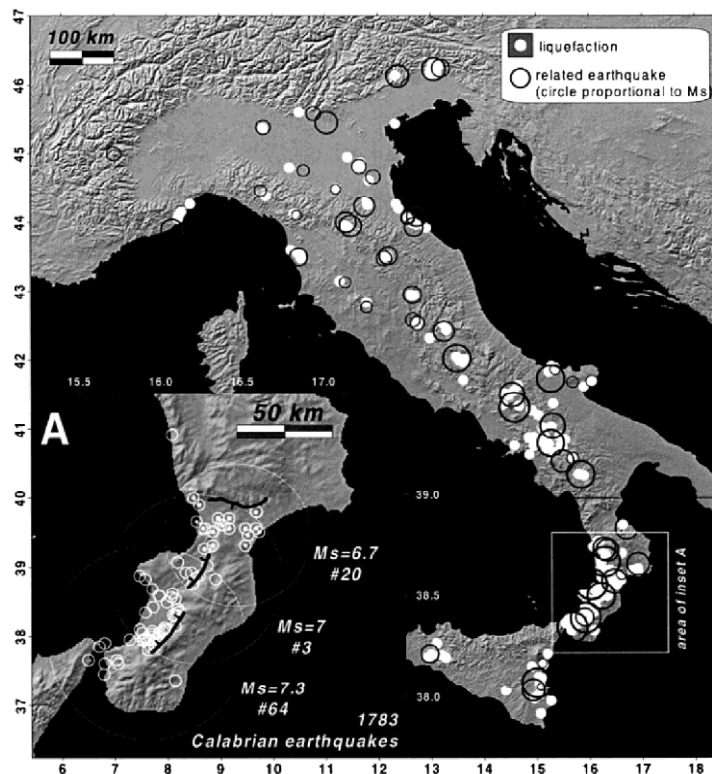


**Figure 40** Map with the distribution of liquefaction cases documented in Italy over the last one-thousand years (Galli, 2000).

Table 3 is an excerpt of the original database and it shows that liquefaction occurred in the Ferrara area during the 1570 AD earthquake that had an estimated magnitude of 5.3. The liquefaction affected areas are shown in Figure 41 and Figure 42. Figure 42 shows the location of sites with evidence of liquefaction associated to the earthquake occurred in Ferrara on 17/11/1570. On the same figure are overlapped the sites with evidence of liquefaction occurred during the recent earthquakes of May 20 and May 29, 2012. Figure 43 shows the sites with evidence of liquefaction after the 2012 earthquakes in the area of Sant'Agostino, San Carlo and Mirabello.

**Table 3** An excerpt of the catalogue of liquefaction phenomena occurred in Italy since 1117 AD (Galli, 2000).

Epicentral parameters of the seismic events							Sites with indication of liquefaction						
Ref.	Date	Latitude	Longitude	$I_0$	$M_c$	$M_s$	Area	Site <sup>a</sup>	Latitude	Longitude	$d$ (km)	$I_s$	Type
1	1117.01.03	45.330	11.200	9.5	6.56	6.4	Verona area	Venezia	45 26	12 20	89	7.0	A2
2	1505.01.03	44.480	11.250	7.0	5.30	5	Bologna	Zola Predosa	44 30	11 13	3	7.0	A1 A3-5
3	1542.06.13	44.000	11.380	9.0	5.85	6.2	Scarperia	Borgo S. Lorenzo	43 57	11 23	6	8.0	A2
4	1542.12.10	37.230	14.920	9.5		6.4	Sortino	Siracusa and neighbour [2]	37 04	15 16	36	8.0	A1-2
5	1545.06.09	44.498	9.844	7.5	5.00	5.2	Borgo V. Taro	Pontremoli [1]	44 23	9 53	13	6.0	A1-2
6	1561.08.19	40.520	15.480	9.5	6.45	6.4	Vallo di Diano	Muro Lucano	40 45	15 29	26	9.0	A1 A3 D
7	1570.11.17	44.820	11.630	7.5	5.30	5.5	Ferrara	Boara	44 52 00	11 41 00	7	7.5	A3-5
8	1570.11.17	44.820	11.630	7.5	5.30	5.5	Ferrara	Ferrara (P.te S.Paolo, S.Pietro)	44 49 40	11 37 00	1	8.0	A1-5 B C D
9	1570.11.17	44.820	11.630	7.5	5.30	5.5	Ferrara	Ficarolo	44 57	11 26	21	7.0	A1 A4-5
10	1570.11.17	44.820	11.630	7.5	5.30	5.5	Ferrara	Giara del Po	44 48 30	11 41 30	5	7.0	A1
11	1570.11.17	44.820	11.630	7.5	5.30	5.5	Ferrara	La Punta	44 49 00	11 40 00	3	7.5	A1 A4
12	1570.11.17	44.820	11.630	7.5	5.30	5.5	Ferrara	Localita' indefinite	-	-	-	-	A1 A3 A4
13	1570.11.17	44.820	11.630	7.5	5.30	5.5	Ferrara	Polesino di S.Giovanni Battista	44 50 30	11 38 20	3	8.0	A1 A4 B
14	1570.11.17	44.820	11.630	7.5	5.30	5.5	Ferrara	Polesino di San Giorgio	44 49 20	11 37 30	0	8.0	A1 A4 B
15	1570.11.17	44.820	11.630	7.5	5.30	5.5	Ferrara	Torre della Fossa	44 47 40	11 37 00	3	7.5	A1 A4 B
16	1624.03.18	44.650	11.850	7.5	5.30	5.5	Argenta	Argenta	44 37	11 50	4	9.0	A1-4 C D
17	1627.07.30	41.730	15.350	10.0	6.78	7	Capitanata	Foci del Fortore	41 55	15 17	21	8.5	A1 A4-5 D
18	1627.07.30	41.730	15.350	10.0	6.78	7	Capitanata	Lesina	41 52	15 21	15	10.0	C
19	1627.07.30	41.730	15.350	10.0	6.78	7	Capitanata	Ripalta	41 51	15 17	14	10.0	C
20	1627.07.30	41.730	15.350	10.0	6.78	7	Capitanata	Localita' indefinita	-	-	-	-	A4
21	1627.07.30	41.730	15.350	10.0	6.78	7	Capitanata	Serra-S.Agata (Valle d. Fortore)	41 50	15 14	15	9.5	A1 A4
22	1627.07.30	41.730	15.350	10.0	6.78	7	Capitanata	Troja	41 22	15 19	40	7.5	A5

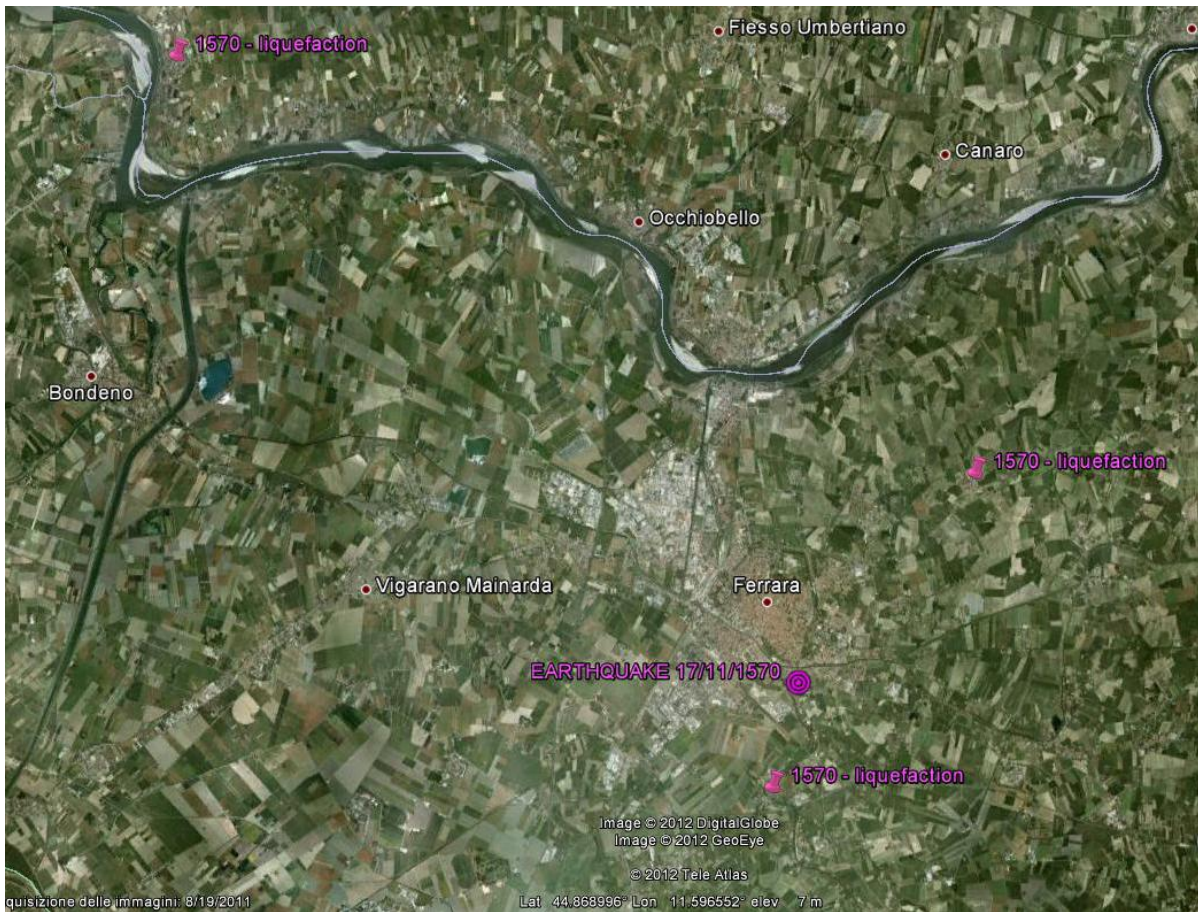


**Figure 41** Location of some historical sites with evidence of liquefaction identified by Galli (2000) during the earthquake of Ferrara on 17/11/1570.

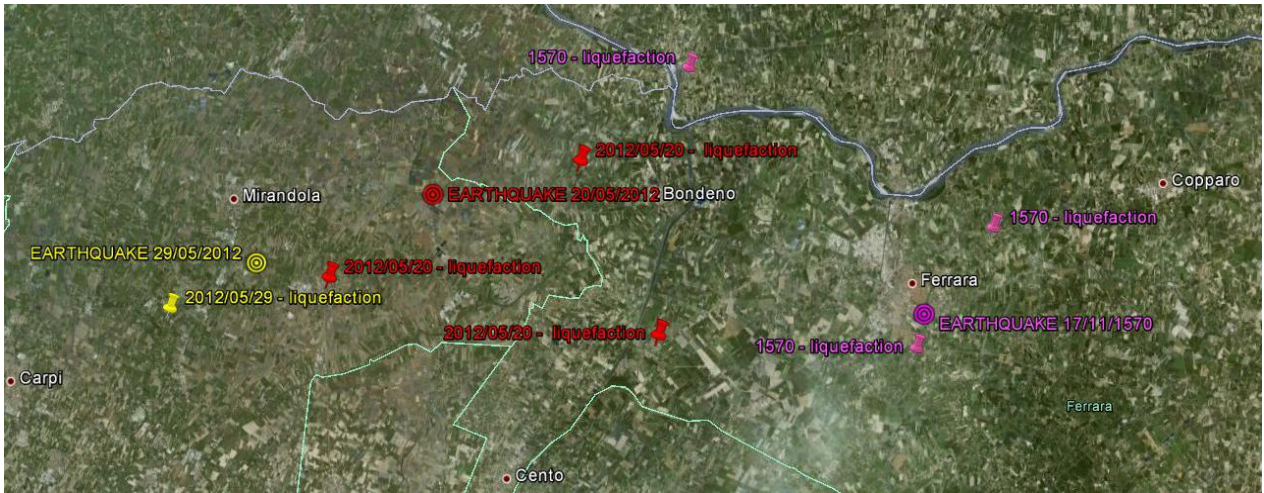


Figure 42 Location of some historical sites with evidence of liquefaction identified by Galli (2000) during the earthquake of Ferrara on 17/11/1570. On the same figure are overlapped sites with evidence of liquefaction occurred during the recent earthquakes of May 20 and May 29, 2012.

**Fenomeni di liquefazione osservati**  
(puntuali e lineari)

- dati STB RENO
- dati STB AFFLUENTI PO
- dati GEOPROCV

**Paesaggio geologico**

- argini - fiumi appenninici
- piana alluvionale - fiumi appenninici
- meandri fluviali - fiume Po
- paleocanali

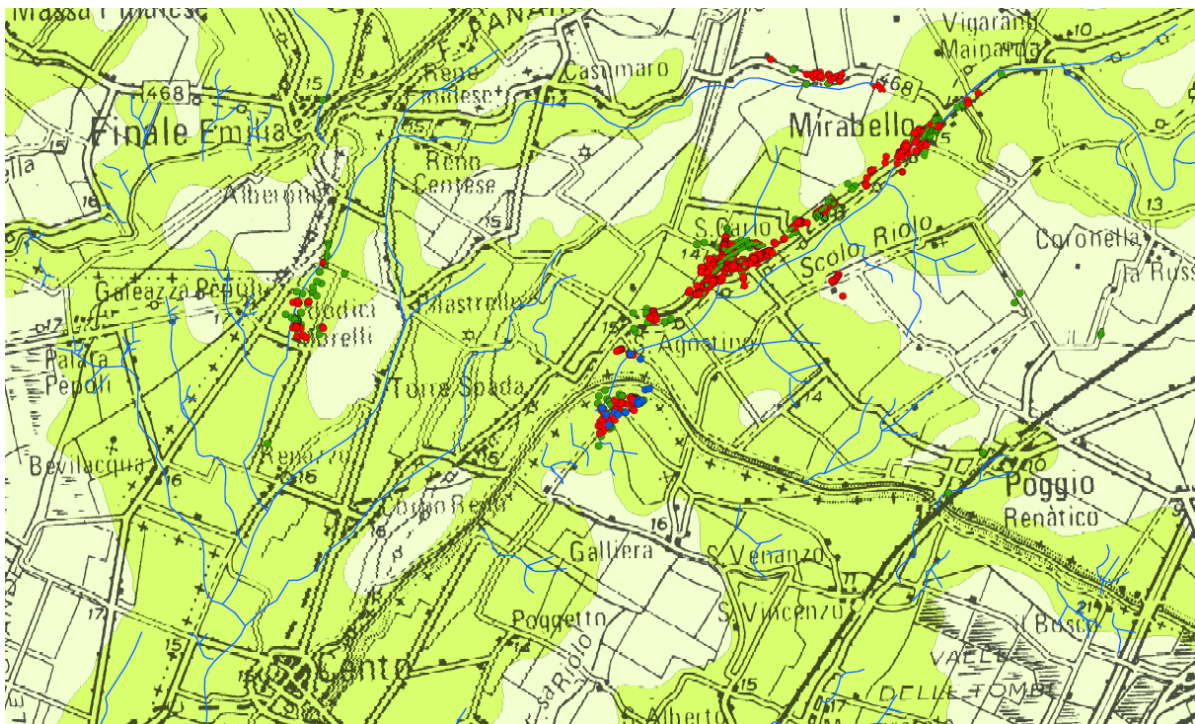


Figure 43 Evidence of liquefaction after the earthquakes occurred on May 20 and May 29, 2012 (from <http://geo.regione.emilia-romagna.it>).

### 2.3. Effects of liquefaction at San Carlo

The village of San Carlo under the Municipality of Sant'Agostino (near Ferrara) was affected by significant phenomena of liquefaction following the M5.9 event of May 20, 2012. San Carlo is located about 17 km from the epicenter. Figure 45 through Figure 54 show the sites that were investigated in San Carlo by the geo-reconnaissance team of EUCENTRE about a week after the earthquake of May 20, 2012. Field measurements were made to estimate the extension of the observed liquefaction phenomenon.

Sites 1 and 3 are located at the outskirts of San Carlo village whereas Site 2 is located inside the red area (characterized by collapsed and highly damaged buildings). Site 4 is located close to the graveyard. During the reconnaissance a series of non-invasive, seismic geophysical tests were carried out in order to estimate the shear-wave velocity profile at each of the four investigated sites. The purpose was to geotechnically characterize sites which showed evidence of liquefaction, as well as to provide an estimate for the depth to the bedrock. Details about the results of geophysical investigation are reported in the next Chapter.



**Figure 44** Location of the sites in San Carlo investigated by the EUCENTRE geo-reconnaissance team after the event of May, 20 2012.

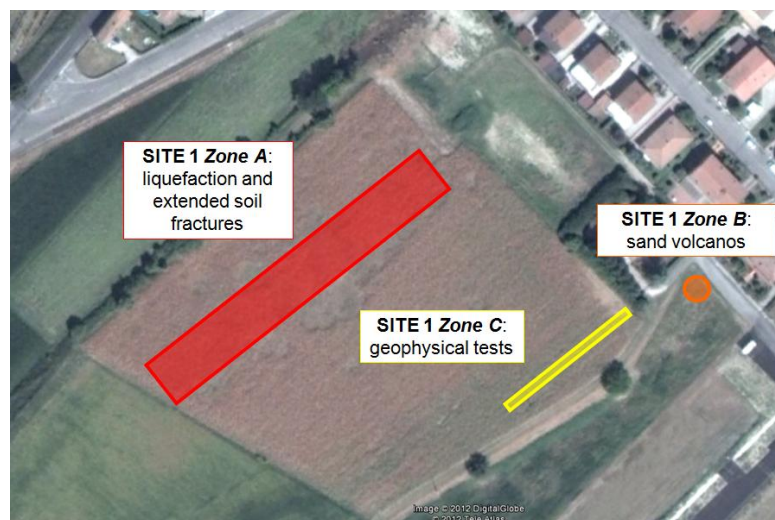


**Figure 45** Site 1 investigated by the EUCENTRE geo-reconnaissance team after the event of May, 20 2012.

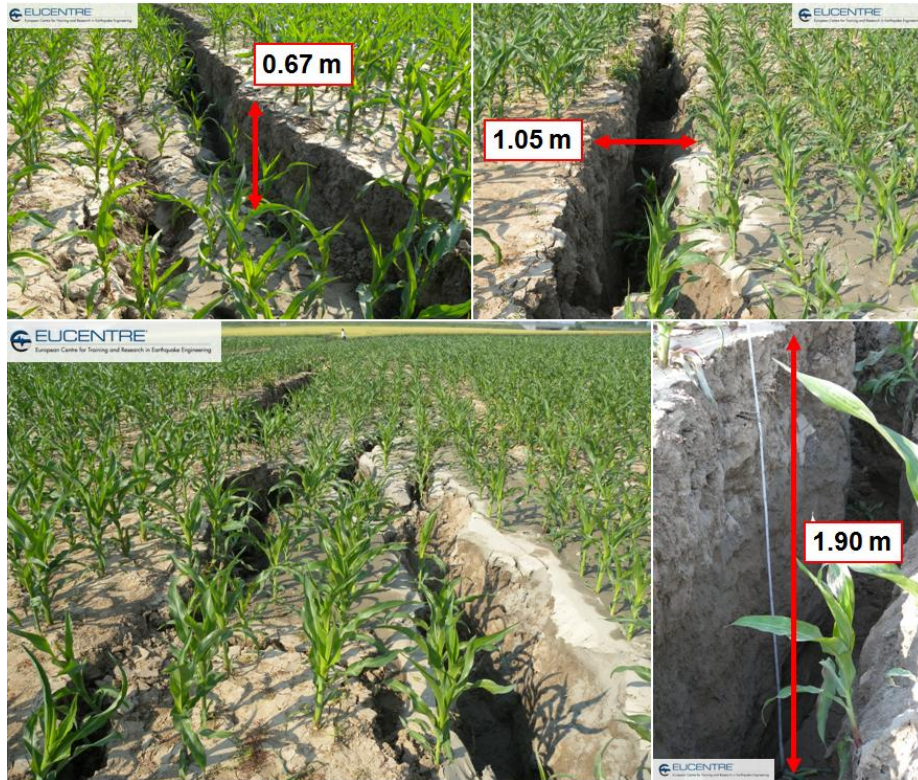


Figure 46 Site 1 investigated by the EUCENTRE geo-reconnaissance team after the event of May, 20 2012. Soil cracks and fractures in Zone A.



Figure 47 Site 1 investigated by the EUCENTRE geo-reconnaissance team after the event of May, 20 2012. Ejecta and sand volcanoes in Zone B and C.

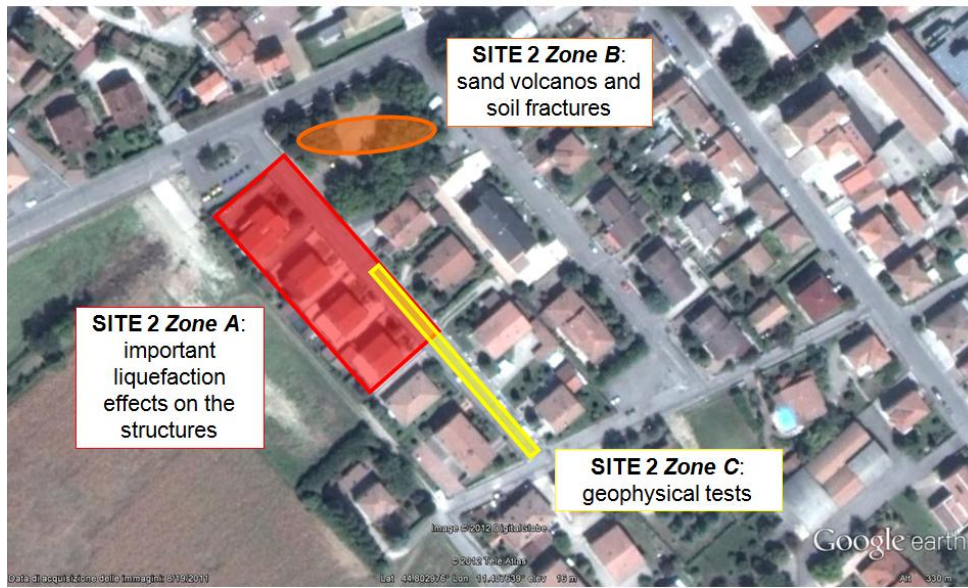


Figure 48 Site 2 investigated by the EUCENTRE geo-reconnaissance team after the event of May, 20 2012.



Figure 49 Site 2 investigated by the EUCENTRE geo-reconnaissance team after the event of May, 20 2012. Fissures with effects on structures and infrastructures in Zone A.



**Figure 50** Site 2 investigated by the EUCENTRE geo-reconnaissance team after the event of May, 20 2012. Soil cracks and fractures in Zone B.



**Figure 51** Site 3 investigated by the EUCENTRE geo-reconnaissance team after the event of May, 20 2012.



Figure 52 Site 3 investigated by the EUCENTRE geo-reconnaissance team after the event of May, 20 2012. Ejecta and sand volcanoes in Zone A.

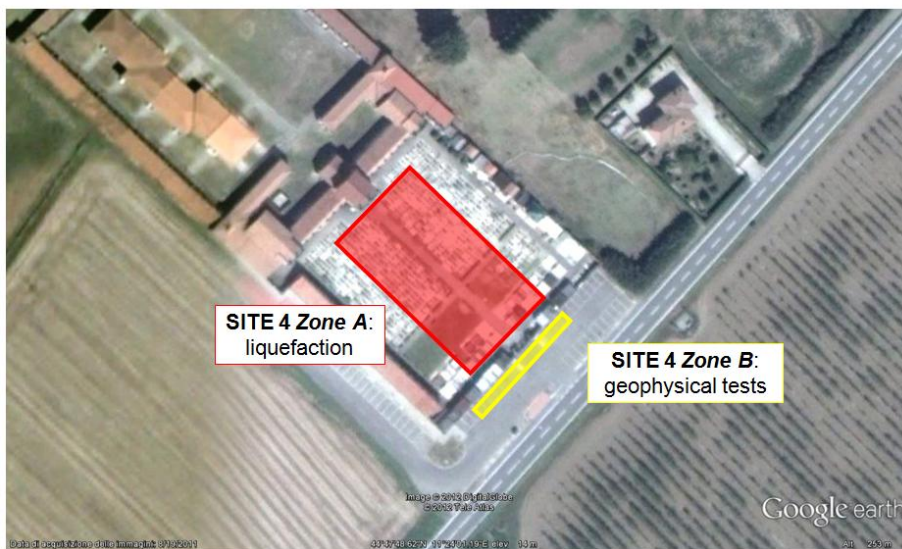


Figure 53 Site 4 investigated by the EUCENTRE geo-reconnaissance team after the event of May, 20 2012.



Figure 54 Site 4 investigated by the EUCENTRE geo-reconnaissance team after the event of May, 20 2012. Evidence of liquefaction in Zone A.

## 2.4. Available geotechnical information

Figure 55 shows the sites where boreholes were drilled for CPT and SPT testing in the area of San Carlo. The corresponding data was retrieved from the webGIS portal of the Emilia-Romagna Region (<https://territorio.regione.emilia-romagna.it/cartografia/cartografia-sgss>).

Five SPT tests performed prior to the earthquake of May 2012 (in the years 1986 and 1989), during geotechnical investigation campaigns in the South-West part of San Carlo (see Figure 56) were downloaded from the webGIS of the Emilia-Romagna Region in order to evaluate liquefaction potential. The next Section will show preliminary results obtained from the interpretation of these data to assess liquefaction susceptibility. Figure 56 shows also the location of these sites and of areas S1, S2 and S3 investigated by the EUCENTRE geo-reconnaissance team.

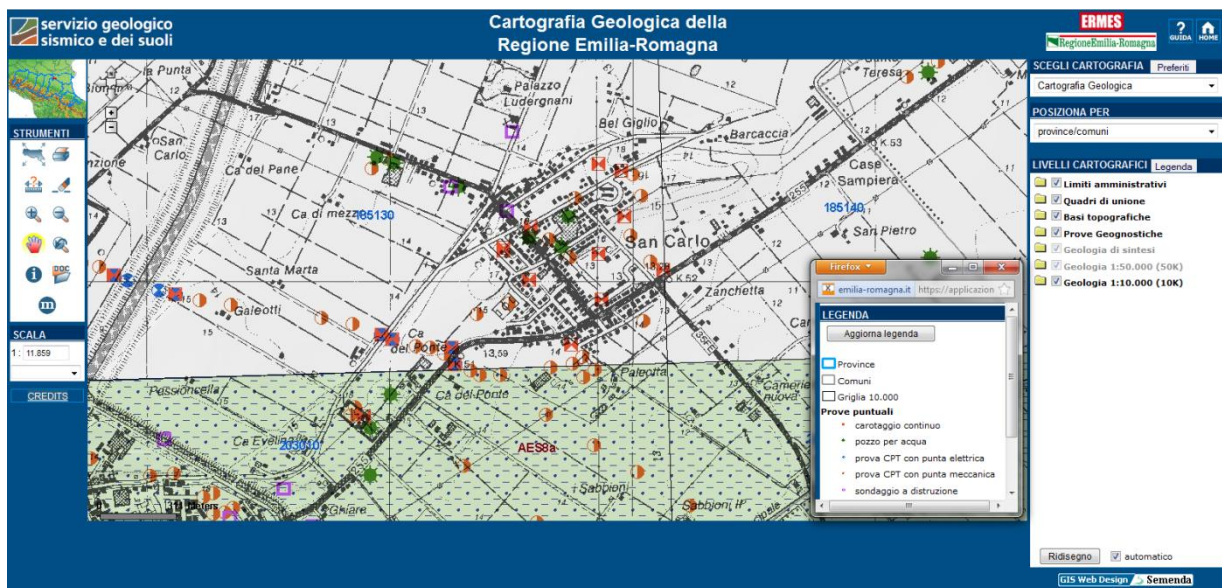


Figure 55 Map of the sites where boreholes, CPT and SPT tests were performed in the area of San Carlo prior to the earthquake of May 2012 (from <https://territorio.regione.emilia-romagna.it/cartografia/cartografia-sgss>).



Figure 56 Location of the sites where SPT tests were performed prior to the earthquake of May 2012 (in the years 1986 and 1989). Also plotted are the areas investigated by the EUCENTRE geo-reconnaissance team, specifically Sites 1, 2 and 3.

Some analyzed borehole logs are shown in the following figures (Figure 57, Figure 58 and Figure 59). They show that the water table was superficial and located 3m below the ground level. At the same time the documents reveal high spatial variability of soil characteristics, especially in the upper layers. In the first 8 to 10 m below the ground level the lithotypes range from clayey silt (Figure 57) to fine sand (Figure 58 and Figure 59). The lateral heterogeneity of soil formations is confirmed by the results of CPT tests and is consistent with the observations made during reconnaissance on whether or not liquefaction has occurred at closely-spacing sites.

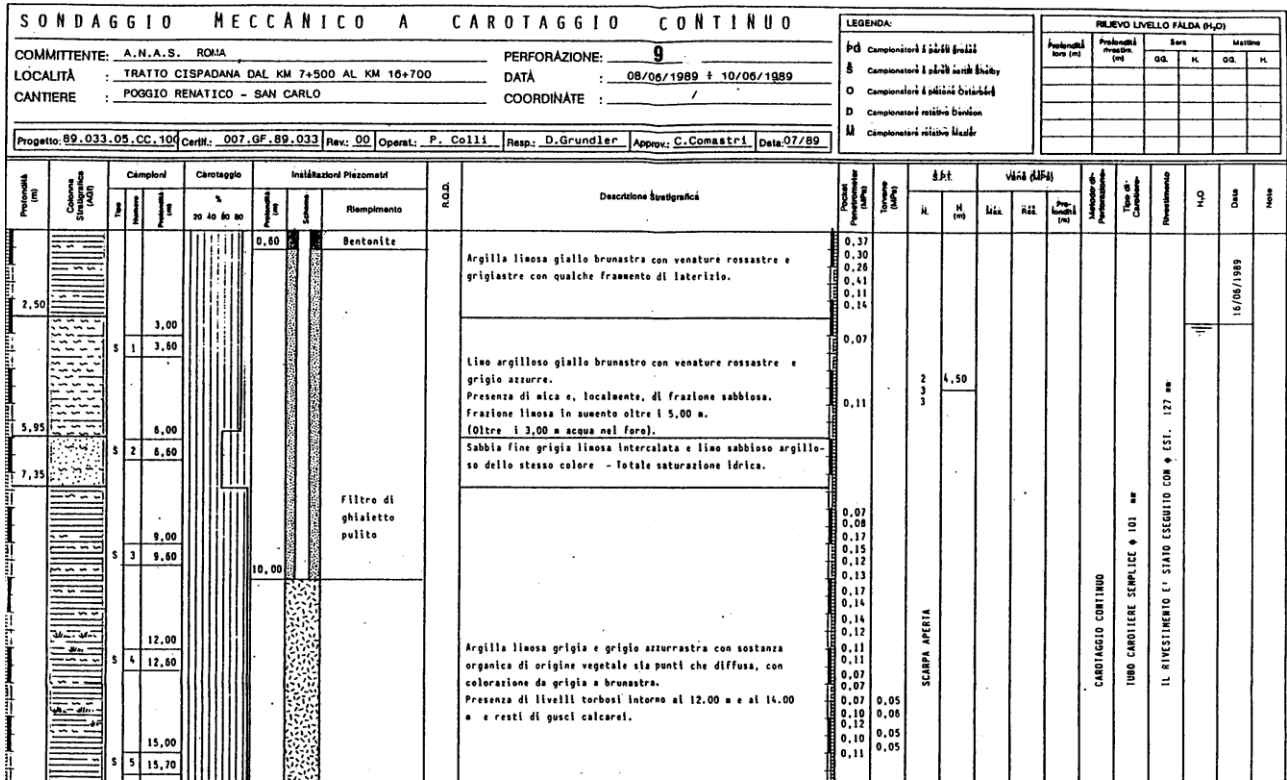


Figure 57 Borehole log SPT002\_185130P427B from the geotechnical investigation campaign performed at San Carlo in 1989.

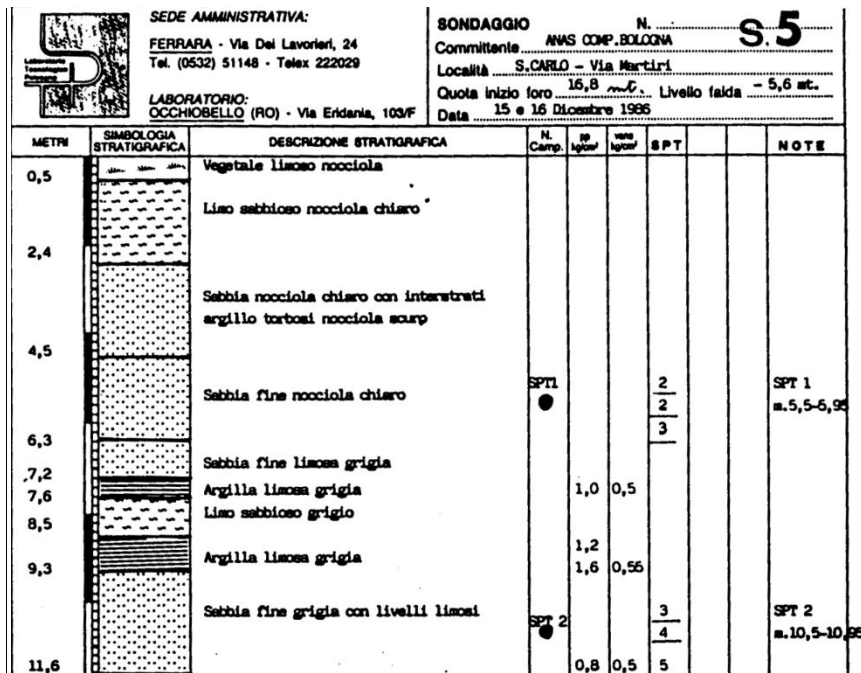


Figure 58 Borehole log SPT001\_185130P427A from the geotechnical investigation campaign performed at San Carlo in 1986.

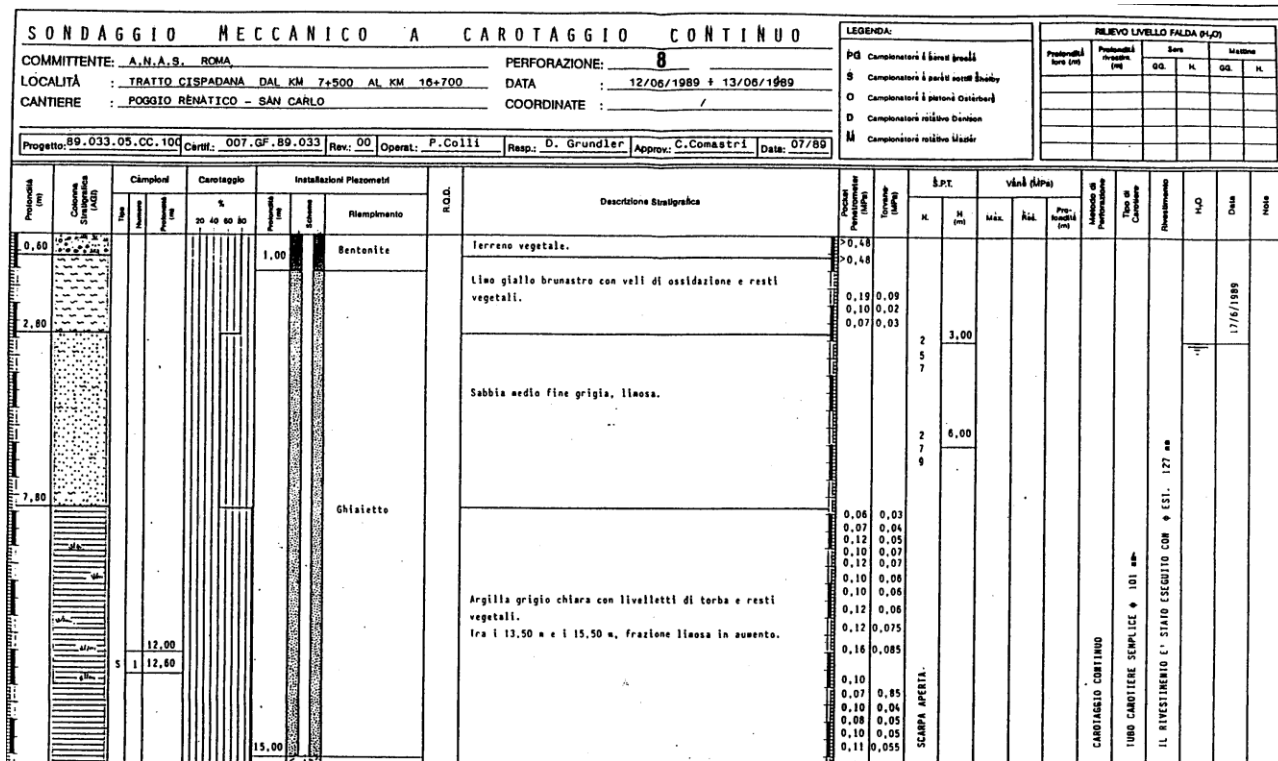


Figure 59 Borehole log SPT003\_185130P432 from the geotechnical investigation campaign performed at San Carlo in 1989.

The lateral heterogeneity observed in San Carlo is characteristic of fluvial deposits. The fluvial deposits consist of laterally discontinuous sand lenses with varying amounts of conglomerate and poorly stratified fine grained materials. The most important mechanisms causing the fluvial soil structure involve: a) the erosion/depositional processes characteristic of the river bed which are linked to the water's velocity distribution, and b) the geographical evolution of the river with time. In fact, as revealed from seismic data of fluvial deposits, depositional systems reveal distinct directional anisotropy (Deshpande et al., 1997), which can be used to infer the river's history. The characteristic sedimentary structure of river plains involves complex layering of high and low permeability layers with pronounced lateral heterogeneity, hence the soil units between boreholes may be poorly-correlated. In addition to the natural processes, to cause the lateral heterogeneity in San Carlo were also anthropic interventions such as the construction of river banks for flood prevention and artificial sandy fills (Martelli, 2012).

## 2.5. Preliminary assessment of liquefaction susceptibility

The availability of borehole and SPT data at few sites inside the epicentral area, allows a preliminary assessment of the liquefaction potential using empirical correlations based on comparing the cyclic stress ratio (CSR) to the cyclic resistance ratio estimated from field-measured penetration resistance. Since the boreholes and SPT tests were performed in the years 1986 and 1989 and thus prior to the May, 2012 earthquake, this assessment will allow to verify the correctness of the predictions. The evaluation has been carried out using the data from San Carlo area described in the previous section.

The field tests, upon which the method of empirical correlations is based, have now reached a sufficient level of maturity as to represent a reliable tool (Youd et al., 2001). For sites in Italy, they include the standard penetration test (SPT), the cone penetration test (CPT) and direct measurement of in-situ shear wave velocity  $V_s$ . SPT and CPT are generally preferred due to the existence of large databases and experience although the oldest, and still most widely used method, is that based on SPT results. Despite the extensive experience matured in this field, the predictions of liquefaction susceptibility produced through the method of empirical correlations should be used with caution and considered valid only to first approximation.

The calculation of liquefaction susceptibility at San Carlo was carried out using both the deterministic approach, based on introducing a factor of safety ( $F_s$ ) and the probabilistic approach, for which the liquefaction potential is computed in terms of probability of liquefaction ( $P_L$ ). Three methods were used: method A based on the work by Youd et al. (2001), method B based on the approach proposed by Idriss and Boulanger (2008) and method C based on the recommendations by Seed (2010). The point-wise assessment of liquefaction susceptibility at different depths have been combined into a single parameter to yield the Liquefaction Potential Index LPI, proposed by Iwasaki et al. (1978), and the Liquefaction Severity Index LSI, introduced by Yilmaz (2004). Simplified approaches were also adopted for the evaluation of liquefaction-induced settlements: for method A, the methodology developed by Ishihara and Yoshimine (1992) has been adopted; the estimate of settlements in method B is based on the suggestions of Idriss and Boulanger (2008), who refer to the work of Yoshimine et al. (2006); the procedure of Cetin et al. (2009) has been implemented for method C.

Figure 60 shows the  $N_{SPT}$  profiles resulting from the available SPT data for the sites investigated in the 80's at San Carlo (Figure 56). The plot shows a significant variability of penetration resistance even over short lateral distances.

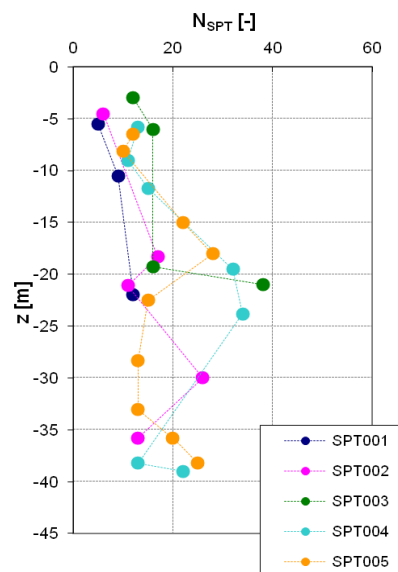
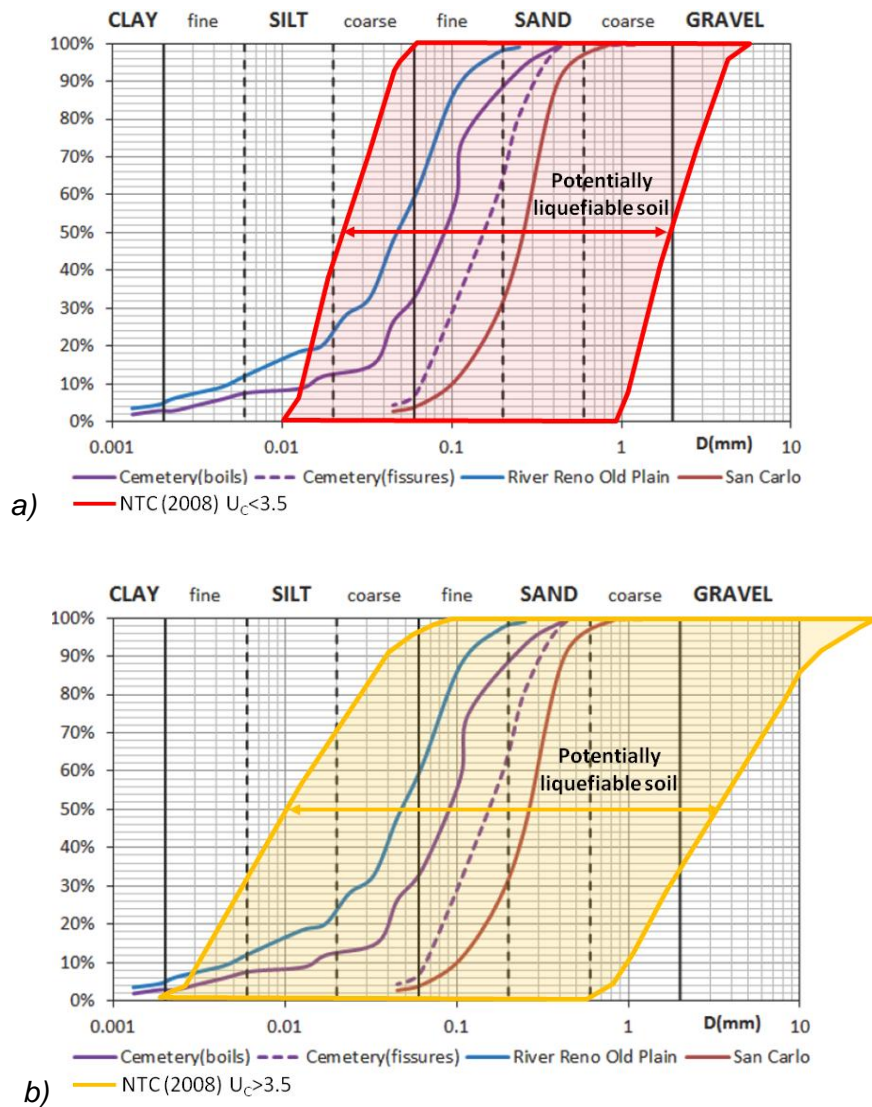


Figure 60  $N_{SPT}$  profiles from the available SPT data for the sites investigated in the 80's at San Carlo (Figure 56).

On the basis of the available SPT data, the soil deposit for the area under investigation is of *category D* for all five boreholes, based on the prescriptions of the current Italian building code (NTC, 2008). Useful information on grain sizes of sands sampled at the surface of San Carlo were retrieved from <http://ambiente.regione.emilia-romagna.it>. Figure 61 shows this data with overlapped the boundaries for potentially liquefiable soil as prescribed by the current Italian building code (NTC, 2008) in case of coefficients of uniformity  $U_C$  smaller than 3.5 (Figure 61a) and greater than 3.5 (Figure 61b).



**Figure 61** Grain sizes of sands sampled at the surface of San Carlo with overlapped the boundaries for potentially liquefiable soil as prescribed by the current Italian building code (NTC, 2008) in case of coefficients of uniformity  $U_C$  smaller than 3.5 (a) and greater than 3.5 (b).

The seismic input has been defined using the GMPE by Cauzzi and Faccioli (2008) whose predictions for the PGA are in good agreement with the recordings, as shown in the previous Section. The PGA computed with the GMPE by Cauzzi and Faccioli (2008) for soil category D at the site under investigation for the M5.9 earthquake of May 20, 2012 is 0.215 g. Table 4 shows the computed values of LPI, LSI and vertical settlements for each of the 5 boreholes shown in Figure 56.

**Table 4** Computed values of LPI, LSI and vertical settlements at each of the 5 boreholes shown in Figure 56.

Borehole #	LPI [-]			LSI [-]			Settlements [m]		
	Met. A	Met. B	Met. C	Met. A	Met. B	Met. C	Met. A	Met. B	Met. C
SPT001_185130P427A	2.6	2.3	3.0	0.4	0.9	1.5	0.138	0.102	0.080
SPT002_185130P427B	0.0	0.0	0.0	0.0	0.0	0.0	0.085	0.006	0.000
SPT003_185130P432	0.0	0.0	0.0	0.3	0.1	0.0	0.011	0.003	0.000
SPT004_185130P433	0.0	0.0	0.0	0.7	1.1	1.3	0.052	0.017	0.083
SPT005_185130P434	0.0	0.3	0.2	0.6	1.0	1.3	0.062	0.018	0.099

The results from Table 3 show that the parameter LPI is less than 6, therefore the liquefaction failure potential is estimated to be low. The LSI parameter is to a great extent less than 1.35, thus also according to Yilmaz (2004) the liquefaction failure potential is low. The vertical settlements shown in Table 3 were used to create a GIS georeferenced map for the area under investigation (Figure 62). A settlement of about 14 cm is predicted at the location of SPT001 borehole.

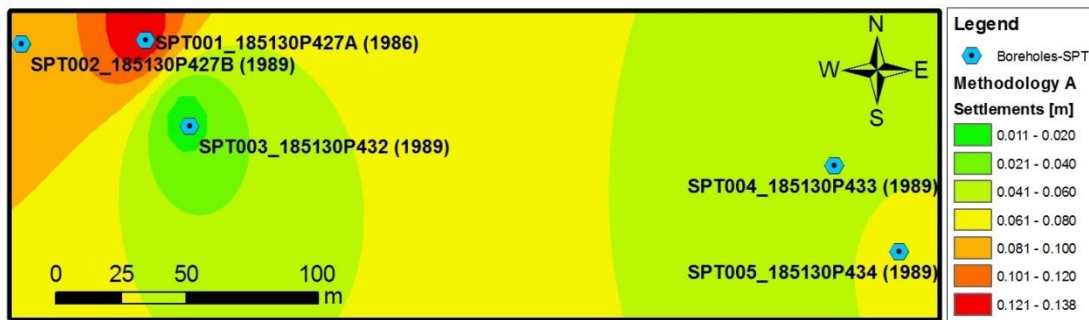


**Figure 62** Map of vertical settlements predicted at San Carlo using borehole data from geotechnical investigations conducted in the years 1986 and 1989.

It is now of interest to compare the results shown above with the observations made at the same sites during the reconnaissance survey immediately after the earthquake. This area of San Carlo village was not affected by significant liquefaction following the event of May 20, 2012. However the borehole SPT001 is located close to the Site 3 (Figure 56), that was characterized by the presence of sand boils, a clear evidence that soil liquefaction has occurred. The high variability of soil characteristics, particularly in the top 20 m, shown by the borehole log information, seems to well correlate the pattern of observed and predicted phenomena related to liquefaction. However further measurements and studies are needed to substantiate these preliminary considerations.

### 3. GEOPHYSICAL TESTING

#### 3.1. Objectives of geophysical testing

The main objective of the geophysical campaign carried out shortly after the seismic event of May, 20 2012 in the Po river valley was to assist the study of co-seismic effects, specifically liquefaction analysis. In this regard, it was felt important to characterize the shear-wave velocity profile,  $V_s(z)$ , at selected locations which showed evidence of liquefaction, as well as to provide an estimate for the water-table, and depth to bedrock. For this purpose, we performed MASW (Multi-channel Analysis of Surface Waves) and ReMi (Refraction Microtremor) measurements, which are fast, non-invasive methods for shear-wave velocity characterization. In addition we performed Nakamura H/V measurements, a fast and non-invasive method for determining the fundamental site period, which, combined with an average  $V_s$  value, can provide the approximate depth to bedrock.

The geophysical campaign discussed in the current report took place on May 29<sup>th</sup> 2012, at four selected sites in San Carlo, located in the province of Ferrara (Figure 63). The first location involved measurements inside a corn field, adjacent to an extensively fractured and liquefied area and the second location, which was a couple of hundred meters away from location 1, along via de Gasperi, a road in the declared “Zona Rossa” in the village of San Carlo (Figure 64). The third location was inside a soya field west of San Carlo village, which showed evidence of sand-boils and the fourth location was in front the parking lot of the local cemetery, which showed pronounced structural damage and liquefaction, located southwest of San Carlo village (Figure 65).

This preliminary report does not contain the theoretical principles behind MASW, ReMi and H/V testing. For information on these principles, the following literature is suggested, which is listed in the references: the SESAME Guidelines (2005) for H/V testing, Louie (2003) for ReMi, and Foti (2000) for MASW.



Figure 63 General view of San Carlo village with testing locations shown as stars.

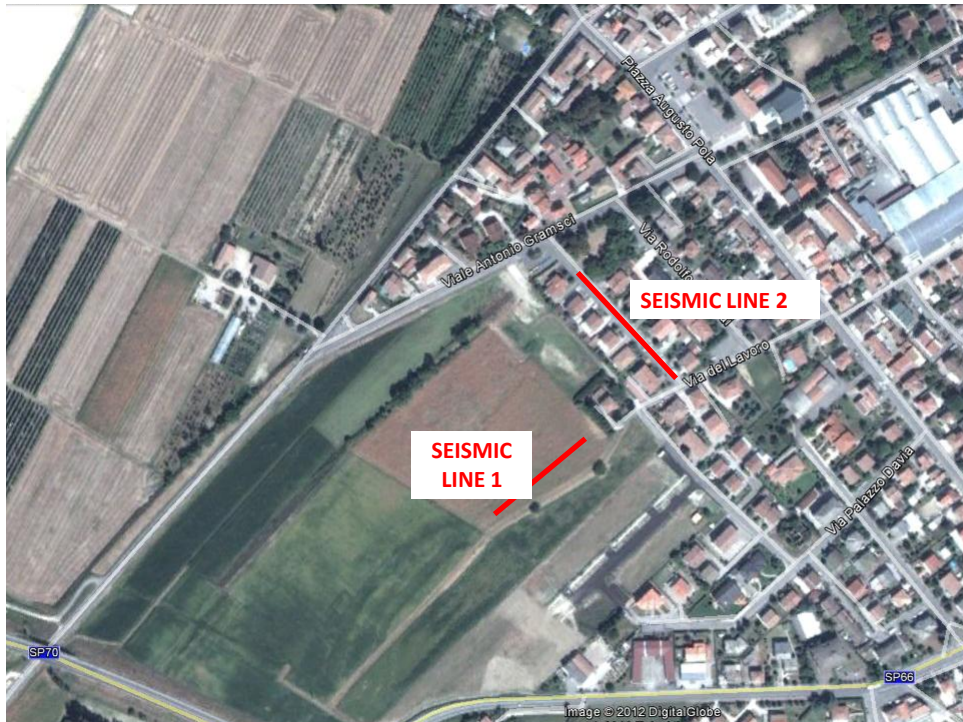


Figure 64 Locations of seismic lines 1 and 2 along the western edge of San Carlo.

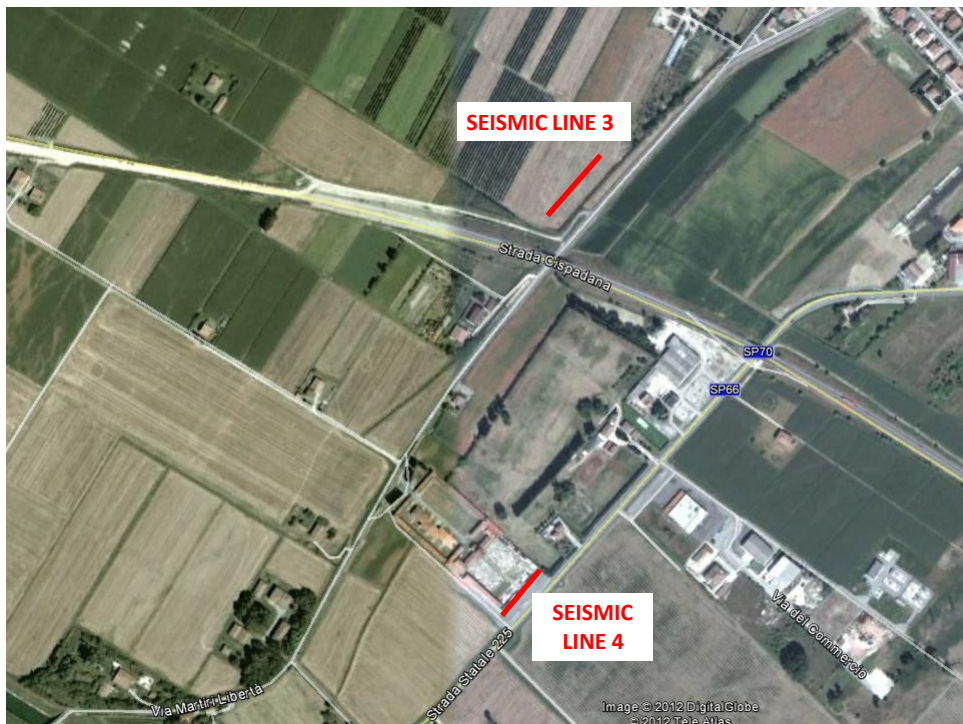


Figure 65 Locations of seismic lines 3 and 4 along the western edge of San Carlo.

## 3.2. Seismic data acquisition

Two different geophysical testing systems were employed in the field:

1. for MASW and ReMi testing:

- Summit DMT seismometer 24-channel
- 24 4.5 Hz Clark geophones
- 8 kg hammer and metallic base plate
- micro-explosive energizer with cartridge system

For MASW and ReMi the receiver configuration consisted of a linear receiver array, spaced at regular intervals (2.5m for lines 1 and 4, and 3m for lines 2 and 3). In MASW testing, which requires a transient source we used the hammer and micro-explosive energizer. The acquisition time for MASW was 8sec at sampling rate 1/8 msec, whereas for ReMi the acquisition time was approximately 30min at sampling rate 1msec. We used identical geometrical acquisition for MASW and ReMi to speed up field acquisition, and in order to compare the Vs results between the two methods.

2. for Nakamura H/V testing:

- -5s Lennartz 3-component velocity meter
- -digitizer

For Nakamura H/V, we recorded noise for over 30min at a rate of 250Hz.

## 3.3. Data Analysis and Results

### MASW

The standard procedure for interpreting MASW data, is to start by inspection of the shot gathers in time- and frequency-offset space in order to reject noisy channels. Once the final shot gather is assumed, the time-space (t-x) data is transformed into frequency-wavenumber (f-k) space, which can be viewed as a phase velocity vs. frequency plot. The next step is to pick the dispersion curve, defined as the Rayleigh wave velocity as a function of frequency.

From the experimental data collected in May 29<sup>th</sup> 2012, we analyzed both hammer and micro-explosive shot records and selected the records with higher signal/noise ratio and clearer f-k appearance. Figure 66 shows the phase velocity vs. frequency plots from the four testing lines (at sites 1-4), and Figure 67 shows the picked fundamental mode dispersion curves. It should be noted that lines 3 and 4 contained strong presence of higher modes, which may be due to an inversely dispersive profile. A comparison of the 4 dispersion curves (Figure 67) suggests that although all lines are characterized by relatively low velocity near-surface, the four sites have distinct Vs profiles.

We proceeded with inversion of the fundamental mode dispersion curves using the Neighborhood Algorithm inversion technique, for a generic 3-layer plus half-space model. The experimental and model dispersion curves, along with the inverted seismic profiles are shown in Figure 68. All processing for the MASW data was performed using the open source geopsy software platform ([www.geopsy.org](http://www.geopsy.org)).

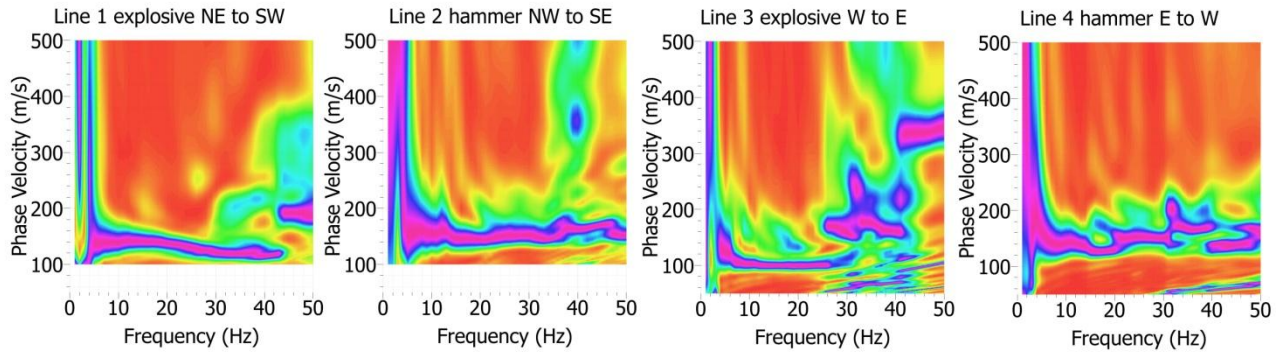


Figure 66 Phase velocity vs. frequency plots for the four seismic testing lines performed at San Carlo village.

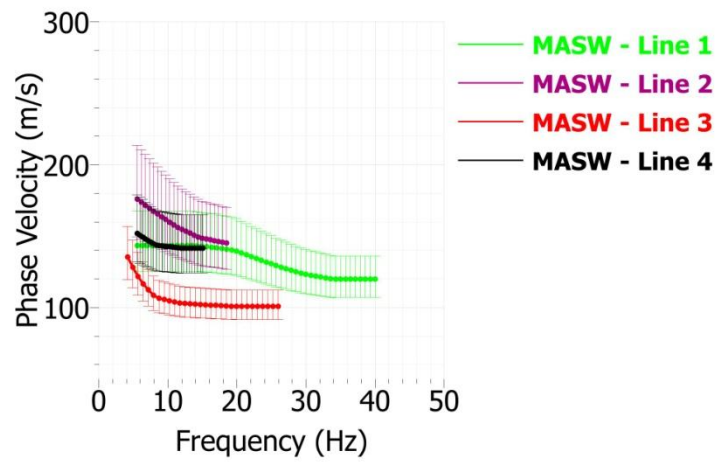


Figure 67 Picked fundamental mode dispersion curves for the four seismic testing lines.

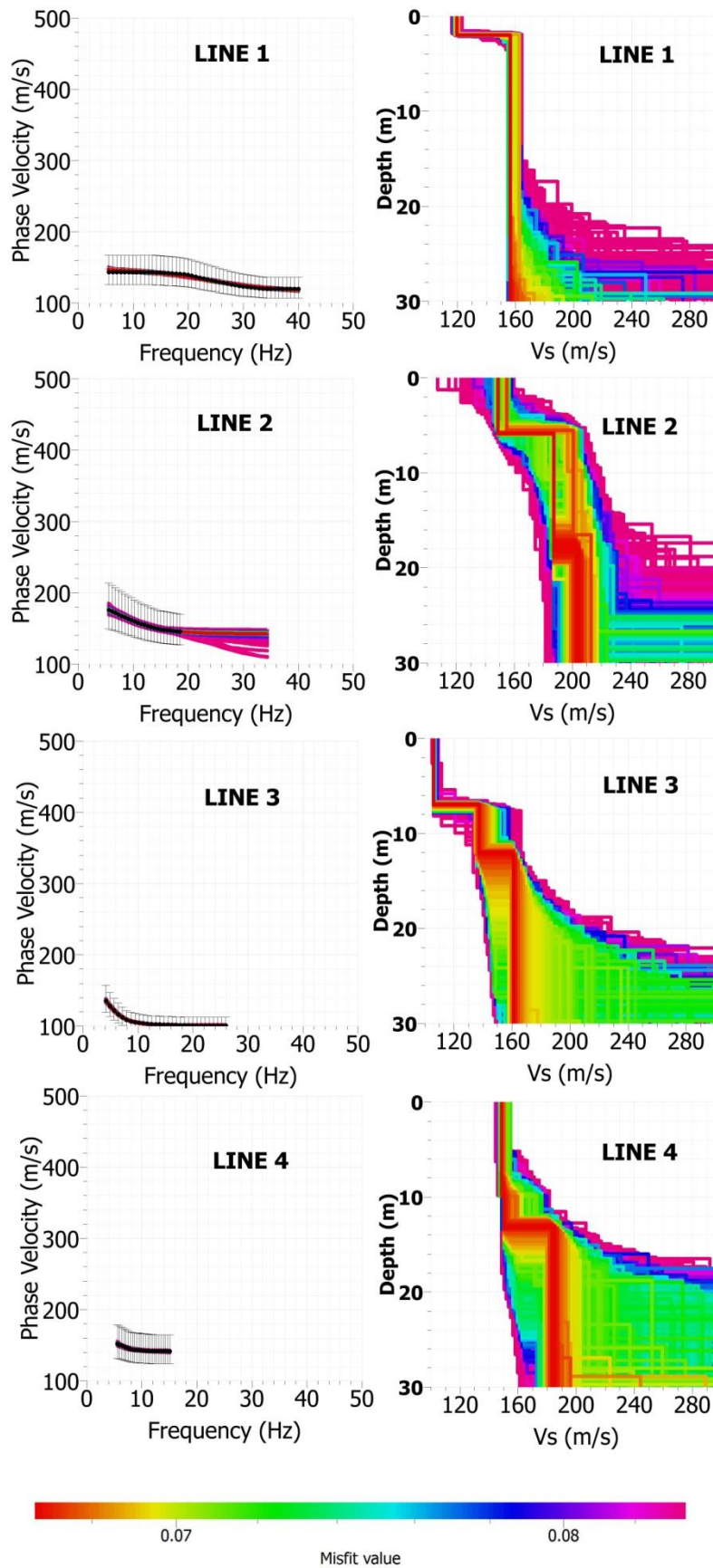


Figure 68 Modeled vs. experimental dispersion curves (left) and modeled Vs profile (right) for the four seismic lines for MASW data.

## ReMi

Similar to MASW, processing for the ReMi data required a preliminary quality check of the data looking at the time-offset ( $t-x$ ) and frequency offset ( $f-x$ ) of the shot gathers in order to identify the noisy traces. The  $f-k$  spectrum was computed for the entire data record ( $\sim 30$ min) using no anti-triggering of sample tolerance and thresholds,  $f-k$  gridding of 0.035 rad/m and grid size of 0.5 rad/m. Figure 69 shows the phase-velocity vs. frequency plots for lines 1-4 (at sites 1-4, respectively).

With manual picking, the phase velocity of the fundamental mode was selected to construct the dispersion curve. The data processing including  $f-k$  spectra computation and picking of the dispersion curve was completed with the open source software package *geopsy* ([www.geopsy.org](http://www.geopsy.org)).

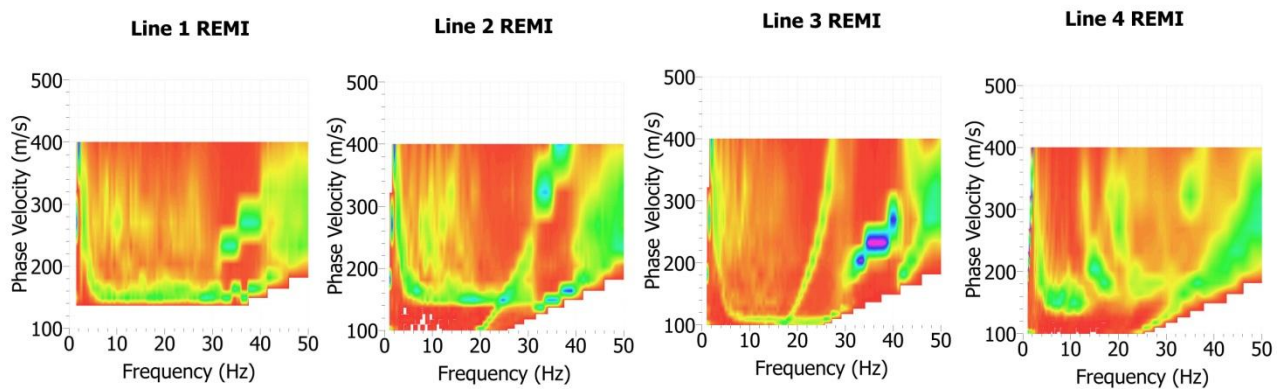


Figure 69 Phase velocity vs. frequency for ReMi data from lines 1-4.

Figure 70 through Figure 73 show a comparison of the picked ReMi vs. MASW dispersion curves for lines 1-4, respectively. The main conclusion from this comparison of the two datasets is that the ReMi and MASW techniques yield similar Rayleigh-wave phase velocity results, with the ReMi data tending to occupy a lower frequency band as is expected due to two main reasons: i) the lower frequency content of their source energy, and ii) the fact that the entire experimental line is used in the analysis, given that there are no near-field concerns, which leads to a longer effective experimental line, and hence lower usable frequency in the dispersion curve. Figure 70 through Figure 73 also show the 'hybrid' dispersion curve constructed from an average of the two types of data, which is thereafter inverted.

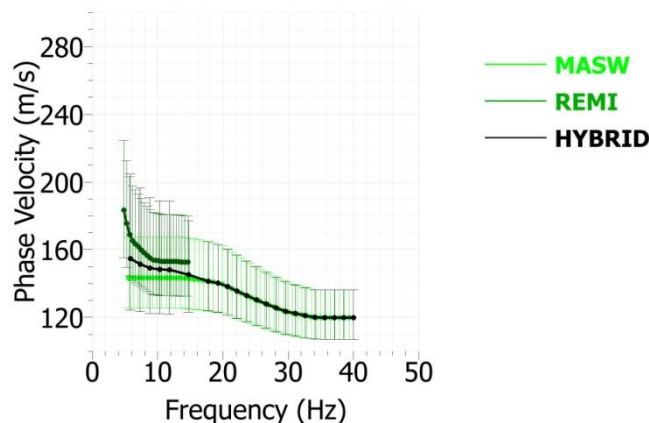


Figure 70 Dispersion curves for MASW, ReMi, and the 'hybrid' dispersion curves for line 1.

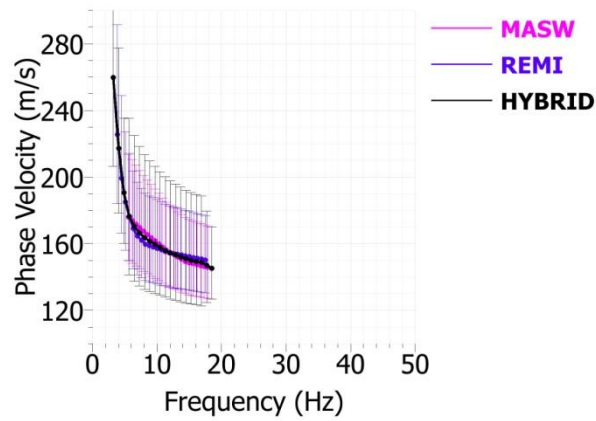


Figure 71 Dispersion curves for MASW, ReMi, and the 'hybrid' dispersion curves for line 2.

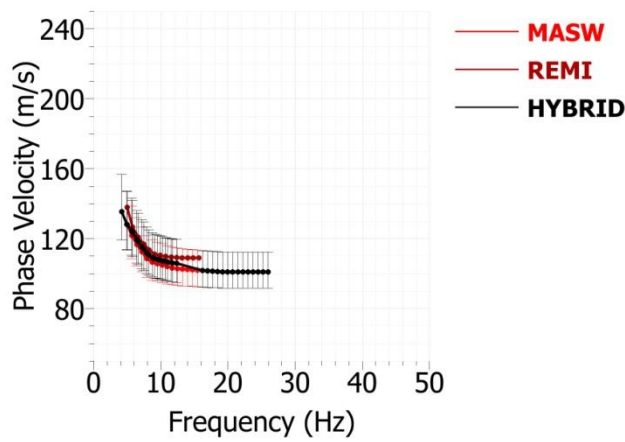


Figure 72 Dispersion curves for MASW, ReMi, and the 'hybrid' dispersion curves for line 3.

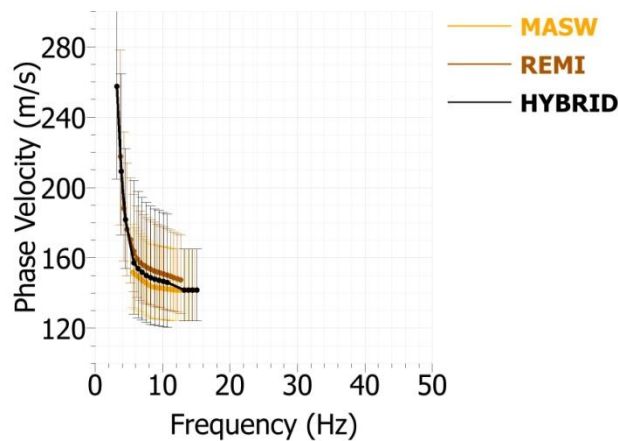


Figure 73 Dispersion curves for MASW, ReMi, and the 'hybrid' dispersion curves for line 4.

The inversion of the 'hybrid' dispersion curves is shown in Figure 74 for a model using 2 layers plus half-space and Figure 75 for 3 layers plus half-space. Comparing the two types of models, we concluded that the 2 layer plus half-space modeling is adequate to capture the main velocity transition with similar  $V_s$  values and at similar depths. The inverted  $V_s$  profiles shown tend to have a very low near-surface velocity, especially for lines 1 and 3 which correspond to the profiles executed inside the fields, whereas lines 2 and 4, which correspond to the profiles executed on asphalt pavement, the near-surface velocity is higher.

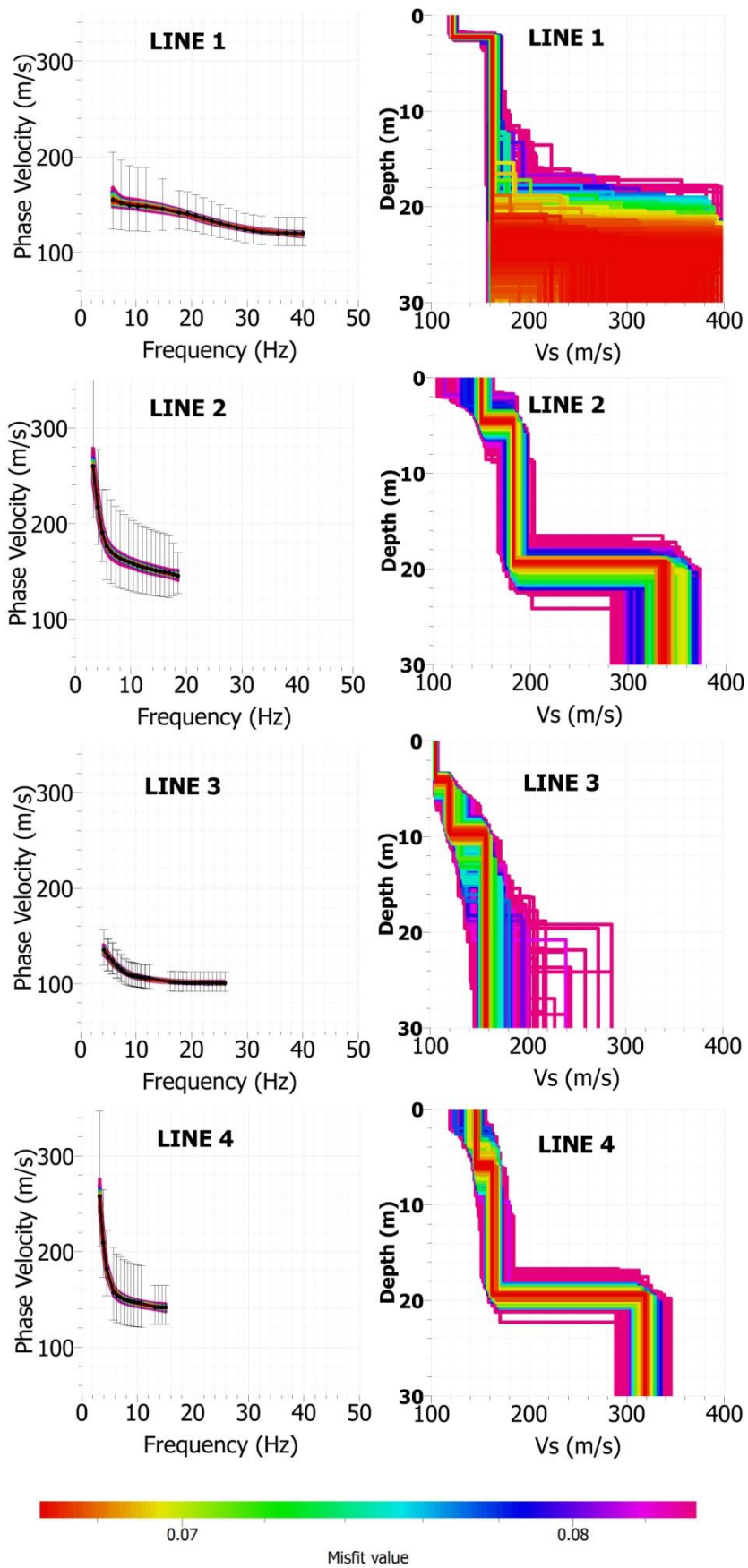


Figure 74 Modeled vs. experimental dispersion curves (left) and modeled Vs profile (right) for the four seismic lines for MASW-ReMi data using a 2 layers plus half-space model.

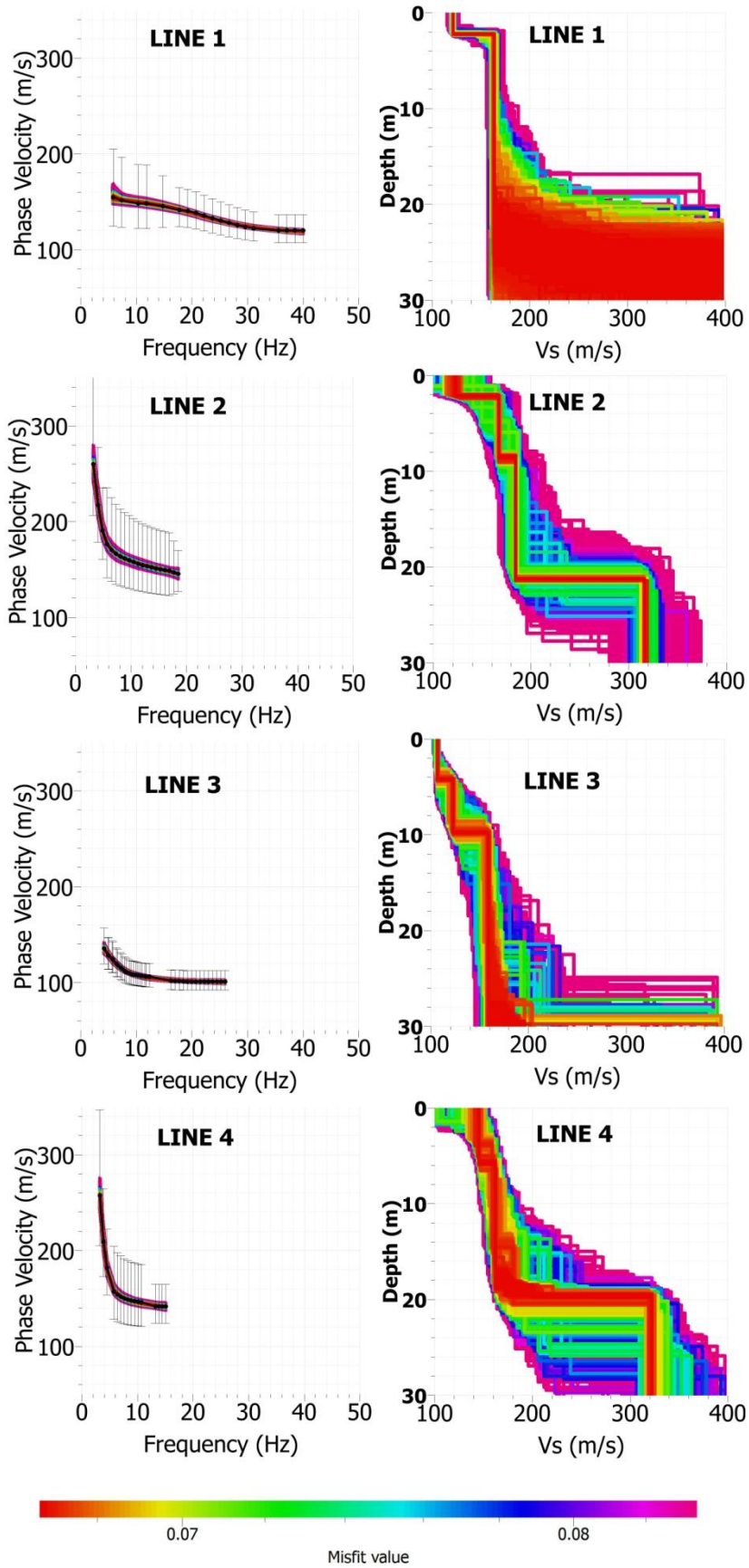


Figure 75 Modeled vs. experimental dispersion curves (left) and modeled Vs profile (right) for the four seismic lines for MASW-ReMi data using a 3 layers plus half-space model.

As a consequence of the higher near-surface velocity, and similar low-frequency dispersion curve information, the inversion for these two profiles (2 and 4) extends deeper. To compute the  $V_{s,30}$  value we employ the formula:

$$V_{s,30} = \sum_{i=1,N} \frac{30}{\frac{d_i}{V_{s_i}}}$$

The corresponding  $V_{s,30}$  values for the 4 sites are shown in Table 5, whereas the recommended  $V_s$ -profiles for each site is shown in Table 6 through Table 9.

**Table 5** Computed  $V_{s,30}$  values at the 4 investigated sites.

Seismic Line	1	2	3	4
$V_{s,30}$ (m/s)	181	208	143	172

**Table 6**  $V_s$  profile resulting for array 1.

Layer No.	Depth (m)	Mean $V_s$ (m/s)	Min. $V_s$ (m/s)	Max. $V_s$ (m/s)
1	0-2	122	120	140
2	2-22	164	155	175
3	22-30	397	300	420

**Table 7**  $V_s$  profile resulting for array 2.

Layer No.	Depth (m)	Mean $V_s$ (m/s)	Min. $V_s$ (m/s)	Max. $V_s$ (m/s)
1	0-5	150	135	170
2	5-15	185	165	200
3	15-40	348	300	420

**Table 8**  $V_s$  profile resulting for array 3.

Layer No.	Depth (m)	Mean $V_s$ (m/s)	Min. $V_s$ (m/s)	Max. $V_s$ (m/s)
1	0-4	110	105	140
2	4-6	125	120	145
3	6-30	160	150	180

**Table 9**  $V_s$  profile resulting for array 4.

Layer No.	Depth (m)	Mean $V_s$ (m/s)	Min. $V_s$ (m/s)	Max. $V_s$ (m/s)
1	0-6	145	125	165
2	6-13	162	155	190
3	13-40	320	300	420

Figure 76 shows a summary of the recommended Vs profiles for the four sites, along with the results by Cocco et al. (2001). The latter study used a variety of measurements, including surface and down-hole (cross-hole and up-hole) Vs measurements and a boring to derive an average profile located approximately 8km North of our testing sites. Their results, although different from our profiles, capture a similar trend: a low Vs at the surface (<250 m/s) and a Vs increase at approximately 15m, which is however deeper from the inversion of our measurements (20-25 m). From their borehole measurements, Cocco et al. (2001) also identified a continental/marine sediment transition at 103m, which corresponds to a jump in Vs to 490 m/s, followed by the transition into bedrock at 130m, corresponding to Vs to 2000 m/s. Their stratigraphic log and Vs model are included in the Appendix (Figures A-1 and A-2). Table 10 summarizes the Vs model after Cocco et al. (2001).

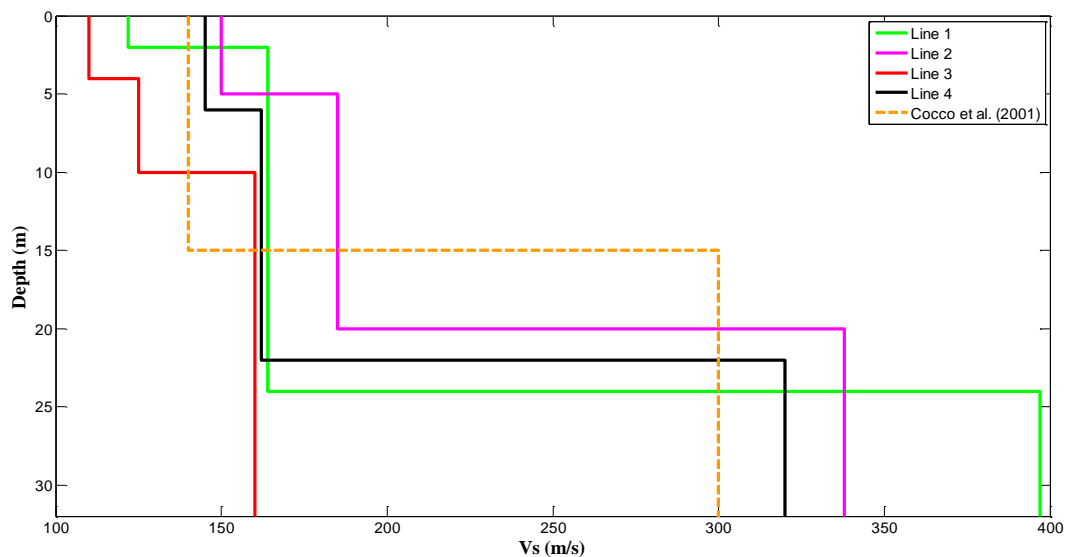


Figure 76 Summary of the recommended Vs profiles for the four sites, along with the results by Cocco et al. (2001).

Table 10 Vs model after Cocco et al. (2001).

Depth (m)	Vs (m/s)
0-15	140
15-103	300
103-130	490
Half-space	2000

### Nakamura H/V

The H/V technique, which is best known as the Nakamura method uses the ratio of the horizontal over the vertical component of ambient noise. The H/V ratio for a body wavefield should always exhibit a peak around the fundamental S-wave frequency, for high impedance contrast sites. It has been observed that the H/V *ellipticity ratio* of the Rayleigh wave exhibits a maximum at a frequency  $f_R$  that is very close to the fundamental resonance frequency for S-waves for S-wave velocity contrast exceeding a value of 4. Hence the H/V ratio of ambient noise, being often related to the ellipticity of surface waves, can be used to identify the peak in order to detect the natural frequency of the site.

We recorded approximately 45min of ambient noise at locations 1-4, and computed the spectra for each component, north, east and vertical, shown in Figure 77. The corresponding H/V ratios are shown in Figure 78. The corresponding peak frequencies of the H/V ratios were 1.07, 0.99, 1.07, and 0.92Hz. Based on the spectra of Figure 77, these frequencies are not present in all three components, which implies that these frequencies are not industrial noise (also given that they are so low makes it highly improbable that they are the result of human activity) and are most likely due to the subsurface structure. It is important to note that these peak frequencies do not satisfy the ‘clarity criteria’, which involve both amplitude and stability criteria, as described in the SESAME European research project. This lack of ‘clarity’ in the experimental peaks suggests that one or more of the assumptions implicit in the theory behind H/V, such as the existence of a very large S-wave velocity contrast, or the assumption for the site as 1D. Hence, we should interpret these peaks with certain caution.

Using the standard formula to compute the fundamental period for 1D site response (Kramer, 1996):

$$T_s = \frac{4H}{V_s}$$

which links the site period ( $T_s$ ) to the average shear-wave velocity ( $V_s$ ) and the depth to bedrock ( $H$ ), we can compute, for  $V_s$  equal to 400 m/s the following approximate depths to ‘bedrock’: 93, 101, 93 and 109 m for locations 1-4, corresponding to an average of 99m.

In comparison to these measurements, Cocco et al. (2001) present H/V ratios from earthquake and noise data, and conclude that for the noise data, their fundamental peak is in the order of 0.8 Hz with an amplitude of 8, whereas for earthquake data there is no clear peak (Figure 79). They conclude that the low frequency peak corresponds to the sediment/bedrock transition at 125m depth.

At this stage, our H/V values cannot be interpreted independently given that the experimental peaks did not satisfy the ‘clarity’ criteria, however, they suggest the presence of a  $V_s$  discontinuity at approximately 100m depth, which may be either a sediment/sediment or sediment/bedrock transition. Based on the velocity profile of Cocco et al. (2001), at 103m depth at their location there is a jump in  $V_s$ , namely from 300m/s to 490m/s, which however does not result in a distinct H/V peak. Hence, it is more likely that the peak in our experimental data is in fact due to the sediment/bedrock transition, which may locally occur at approximately 100m depth. As seen from seismic reflection sections shown in the Appendix (Figure A-3 and A-4) (Boccaletti et al., 2004), undulations in the bedrock are present, which may explain a difference in bedrock depth between our testing location and that of Cocco et al. (2001).

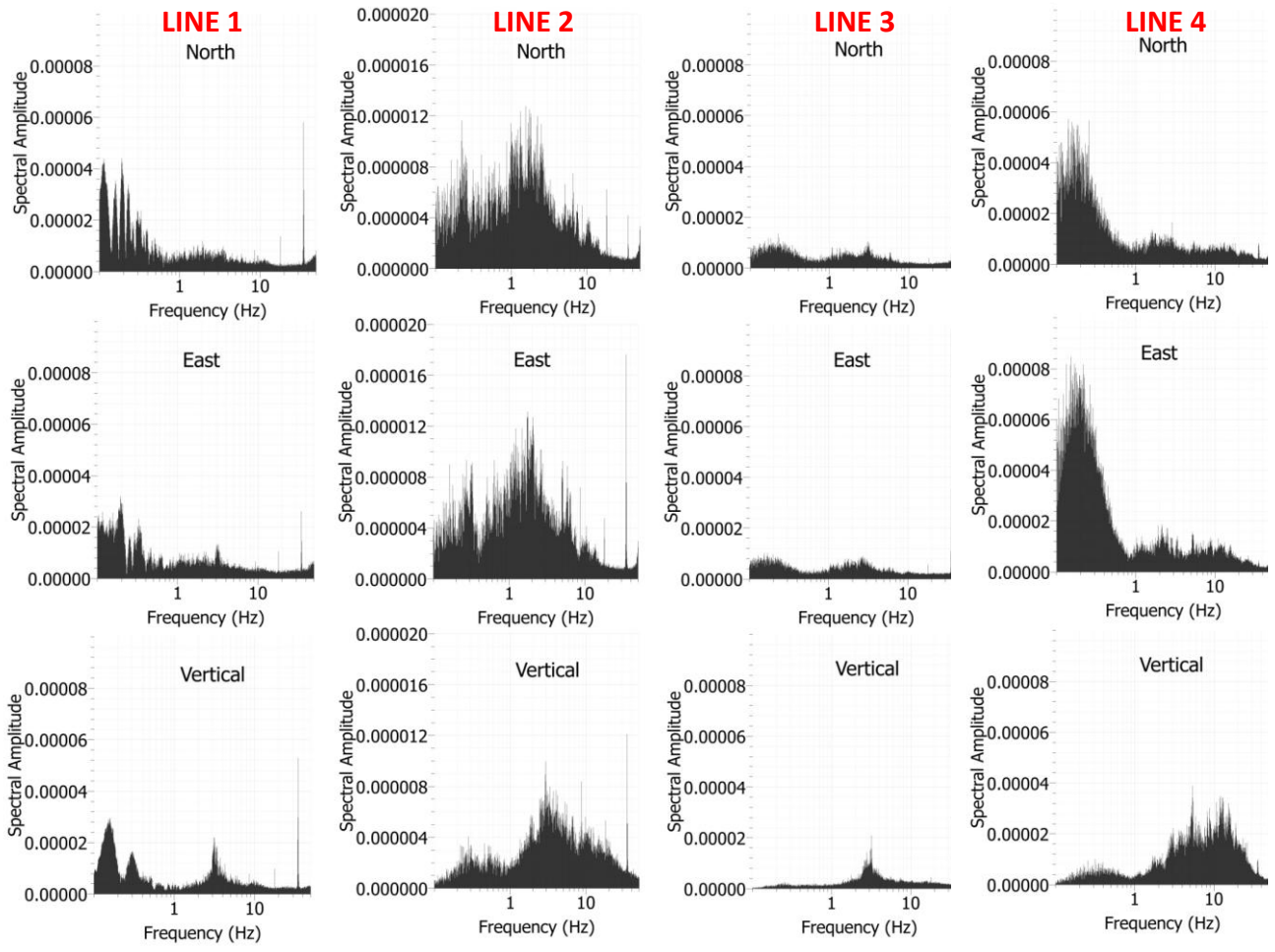


Figure 77 Recorded 3-component spectra at the four site locations.

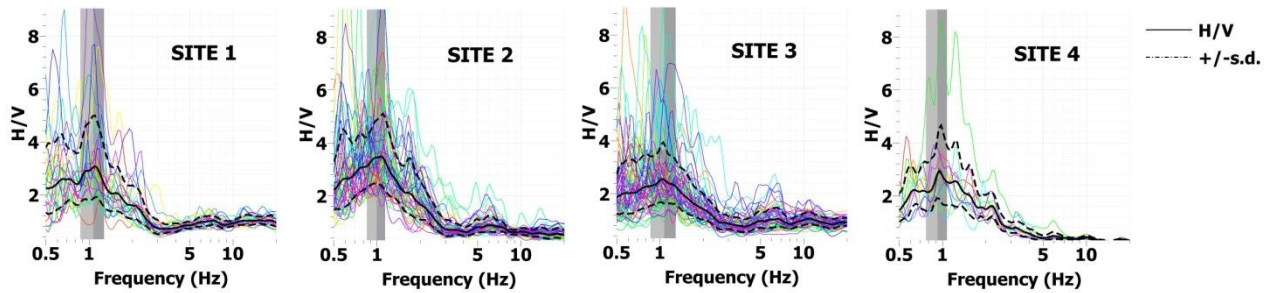
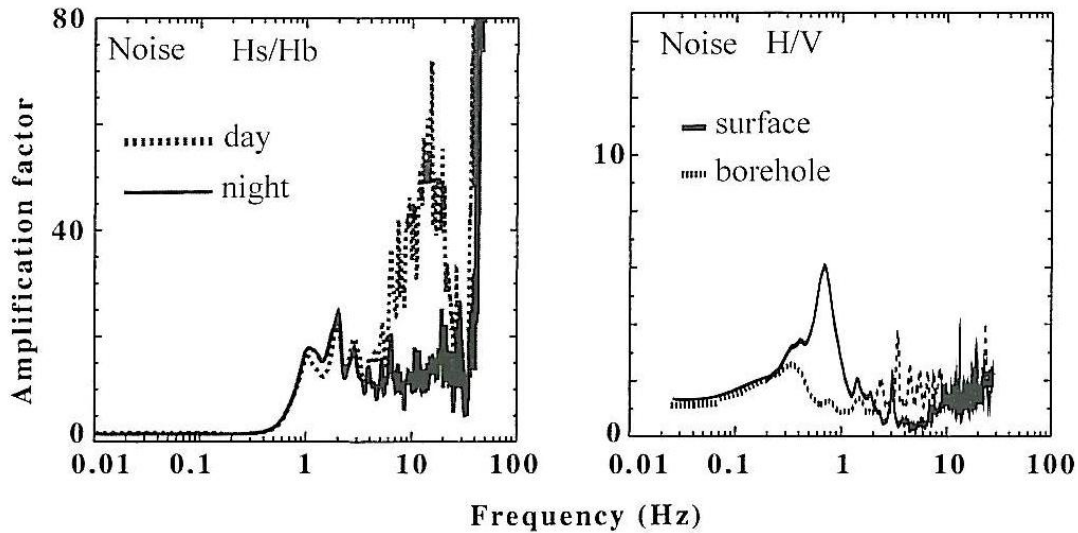


Figure 78 Processed H/V spectral ratios for the four site locations showing average and +/- s.d. H/V curves.



**Figure 79** Spectral ratios of ground noise: the left panel shows the spectral ratio between the horizontal components recorded at the surface and borehole sensors. The right panel shows the H/V measurements (similar to our type of measurements) resulting from surface and borehole recordings (adapted from Cocco et al., 2001).

### 3.4. Remarks

The geophysical campaign executed in May 29<sup>th</sup> 2012 was successful at determining the shear-wave velocity profile at four sites, which showed extensive evidence of fracturing, liquefaction as well as structural damage, in order to assist with the analysis of co-seismic effects. The data acquisition and processing was efficient and fast for MASW and ReMi and provided consistent results for the top 30m, and in some locations even deeper (40m). These results show very low shear-wave velocities in the upper subsurface. For future campaigns, it may also be important to acquire longer lines in order to assess the shear-wave velocity profile at deeper depths.

On the other hand, the H/V data acquired from the current campaign showed evidence of H/V peaks, which did not satisfy the ‘clarity’ criteria, and hence their interpretation is not straightforward. This may be for example due to the sites not being 1D, or the sediment/bedrock discontinuity not involving a large  $V_s$  contrast. It may be worthwhile in future campaigns in this area to acquire longer ambient noise records, which will improve the statistical averaging in the H/V processing.

Given that we cannot model the  $V_s$  profile deeper than 30m with our current data, we suggest extrapolating the results of Cocco et al. (2001) for depths deeper than 30m (for lines 1 and 3) and 40m (for lines 2 and 4).

## References

- Atzori, S., Merryman Boncori, J., Pezzo, G., Tolomei, C., Salvi, S. (2012). Secondo Report analisi dati SAR e modellazione della sorgente del terremoto dell'Emilia. INGV.
- Barbieri, M. (2003). Brevi note storico-geografiche sul Reno, in "Reno, campi e uomini", *Rivista periodica della pianura*, Anno I, n. 1, giugno-dicembre 2003,
- Bindi, D., Pacor, F., Luzi, L., Puglia, R., Massa, M., Ameri, G., Paolucci, R. (2011). Ground Motion Prediction Equations Derived from the Italian Strong Motion Data Base. *Bulletin of Earthquake Engineering*, vol: 9, n. 6, 1899-1920.
- Boccaletti, M., Bonini, M., Corti, G., Gasperini, P., Matrelli, L., Piccardi, L., Severi, P., Vannucci, G. (2004). Carta Sismotettonica della regione Emilia-Romagna, Note Illustrative. Servizio Geologico Sismico e dei Suoli.
- Carminati, E., Enzi, S., Camuffo, D. (2007). A study on the effects of seismicity on subsidence in foreland basins: An application to the Venice area. *Global and Planetary Change*, vol: 55 (2007) 237-250.
- Cauzzi, C., Faccioli, E. (2008). Broadband (0.05 a 20 s) prediction of displacement response spectra based on worldwide digital records. *Journal of Seismology*, 3, DOI 10.1007/s10950-008-9098-y.
- Cetin, K.O., Bilge, H.T., Wu, J., Kammerer, A., Seed, R.B. (2009). Probabilistic models for the assessment of cyclically-induced reconsolidation (volumetric) settlements. *Journal of Geotechnical and Geoenvironmental Engineering*, vol: 135 (3), 387-398.
- Cocco, M., Ardizzoni, F., Azzara, R.M., Dall'Ilio, L., Delladio, A., Di Bona, M., Malagnini, L., Margheriti, L., Nardi, A. (2001). Broadband waveforms and site effects at a borehole seismometer in the Po alluvial basin (Italy). *Annali di Geofisica*, 44, 1, 137-154.
- Comité Européen de Normalisation, CEN (2004). Eurocode 8 - Design of Structures for earthquake resistance - Part 1: General rules, seismic actions and rules for buildings. EN 1998-1, CEN, Brussels.
- Deshpande, A., Flemings, P.B., Huang, J. (1997). Quantifying lateral heterogeneities in fluvio-deltaic sediments using three-dimensional reflection seismic data: Offshore Gulf of Mexico. *Journal of Geophysical Research*, 102, 385-401.
- Devoti, R., Riguzzi, F., Cuffaro, M., Doglioni, C. (2008). New GPS constraints on the kinematics of the Apennines subduction. *Earth and Planetary Science Letters*, 273, 163-174.
- DISS Working group (2007). Database of individual seismogenic sources (version 3.0.4). A compilation of potential sources for earthquakes larger than M 5.5 in Italy and surrounding areas, available at <http://www.ingv.it/DISS>.
- Foti, S. (2000). Multi-Station Methods for Geotechnical Characterisation Using Surface Waves. PhD Diss., Politecnico di Torino.
- Guidelines for the implementation of the H/V spectral ratio technique on ambient vibrations: measurements, processing and interpretation (2005). Project No. EVG1-CT-2000-00026 SESAME, source: [http://sesame-fp5.obs.ujfgrenoble.fr/SES\\_TechnicalDoc.htm](http://sesame-fp5.obs.ujfgrenoble.fr/SES_TechnicalDoc.htm), 62 pages.
- Galli, P. (2000). New empirical relationships between magnitude and distance for liquefaction. *Tectonophysics*, 324 (2000) 169-187.

- Idriss, I.M., Boulanger, R.W. (2008). Soil Liquefaction During Earthquakes. EERI Monograph.
- Ishihara, K., Yoshimine, M. (1992). Evaluation of settlements in sand deposits following liquefaction during earthquakes. *Soils and Foundations*, vol: 32(1), 1 3-188.
- Iwasaki, T., Tatsuoka, F., Tokida K., Yasuda, S. (1978). A practical method for assessing soil liquefaction potential based on case studies at various sites in Japan. 2nd International Conference on Microzonation for Safer Construction - Research and Application, San Francisco, Calif., 26 November - 1 December. American Society of Civil Engineers, New York. Vol. 2, 885-896.
- Kramer, S.L. (1996). Geotechnical Earthquake Engineering, Prentice Hall.
- Louie, J. N. (2001). Faster, better: shear-wave velocity to 100 meters depth from refraction microtremor arrays. *Bulletin of the Seismological Society of America*, vol: 91, 347-364.
- Mantovani, E., Viti, M., Babbucci, D., Cenni, N., Tamburelli, C., Vannucchi, A., Falciani, F., Fianchisti, G., Baglione, M., D'Intinosante, V., Fabbroni, P. (2011). Sismotettonica dell'Appennino settentrionale Implicazioni per la pericolosità sismica della Toscana. Regione Toscana
- Martelli, L. (2012). Liquefaction effects observed in occasion of the 2012 May 20 earthquake in the Emilia plain. 7<sup>th</sup> European Congress on Regional Geoscientific Cartography and Information Systems (EUREGEO). Bologna, Italy June 12-15, 2012.
- NTC (2008). Norme tecniche per le Costruzioni, D.M. 14.1.2008 (Italian Building Code, in Italian).
- Rota, M., Lai, C.G., Strobbia, C.L. (2011). Stochastic 1D site response analysis at a site in central Italy. *Soil Dynamics and Earthquake Engineering*, vol: 31 (2011), 626-639.
- Rota, M., Zuccolo, E., Taverna, L., Corigliano, M., Lai, C.G., Penna, A. (2012). Mesozonation of the Italian territory for the definition of real spectrum-compatible accelerograms. Accepted for publication to the *Bulletin of Earthquake Engineering*. May 2012.
- Seed, R.B. (2010). Technical review and comments: 2008 EERI Monograph Soil Liquefaction During Earthquakes by I.M. Idriss and R.W. Boulanger. Geotechnical Report N° UCB/GT - 2010/2011 University of California at Berkeley.
- Toscani, G., Burrato, P., Di Bucci, D., Seno, S., Valensise, G. (2009). Plio-Quaternary tectonic evolution of the Northern Apennines thrust fronts (Bologna-Ferrara section, Italy): Seismotectonic implications. *Bollettino della Società Geologica Italiana* 128 (2), 605-613.
- Yilmaz, Z. (2004). GIS-Based Structural Performance Assessment of Sakarya City after 1999 Kocaeli-Turkey Earthquake from Geotechnical and Earthquake engineering Point of View, M.Sc. Thesis, The Graduate School of Natural and Applied Sciences, Middle East Technical University (METU), Ankara, Turkey.
- Yoshimine, M., Nishizaki, H., Amano, K., Hosono, Y. (2006). Flow deformation of liquefied sand under constant shear load and its application to analysis of flow slide of infinite slope. *Soil Dynamics and Earthquake Engineering*, vol: 26(2-4), 253-264.
- Youd, T.L., Idriss, I.M., Andrus, R.D., Arango, I., Castro, C., Christian, J.T., Dobry, R., Finn, W.D.L., Harder, L.F., Hynes, M.E., Ishihara, K., Koester, J.P., Liao, S.C.C., Marcuson, W.F., Martin, G.R., Mitchell, J.K., Moriwaku, Y., Power, M.S., Robertson, P.K., Seed, R.B., Stokoe, K.H. (2001). Liquefaction Resistance of Soils. Summary Report from the 1996 NCEER and 1998 NCEER/NSF. *Journal of Geotechnical and Geoenvironmental Engineering*, ASCE, vol: 127 (10), 817-833.

# Appendix

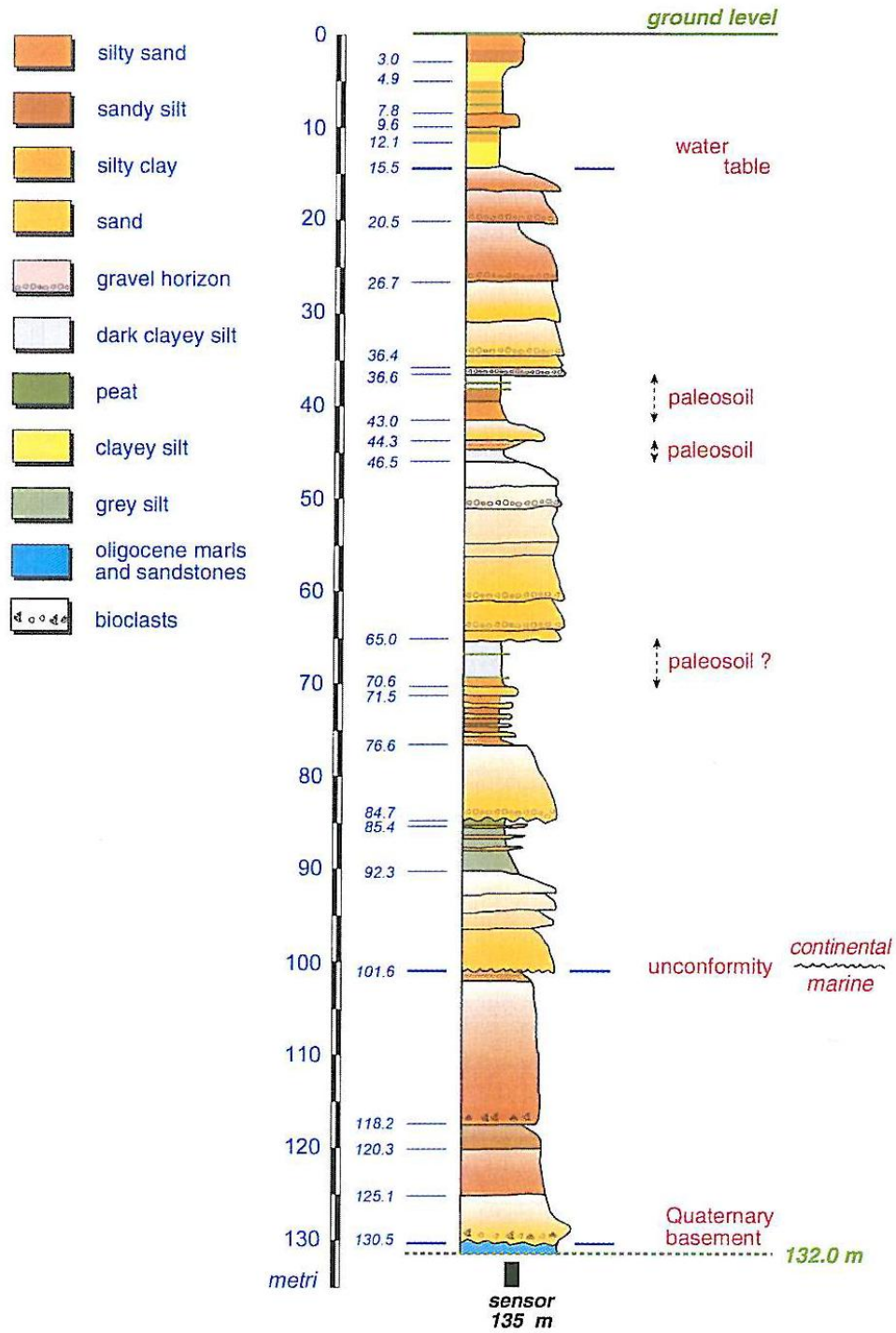


Figure A-1 Stratigraphic log (Cocco et al., 2001).

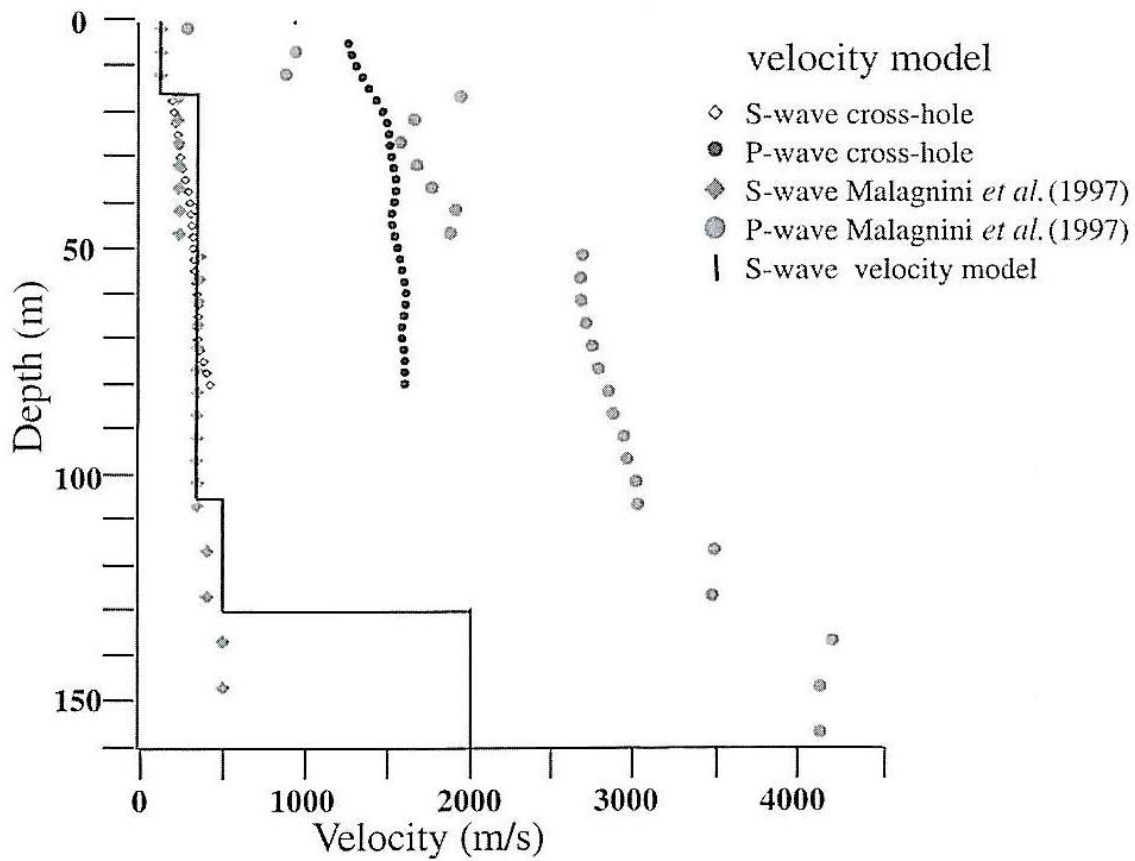


Figure A-2 P- and S-wave models (Cocco et al., 2001).

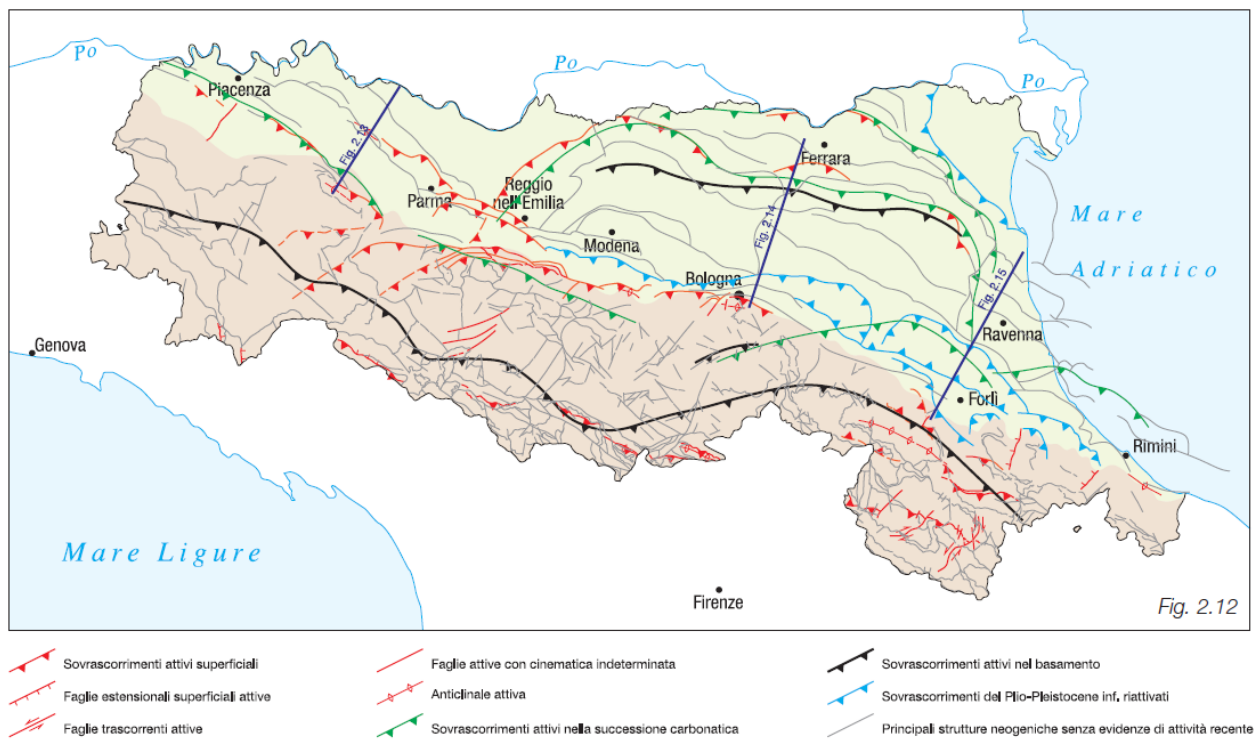


Figure A-3 Geologic map of Emilia-Romagna (Bocaletti et al., 2004).

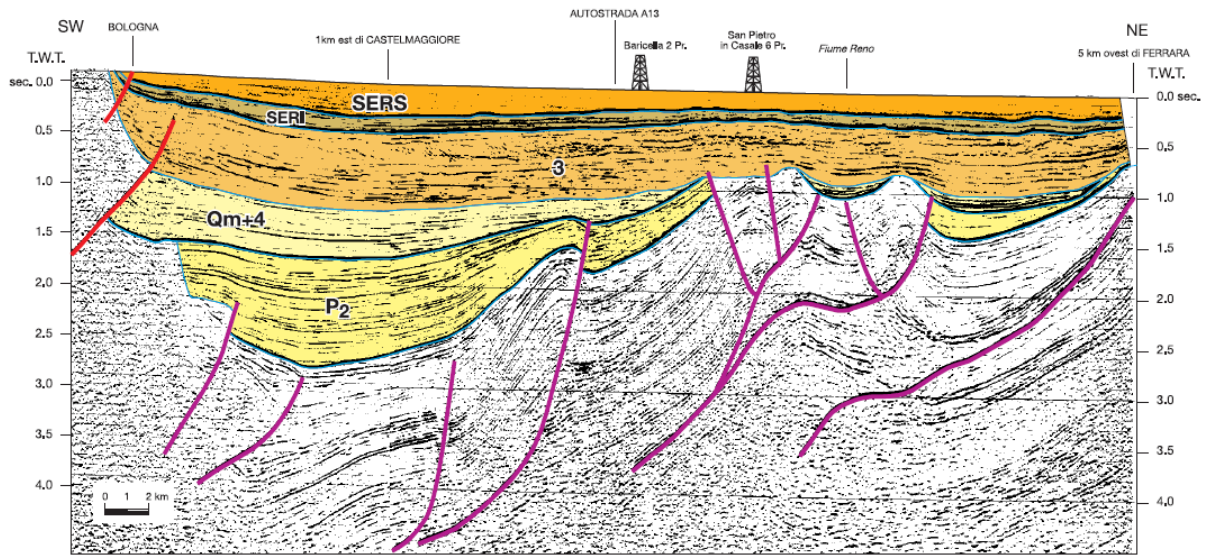


Fig. 2.14

Figure A-4 Seismic reflection cross-section along section marked in Figure A-3 (Bocaletti et al., 2004).